

Power Combiner and Antenna Array Concepts for Millimeter Wave Applications

van Schelven, R.M.

DOI

[10.4233/uuid:26400589-ae0f-46bc-aaea-70004d5fbbf2](https://doi.org/10.4233/uuid:26400589-ae0f-46bc-aaea-70004d5fbbf2)

Publication date

2022

Document Version

Final published version

Citation (APA)

van Schelven, R. M. (2022). *Power Combiner and Antenna Array Concepts for Millimeter Wave Applications*. [Dissertation (TU Delft), Delft University of Technology].
<https://doi.org/10.4233/uuid:26400589-ae0f-46bc-aaea-70004d5fbbf2>

Important note

To cite this publication, please use the final published version (if applicable).
Please check the document version above.

Copyright

Other than for strictly personal use, it is not permitted to download, forward or distribute the text or part of it, without the consent of the author(s) and/or copyright holder(s), unless the work is under an open content license such as Creative Commons.

Takedown policy

Please contact us and provide details if you believe this document breaches copyrights.
We will remove access to the work immediately and investigate your claim.

Power Combiner and Antenna Array Concepts for Millimeter Wave Applications

Power Combiner and Antenna Array Concepts for Millimeter Wave Applications

Dissertation

for the purpose of obtaining the degree of doctor
at Delft University of Technology
by the authority of the Rector Magnificus, prof.dr.ir. T.H.J.J. van der Hagen,
chair of the Board for Doctorates
to be defended publicly on
Wednesday 19 January 2022 at 10:00 o'clock

by

Ralph Matthijs VAN SCHELVEN

Master of Science in Electrical Engineering,
Delft University of Technology, the Netherlands,
born in Dordrecht, the Netherlands.

This dissertation has been approved by the promotor.

Composition of the doctoral committee:

Rector Magnificus,	chairperson
Prof.dr.ing. A. Neto	Delft University of Technology, promotor
Dr. D. Cavallo	Delft University of Technology, copromotor

Independent members:

Prof.dr. A. Yarovoy	Delft University of Technology
Prof.dr. R. Sauleau	Université de Rennes 1, France
Prof.dr.ir. A.B. Smolders	Eindhoven University of Technology
Prof.Dr.-Ing. M. Geissler	IMST GmbH, Germany
Prof.dr. L.C.N. de Vreede	Delft University of Technology, reserve member

Other members:

Dr. G. Carluccio	NXP Semiconductors Eindhoven
------------------	------------------------------

The work presented in this thesis has been performed at TU Delft and financed by the Dutch Technology Foundation NWO-TTW (WAtt LEvel transmitters at mmwaves (WhALE), 15591), as part of the TTW-NXP partnership programme “Advanced 5G Solutions”.



Keywords: Artificial dielectric layers, equivalent circuit, leaky wave, pattern shaping, phased array, power combiner, slot antenna

Printed by: Ipskamp Printing

Cover design: Ralph van Schelven

Copyright © 2021 by R.M. van Schelven

ISBN 978-94-6421-612-7

An electronic version of this dissertation is available at
<http://repository.tudelft.nl/>.

Voor mijn ouders

Contents

1	Introduction	1
1.1	Efficient Power Combination for Millimeter Waves	1
1.2	Pattern Shaping for Scan Loss Reduction at Millimeter Wave Frequencies	2
1.3	Antenna Concept	3
1.3.1	Artificial Dielectric Layers for Integrated Transmitters	3
1.3.2	Artificial Dielectric Layers for Pattern Shaping	4
1.4	Antenna Modeling	5
1.4.1	Modelling of the Slot Antenna	5
1.4.2	Modeling of Artificial Dielectric Layers.	5
1.5	Scientific Contribution in this Thesis	5
1.6	Outline of the Thesis	6
2	Equivalent Circuit Models of Finite Slot Antennas	9
2.1	Introduction	9
2.2	MoM Solution for Semi-Infinite Slot	10
2.2.1	Infinite Slot	10
2.2.2	Semi-Infinite Slot	12
2.3	Equivalent Transmission Line Circuit	14
2.3.1	Residue Contribution of the Input Impedance of an Infinite Slot.	14
2.3.2	Residue Contribution of the Mutual Impedance	16
2.3.3	Input Impedance and Accuracy of the Circuit Model.	19
2.3.4	Finite Slot	20
2.4	Analysis of the Slot Termination.	22
2.4.1	Voltage Distribution on the Slot	22
2.4.2	Power Balance	24
2.5	Multiple Feeding Points.	26
2.6	Conclusions.	26
3	Closed-Form Analysis of ADs with Non-Identical or Non-Square Layers	29
3.1	Introduction	29
3.2	z -Aperiodic Artificial Dielectric Layers	30
3.2.1	Problem Definition and Equivalence Principle.	31
3.2.2	Equivalent Impedance of a Layer in a Non-Periodic Sequence	33
3.2.3	Validation of the Closed-Form Solutions	34
3.3	Analysis of Non-square Artificial Dielectric Layers	39
3.3.1	Closed-Form Analysis of a Single Layer	39
3.3.2	Closed-Form Analysis of Multiple Layers.	40
3.4	Conclusion	42

4	Efficient Waveguide Power Combiners at mm-Wave Frequencies	45
4.1	Parallel Plate Waveguide Combiner	45
4.1.1	Single-Feed and Multi-Feed PPW	45
4.1.2	Comparison between SIW and PPW Combiners	46
4.2	PPW Implementation of a Doherty Combiner.	47
4.2.1	Ideal Two-way Series Doherty Circuit	48
4.2.2	PPW Implementation	48
4.2.3	Simulated Results for Impedance and Efficiency.	49
4.3	PCB Demonstrator	50
4.3.1	PCB Design of the Combiner.	51
4.3.2	Measured S-Parameters and De-Embedding of Feed Lines.	53
4.3.3	Impedance and Efficiency Results	54
4.4	Integration with Antenna	55
4.4.1	Design of the PPW Combiner with Antenna	56
4.4.2	Measured S-Parameters	59
4.4.3	Radiation Characteristics	60
4.5	Conclusions.	62
5	Implementing a PPW Combiner with Active Components	65
5.1	Coupling Slot Design	65
5.1.1	Meandered Slot	65
5.1.2	Combiner Design and Matching to PA	66
5.2	Impact of the IC.	68
5.2.1	Undesired Air Gap Mode.	69
5.2.2	Folded Open Stub	70
5.2.3	Co-Optimization of the PA Circuit and Combiner	70
5.3	Output of the Combiner.	71
5.3.1	Coaxial Output.	71
5.3.2	Single Antenna Output.	72
5.3.3	Two-Antenna Array	73
5.4	Conclusions.	73
6	Phased Array with Pattern Shaping and Scan Loss Reduction for Millimeter Waves	77
6.1	Slot with ADL Superstrate in Free Space.	77
6.1.1	Single Slot	77
6.1.2	Array of Slots.	81
6.2	Study on Gain Enhancement and Mutual Coupling.	83
6.3	Array Design	85
6.4	Measurements	87
6.5	Conclusions.	90
7	Conclusions	93
7.1	Equivalent Circuit Models of Finite Slot Antennas.	93
7.2	Closed-Form Analysis of Artificial Dielectrics with Non-Identical or Non-Square Layers	94
7.3	Efficient PPW Power Combiner for mm-Waves	94

7.4	Phased Array with Pattern Shaping and Scan Loss Reduction for mm-Waves	95
7.5	Future Outlook	96
7.6	Impact of the Research	96
A	Derivations of Equivalent Circuit for Non-square ADL	97
A.1	Single Layer	97
A.1.1	Basis Functions	97
A.1.2	Reduced Admittance Matrix	99
A.1.3	Admittance Matrix Entries	100
A.1.4	Equivalent Circuit Representation	105
A.2	Multiple Layers	106
A.2.1	Aligned Layers	106
A.2.2	Misaligned Layers	107
B	Cascading Layers of Non-Square ADL	109
C	Modeling of Power Amplifiers as Sources	113
	Bibliography	117
	Summary	123
	Samenvatting	125
	List of Publications	127
	Propositions Accompanying the Doctoral Thesis	129
	About the Author	131
	Acknowledgements	133

Chapter 1

Introduction

1.1. Efficient Power Combination for Millimeter Waves

The fifth generation of mobile communications (5G) has been conceived to meet the growing wireless traffic demands of the coming decade. Challenging requirements on the 5G networks are set to allow for data volume increase, network scalability and efficient network operation. A key enabler of 5G is the millimeter wave (mm-wave) frequency range, which can provide large spectrum and consequently high-data rates. The work described in this dissertation specifically focuses on the allocated band around 28 GHz.

One of the most challenging aspect of mm-wave communication is related to the efficient generation of radio frequency (RF) power. Currently reported mm-wave power amplifiers (PAs) are unable to reach the required output power to account for the loss margins in commercial applications [1–3]. One typical way to increase the available output power is to combine the signals from multiple PAs using a power combiner. Power combiners in the mm-wave frequency range have been a topic of investigation for many years [4, 5]. Typical solutions are Wilkinson-based combiners [6] as shown in Fig. 1.1(a), but they present area occupation and losses that grow directly with the number of combined elements. More compact combiners have been proposed [7–9], based on parallel or series combination, but their operation is restricted by factors such as impedance variation with number of elements, narrow bandwidth and limited impedance transformation. Waveguide-based power combiners (Fig. 1.1(b)) were presented in [10–13]. An important advantage of this type of structures, with respect to Wilkinson or transformer based combiners, is that the insertion losses do not increase with the number of feeds, thus resulting in efficient power combiners if a large number of PAs is needed to meet the requirements on the output power.

Besides the output power levels, another limitation of mm-wave power amplifiers is the low efficiency [14]. In communication applications, signal modulations are applied to increase the channel capacity. For example, the use of Quadrature Amplitude Modulation requires the transmitter to deliver a range of output power. By decreasing the output power of the PAs, their operating efficiency is reduced. To overcome this problem, a Do-

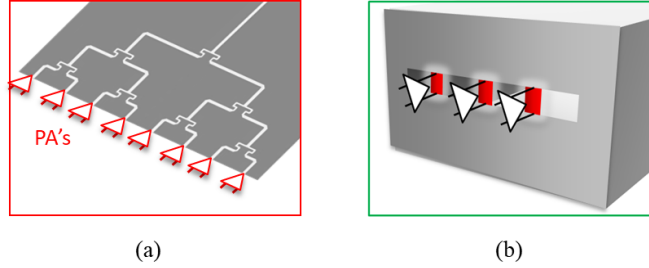


Figure 1.1: (a) Wilkinson power combiner. (b) Waveguide power combiner.

herty power combiner [15] can be implemented. The Doherty combiner connects and excites multiple PAs in such a way that the overall operating efficiency of the PAs is maximized for a range of output power. Examples of the implementation of a Doherty power combiner for 5G applications are presented in [16, 17].

In summary, there is a need to introduce power combiners that are not dispersive with frequency and simple to scale to a large number of inputs, while including the possibility to implement the Doherty configuration. The output of the power combiner is then typically connected to a radiating structure, thus the efficient integration of the combiner with an antenna is desired.

1.2. Pattern Shaping for Scan Loss Reduction at Millimeter Wave Frequencies

Besides the generation of sufficiently high power levels, an efficient mm-wave link requires the capability to radiate the power through optimal beam patterns. Thus, the possibility to achieve versatile radiation properties is a highly desired feature of mm-wave transmitters. For this reason, in both mm-wave communication and radar applications, radiation pattern diversity has become an attractive property for the antenna systems. For example, base stations in wireless cellular networks will comprise of antenna arrays that can switch between narrow or wide beams to achieve optimal capacity for different user distributions [18]. Multi-mode operation of antennas that can dynamically change the radiation beamwidth allows to reuse for multiple purposes the limited number of output channels available from mm-wave integrated circuits (ICs). Another advantage of implementing a single antenna system with a variable beamwidth, is the smaller area usage compared to two separate antennas.

The multi-mode operation can be simply achieved with digital excitation of antennas operating in free space. However, for well-defined scenarios where the beam efficiency is important (the radiated power needs to be mostly confined within the field of view $\pm\theta_{\text{design}}$), the use of wide angle impedance matching (WAIM) layers that support leaky waves can be beneficial. The leaky waves that propagate along the structure can focus the radiation in some desired directions [19]. Specifically here we target a double operation mode scenario. For one mode of operation we aim at a phased array capable of maintaining high gain over a wide scan range, up to $\pm 45^\circ$. The same array should also

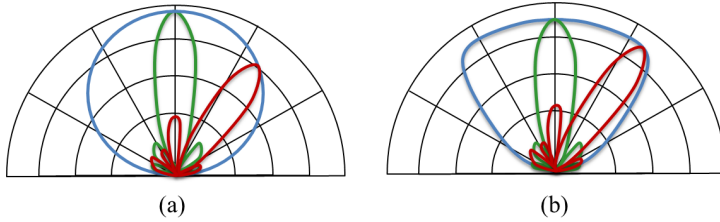


Figure 1.2: (a) Common element pattern where the array suffers from scan loss. (b) Pattern shaping to reduce scan loss.

be able to generate a single broad beam with a beamwidth up to $\pm 45^\circ$. The two modes of operation cannot be easily realized with an array in free space, while a superstrate supporting a leaky wave aiming at roughly $\theta_{\text{design}} = \pm 45^\circ$ can facilitate them both. In fact, phased arrays in free space are characterized by scan loss, i.e. a reduction of gain as a function of scan angle, as shown in Fig. 1.2(a). It is known that a WAIM layer such the one originally proposed in [20] can mitigate this problem. This electrically thin dielectric layer located in the close vicinity above a phased array antenna, by supporting a leaky wave that enhances the radiation towards a fixed direction compensates the scan loss. An example of pattern shaping to reduce scan loss is shown in Fig. 1.2(b), where it can be seen that the broadside gain and the gain while scanning are similar. Different types of WAIM structure have been subsequently investigated, using artificial dielectrics or metamaterials to improve the performance, either in scanning range or operational bandwidth [21–23]. Similarly an array of isotropic elements phased to first focus in the near field will naturally radiate a wide far field beam. However, to achieve a good beam efficiency over a limited angular range, the element pattern of each radiator can be controlled by the superstrate supporting leaky waves.

1.3. Antenna Concept

Both the mm-wave power combiners and the multi-mode arrays discussed in the previous sections necessitate the choice of a suitable antenna element.

1.3.1. Artificial Dielectric Layers for Integrated Transmitters

In the case of the waveguide combiner, the antenna should be integrated in the same PCB with the combiner in a compact and efficient manner. Such an integration is challenging because of the typical tradeoff between bandwidth, directivity and efficiency: electrically thick dielectric substrates provide wider bandwidth, but higher losses due to surface waves; on the contrary, electrically thin substrates would result in lower power being lost in surface waves, but narrow bandwidth and/or poor front-to-back ratio. The use of artificial dielectric layers (ADLs) in combination with the antenna was introduced in [24] as a solution to the surface wave problem.

The ADLs are multi-layer structures made of sub-wavelength periodic patches to realize an anisotropic artificial material. Recently, ADLs were exploited to improve the front-to-back ratio of integrated antennas at mm-wave frequencies [25, 26]. The main

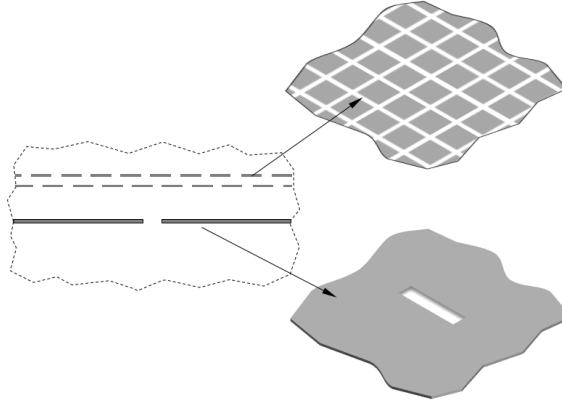


Figure 1.3: Antenna element with artificial dielectric superstrate under consideration for pattern shaping.

advantage of an ADLs compared to a real dielectric is the anisotropy, which is a key property to avoid the excitation of surface waves. Another application was proposed in [23, 27], where the ADLs were used in combination with planar connected arrays to achieve wideband and wide angle scanning phased array designs. The anisotropy of the ADLs allows enlarging the scan range with no scan blindness, while performing a wide-band impedance transformation, to widen the impedance matching bandwidth.

The power combiners presented in this thesis are connected to ADL-enhanced antennas. Two commonly used planar antennas are considered, i.e. a patch and a slot antenna. An example of an antenna element under consideration is shown in Fig. 1.3. It consists of a slot antenna in the presence of an artificial dielectric (AD) superstrate for enhanced performance.

1.3.2. Artificial Dielectric Layers for Pattern Shaping

The same antenna element can also be used as array element to realize an array with pattern shaping to reduce scan losses. We investigate the possibility of enhancing the radiation of single and multiple slot antennas by means of a WAIM realized using artificial dielectrics layers (ADLs). Being planar and very close to the array plane, the WAIM can be integrated with the array in a single printed circuit board (PCB). The analysis of the ADL is based on closed-form expressions to describe artificial dielectrics in the spectral domain [28–30]. The artificial dielectric superstrate supports leaky waves that can be optimized to enhance the gain in a specific angular region, [31–34]. The same concept was originally proposed, mainly within the scope of obtaining highly directive radiation [35]. As typical for WAIM or leaky wave antennas, the bandwidth of operation is inversely proportional to the leaky wave angle of radiation from broadside. Accordingly, when targeting relatively wide field of views, bandwidths that are viable for 5G communication application can be achieved.

1.4. Antenna Modeling

Regarding the modeling aspects of the radiating structure under analysis, fundamental studies are introduced both for the slot antenna element and the artificial dielectrics.

1.4.1. Modelling of the Slot Antenna

A convenient way to describe slot antennas is by equivalent transmission lines, where the excitation is modelled as a shunt generator and the slot arms are represented as two transmission line sections. These models can be used to aid the design of slot antennas with different loadings configurations or to compute efficiently the impedance characteristics of slots with a single or multiple feed points. However, existing models fail to accurately estimate the reactance at the slot terminations (and in turn the input impedance) and do not provide physical insight on the radiation mechanism.

In the thesis, an equivalent transmission line model for planar slots embedded in generic stratified media is described, based on a spectral domain analysis. The circuit is derived from a Method of Moment solution with only two basis functions, one defined on the feeding gap and the other at the shorted end of the slot. These basis functions are chosen to accurately account for the field diffractive behavior at the slot end points and for the reactive nature of the feed. The radiation is described in the model as resistances located at the feed and the end points. This approach allows representing the radiation from the slot as different space waves emerging from the feeding gap and the end points, with consequent gain in physical insight.

1.4.2. Modeling of Artificial Dielectric Layers

The analysis of the ADL is based on closed-form expressions of the equivalent reactance of each layer with a spectral domain method [28, 29, 36]. The previous works only contemplated z -periodic structures, where the layers of patches are all identical or alternatively shifted to realize a glide symmetric structure [37]. However, an interesting extension of these works would be a case with non-periodic characteristics along the z -direction. By allowing the layers to be different, one can imagine a gradual impedance transformer between the antenna impedance and free space impedance, to improve matching performance of the antenna.

Another limitation of the previously published analysis of ADLs is the square shape of the patches and the unit cell. Because of the square shape, many terms during the derivation of the analytical expression simplify, resulting in the decoupling of the TE and TM modes in the equivalent transmission line model. However, non-square patches allow for an extra degree of freedom in the design of matching layers with ADLs. For example, one can design the layers with the intent to shape the radiation pattern in the E- and H-plane separately.

A generalization of the method to account for z -aperiodic and non-square ADL structures is described in the thesis.

1.5. Scientific Contribution in this Thesis

- An improved model is proposed that accurately describes the reactive nature of both the feed and the terminations of a slot antenna. A Method of Moments (MoM)

solution is given where, by using the Green's function of an infinite slot [38], only two basis functions are employed to describe the current in the feeding gap and at the edges of the antennas.

- An equivalent transmission line model of the finite slot antenna is derived from the Method of Moments solution, by extracting the polar singularity contribution of the spectral domain Green's function as in [39, 40]. The model can be generalized to arbitrary stratified media, as long as the polar and the branch singularity do not coincide. Based on the MoM solution, the radiation from the slot is represented as three separate resistances, one associated with the feed point and two located at the edges.
- Closed form expressions are derived for the analysis of a non-periodic ADL structure. The structure is still doubly periodic in the x - y plane, but each layer along the z -axis can have different geometrical parameters, namely the gaps between patches, the distance and the shift to the layer above or below. The closed-form expressions can be used to design more complex non-uniform ADLs that can provide a variation of effective permittivity along the direction of stratification z .
- Another extension to the closed form expressions of the ADLs is done, allowing the geometrical parameters to differ in x - and y -direction. The equivalent transmission line circuit for these non-square ADLs is derived and it is shown that the TE and TM modes are no longer decoupled.
- A parallel plate waveguide (PPW) power combiner that also includes a Doherty scheme is proposed. When comparing with rectangular waveguide power combiners presented in [12, 13, 41], the PPW-based solution given here can achieve a much wider bandwidth, thanks to the nondispersive impedance characteristic of the PPW. Moreover, the concept is easily scalable to larger number of inputs, since the impedance of each feed is independent on the number of feeds.
- An array of slot antennas combined with ADLs is investigated to achieve pattern shaping and scan gain enhancement. The cavity between the array and the artificial dielectric superstrate supports leaky waves that can be optimized to enhance the gain in a specific angular region or to enlarge the array field-of-view. Superstrates that are electrically close to the radiating structure are considered, so that the leaky-wave radiation has low directivity and points at angles far from broadside. By controlling the amplitude and phase of the antenna elements, an adaptive array that can dynamically change its radiation beamwidth is realized.

1.6. Outline of the Thesis

This thesis, comprising the four topics mentioned above, is structured as follows:

- **Chapter 2**¹ presents a novel MoM-method to analyze semi-infinite and finite slot antennas. The basis functions and MoM-procedure are discussed and the method

¹The contents of this chapter have been published in [J.1].

is compared with full wave simulations. Besides this, an equivalent transmission line model is presented, where the characteristic impedance of the slot is found from its Green's function in the spectral domain, requiring that the pole and branch contributions to the spectral integral can be separated.

- In **Chapter 3**² closed form expressions for ADLs are presented for two novel cases. The first case that is studied has a non-periodic characteristic in the z -direction. Secondly, a situation where the patches and unit-cell of the ADLs are non-square is considered. Equivalent transmission circuits for both cases have been derived, where it is shown that for the non-square ADL the TE and TM modes are no longer decoupled.
- In **Chapter 4**³ the proposed solution for the efficient waveguide power combiner at mm-wave frequencies is described. A study on waveguide structures is presented, showing the most important impedance characteristics of a PPW to be used as combining structure. A Doherty combiner is implemented in the PPW combiner, in a hybrid series and parallel combiner. Two designs of 6-to-1 combiners are presented, one with a tapered impedance transformer and a connector as output and another where the PPW is directly integrated with a patch antenna. Simulations and measured results are presented, and a good comparison is shown.
- **Chapter 5** presents another design of a PPW power combiner, where the connection to an IC is taken into account. The connection to the IC comes with certain restrictions on the combining structure, specifically the feeding structure. A 4-to-1 power combiner is considered. Again, multiple structures are shown, one with a connector as output, and one with a cavity backed slot antenna.
- In **Chapter 6**⁴ an array of slot antennas in the presence of an ADL superstrate is considered, that reduces scan loss in the mm-wave frequency range. A study is presented on the trade-off between the gain enhancement due to the leaky wave and the mutual coupling between the antenna elements. A design is made of a four element array of cavity backed slots, that successfully reduces the scan losses of the array. Besides this, a multi-mode capability is shown where electronic control on amplitude and phase distribution of the excitation of the array allows for changing between a narrow, scanning beam, or a wide beam from the same array. A prototype is manufactured and measured results are presented, showing good agreement with simulations.
- In **Chapter 7** the most important conclusions of this thesis are presented, along with possible indications about future research directions.

²Parts of this chapter have been published in [C.7].

³The contents of this chapter have been submitted for publication in [J.3].

⁴The contents of this chapter have been prepared for publication in [J.4].

Chapter 2

Equivalent Circuit Models of Finite Slot Antennas

This chapter presents a systematic approach to describe planar slot antennas, embedded in generic stratified media. An equivalent transmission line model for the slot is proposed, based on a spectral domain analysis. First, we introduce a method of moments solution to model semi-infinite or finite slots, fed by a delta-gap excitation. The solution entails only two basis functions, one located at the feed and the other at the termination. The latter basis function is chosen to properly account for the field diffractive behavior at the antenna end points. An approximate circuit model is then introduced, which describes the main mode propagating along the slot as an equivalent transmission line. Lumped impedances are derived to accurately describe the source and the end points: the reactances account for the reactive nature of the feed and the termination, while the resistances represent the radiated space waves, emerging from both the feed and the end points. This procedure can be used to derive the input impedance of planar slot antennas with arbitrary length in generic layered media or the interaction between multiple feeds within the same slot.

2.1. Introduction

Printed slot antennas are among the most common planar antennas in use today and have been studied extensively in the literature, both as isolated elements and in array configurations. Their structure is complementary to the printed dipoles, thus all known analytical solutions of canonical dipole antennas can be applied also to slots by using Babinet's principle [42]. However, realistic slot antennas are not radiating in free-space but in the presence of a more complex dielectric stratification. In these cases, the input impedance is typically determined with general-purpose numerical methods.

A convenient way to describe a center-fed slot is by an equivalent transmission line, where the excitation is modeled as a shunt generator and the slot arms are represented as two transmission line sections. For example, equivalent transmission line models were used in [43–45] to aid the design of slot antennas with different loadings. To compute the

characteristic impedance and the propagation constant of the slot lines, different methods have been proposed in [46–49]. Several transmission line models for slot antennas are based on the solutions given in [50, 51]. In particular, the approach in [50] was based on equating the power radiated by the slot to the power delivered to a lossy transmission line. Moreover, both the models in [50, 51] considered short circuits to describe the slot terminations, thus did not account for the reactance associated with the end points. An improved model was proposed in [52], where the inductance of the slot shorted ends was considered.

A limit of all the mentioned models of finite slot antennas is that they do not account for the reactance of the feed and the diffraction from the edges. Besides, the radiation is modeled as a distributed resistance through a lossy line or as a single lumped resistance, thus it is not possible to separate the contributions to the radiated power that are emerging from the feed and from the end points.

A different approach is presented here, where an improved model is proposed that accurately describes the reactive nature of both the feed and the terminations of the slot. First, a Method of Moments (MoM) solution is given where, by using the Green's function of an infinite slot [38], only two basis functions are employed to describe the current in the feeding gap and at the edges of the antennas. The basis functions are appropriately chosen to represent the reactance due to the finite dimension of the feed and due to the diffraction of the electromagnetic field at the end points. Moreover, the MoM solution allows representing the radiation from the slot in terms of three separate resistances, one associated with the feed point and two located at the edges. Such configuration gives more physical insight, as the radiated field can be interpreted as three space waves, emerging from the feed and the end points.

An additional advantage of the proposed method is that the characteristic impedance of the transmission line is derived by extracting the polar singularity contribution of the spectral domain Green's function as in [39, 40]. The model can be generalized to arbitrary stratified media, as long as the polar and the branch singularity do not coincide.

2.2. MoM Solution for Semi-Infinite Slot

This section describes the steps for calculating the input impedance and the current distribution of a semi-infinite slot in an arbitrary stratification. The infinite slotline solution is given first, as it constitutes the basis for the theory described in the remainder of the paper. The termination of the slot is then introduced and described by means of an ad-hoc basis function that accounts for the diffraction at the slot edge.

2.2.1. Infinite Slot

Let us consider an infinite slot oriented along x in the presence of a generic dielectric stratification. For example, the slot can be in free-space, as shown in Fig. 2.1(a), or printed on a dielectric slab, as in Fig. 2.1(b). The slot is assumed to be electrically narrow and excited by a feeding gap, which is small in terms of wavelength (δ -gap excitation). The solution for the voltage along the slot can be found in [39] and can be written as a

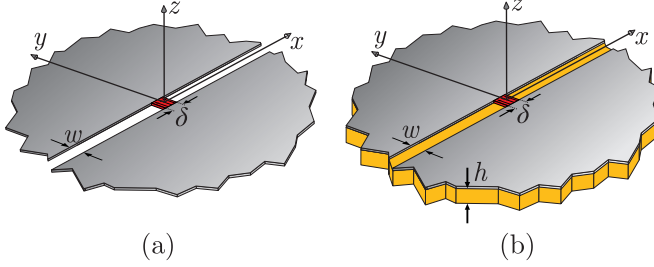


Figure 2.1: Infinite slot (a) in free-space and (b) printed on a dielectric slab.

one-dimensional inverse Fourier transform:

$$v(x) = \frac{1}{2\pi} \int_{-\infty}^{\infty} \frac{i_{\delta} F_{\delta}(k_x)}{D_s(k_x)} e^{-jk_x x} dk_x \quad (2.1)$$

where i_{δ} is the average current in the feeding gap, $F_{\delta}(k_x)$ is the spectral basis function representing the difference between the impressed tangential magnetic fields above and below the slot plane, exciting the gap:

$$F_{\delta}(k_x) = \text{sinc}\left(\frac{k_x \delta}{2}\right) \quad (2.2)$$

and

$$D_s(k_x) = \frac{1}{2\pi} \int_{-\infty}^{\infty} G_{xx}^{hm}(k_x, k_y) M_t(k_y) dk_y \quad (2.3)$$

is the spectral longitudinal Green's function of an infinite slot, defined in [38]. G_{xx}^{hm} is the xx -component of the spectral dyadic Green's function relating magnetic field to magnetic source, and k_x and k_y are the spectral counterparts of the spatial variables x and y , respectively. As the transverse current distribution is assumed to be edge-singular, its Fourier transform is the zeroth order Bessel function of the first kind $M_t(k_y) = -J_0(k_y, w/2)$. The integral in (2.3) can be solved analytically for free-space or for slots at the interface between two homogeneous media [38], while it can be computed numerically for generic stratification.

The input impedance of the infinite slot can be defined as the ratio of the average voltage (v_{δ}) and the average current (i_{δ}) over the feeding gap:

$$Z_{\text{in}} = \frac{v_{\delta}}{i_{\delta}} = \frac{\frac{1}{\delta} \int_{-\delta/2}^{\delta/2} v(x) dx}{i_{\delta}}. \quad (2.4)$$

By substituting (2.1) in (2.4) and evaluating the integral in dx , the input impedance can be expressed as a single spectral integral:

$$Z_{\text{in}} = \frac{1}{2\pi} \int_{-\infty}^{\infty} \frac{F_{\delta}(k_x) F_{\delta}(-k_x)}{D_s(k_x)} dk_x. \quad (2.5)$$

The integrands in (2.1) and (2.5) present square-root branch and polar singularities. The location of these singularities in the complex plane depends on the layered dielectric

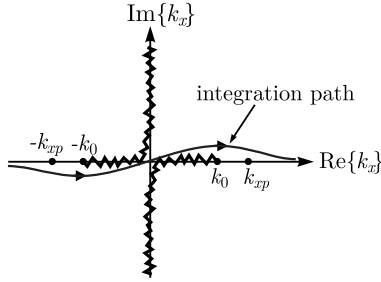


Figure 2.2: Branch cuts and poles in the complex k_x -plane for a slot with a thin dielectric substrate. The deformed integration path to avoid the singularities is also shown.

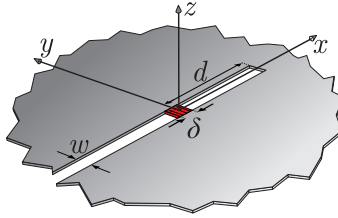


Figure 2.3: Semi-infinite slot in free-space.

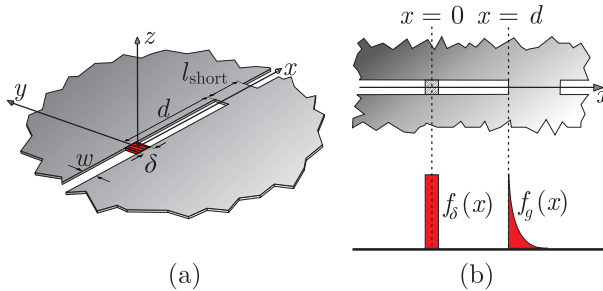


Figure 2.4: (a) Interrupted infinite slot in free-space; (b) Space domain basis functions with respect to their location along the semi-infinite slot.

medium under consideration. For example, for the geometry in Fig. 2.1(b), the branch points are in $k_x = \pm k_0$ and the poles are in $k_x = \pm k_{xp}$, as shown in Fig. 2.2. The integrals can be then solved numerically along the deformed path also shown in the figure.

2.2.2. Semi-Infinite Slot

Let us now consider a semi-infinite slot, interrupted at a certain distance, d , from the feeding gap, as depicted in Fig. 2.3. A convenient way to represent the semi-infinite slot is to assume that the short is realized with a metallic interruption of finite length l_{short} ,

as shown in Fig. 2.4(a). The length of the short is sufficiently large so that the magnetic current induced in the slot for $x > d + l_{\text{short}}$ does not influence the current at $x < d$. This assumption allows modeling a semi-infinite slot with infinitely extended metal (for $x > d$) as an infinite slot with a finite metal termination. Such an approximation is beneficial due to the availability of the infinite slot spectral Green's function in (2.3).

To represent the boundary conditions on the shorted end, an electric current is assumed to be distributed at $x > d$ with an edge-singular behavior, as shown in Fig. 2.4(b). The edge-singular behavior is assumed to be represented with the following basis function:

$$f_g(x) = \frac{2}{g\pi} \left(\frac{\text{rect}_{g/2}(x - (d + g/4))}{\sqrt{1 - \left(\frac{2(x - (d + g/2))}{g}\right)^2}} - 1 \right) \quad (2.6)$$

where $\text{rect}_l(x)$ is equal to 1 for $x \in [-l/2, l/2]$ and 0 elsewhere, and the parameter g in (2.6) is related to the width of the current distribution on the metallic interruption. The choice of the value for g is found to be linked to the width of the slot and the free-space wavelength λ as

$$g = \frac{5}{3} \sqrt{w\lambda}. \quad (2.7)$$

The expression for g has been derived empirically by curve fitting the numerical data obtained with a parametric analysis performed in CST. The accuracy of this expression will be later assessed by comparing our results for the slot input impedance with commercial electromagnetic solvers.

With the given choice of the basis functions, the voltage on the semi-infinite slot can be expressed similarly to (2.1) as follows [53]:

$$v(x) = \frac{1}{2\pi} \int_{-\infty}^{\infty} \frac{i_{\delta} F_{\delta}(k_x) + i_g F_g(k_x)}{D_s(k_x)} e^{-jk_x x} dk_x \quad (2.8)$$

where i_g is the average current on the metallic interruption and $F_g(k_x)$ is the Fourier transform of (2.6), which can be calculated in closed form as

$$F_g(k_x) = e^{jk_x g/2} \times \left(J_0\left(\frac{k_x g}{2}\right) - j\mathbf{H}_0\left(\frac{k_x g}{2}\right) - \frac{2}{\pi} \text{sinc}\left(\frac{k_x g}{4}\right) e^{-jk_x g/4} \right) \quad (2.9)$$

with \mathbf{H}_0 being the zeroth order Struve function.

The average voltage on the delta-gap feed (v_{δ}) and on the metallic interruption (v_g) can be expressed by Galerkin projection of (2.8) on the corresponding basis functions, which after some algebraic manipulations yields the following system of two linear equations [53]:

$$\begin{cases} v_{\delta} = i_{\delta} Z_{\delta\delta} + i_g Z_{\delta g} \\ v_g = i_{\delta} Z_{g\delta} + i_g Z_{gg} = 0 \end{cases} \quad (2.10)$$

where we imposed $v_g = 0$ for the perfect conducting termination. The mutual and self-impedances are given by

$$Z_{ji} = \frac{1}{2\pi} \int_{-\infty}^{\infty} \frac{F_i(k_x) F_j(-k_x) e^{jk_x(x_i - x_j)}}{D_s(k_x)} dk_x \quad (2.11)$$

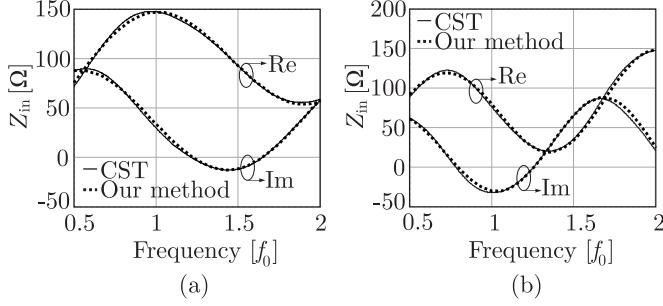


Figure 2.5: Comparison between the input impedance of a semi-infinite slot calculated with our method and CST for a slot (a) in free-space and (b) with a thin dielectric slab. The geometrical parameters of the structure are $d = \lambda_0/4$, $w = \lambda_0/50$ and $\delta = \lambda_0/40$, where λ_0 is the wavelength in free-space at f_0 . The dielectric substrate is characterized by $\epsilon_r = 4$, $h = \lambda_d/20$ when λ_d is the wavelength in the dielectric at f_0 .

where the subscripts i and j can refer to either δ or g , and the locations of the basis functions are defined as $x_\delta = 0$ and $x_g = d$. The input impedance of the slot can now be derived from (2.10) as the ratio between the average voltage and the current on the delta-gap:

$$Z_{in,MoM} = \frac{v_\delta}{i_\delta} = Z_{\delta\delta} - \frac{Z_{\delta g} Z_{g\delta}}{Z_{gg}}. \quad (2.12)$$

As a numerical example, Fig. 2.5(a) shows the input impedance of a semi-infinite slot in free-space calculated as described above, compared to CST. The distance between the excitation gap and the termination of the slot is $d = \lambda_0/4$, the width of the slot is $w = \lambda_0/50$ and the length of the delta-gap is $\delta = \lambda_0/40$, where λ_0 is the wavelength in free-space at the frequency f_0 . Figure 2.5(b) shows the input impedance of the same semi-infinite slot, when a thin dielectric substrate is added. The relative permittivity of the dielectric is $\epsilon_r = 4$ and the height of the slab is $h = \lambda_d/20$, where λ_d is the wavelength in the dielectric at f_0 . A very good agreement is observed in both examples.

2.3. Equivalent Transmission Line Circuit

Based on the numerical solution, an equivalent circuit model can be derived. The procedure entails the analysis of the polar and branch singularities of the spectral integral expressions of the impedances. The pole contributions to the integrals, when solved with the residue theorem, can be represented with equivalent transmission lines describing the guided propagation along the slot.

2.3.1. Residue Contribution of the Input Impedance of an Infinite Slot

The integrand in the impedance expression in (2.5) presents two types of singularities that can be recognized by writing the denominator $D_s(k_x)$ explicitly: square-root branch points, representing radiated space waves, and poles associated with quasi-TEM waves guided along the slot. When the poles and the branch points coincide, e.g. for a slot on perfectly conducting plane radiating in a homogeneous medium, the two contribu-

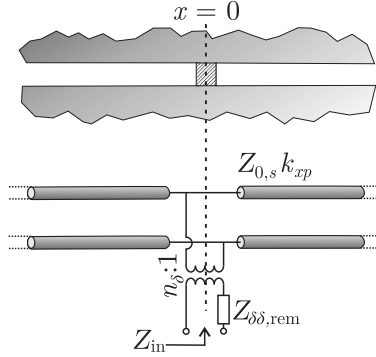


Figure 2.6: Equivalent transmission line of an infinite slot.

tions cannot be considered separately. In these cases, the integral in (2.5) can be solved asymptotically with the method in [54]. This approach allows writing the voltage on the slot for large values of $(x_i - x_j)$ as the solution of a tapered transmission line with x -dependent characteristic impedance, which is, however, not convenient to model multiple feed points or terminations.

To isolate the polar contribution from the branch, one can introduce small losses in the ground plane [39, 55] or a thin dielectric substrate, so that the pole singularity moves away from the branch point in the complex k_x -plane. The location of the pole, k_{xp} , can be found using a local-search algorithm (e.g. Newton's method) starting from an appropriate initial point.

By using Cauchy's residue theorem, the polar contributions of the input impedance of an infinite slot defined in (2.5) can be written as

$$Z_{\delta\delta,TL} = -j \frac{F_{\delta}(k_{xp})F_{\delta}(-k_{xp})}{D'_s(k_{xp})} = -j \frac{F_{\delta}(-k_{xp})^2}{D'_s(k_{xp})} \quad (2.13)$$

where the prime ($'$) indicates the operation of differentiation.

By representing the impedance as two parts, namely its residual contribution and a remaining term as

$$Z_{in} = Z_{\delta\delta,TL} + Z_{\delta\delta,rem} \quad (2.14)$$

the infinite slot can be represented by an equivalent circuit, as shown in Fig. 2.6. The model consists of two semi-infinite transmission line sections representing the slotline and a transformer with turn ratio $n_{\delta} = F_{\delta}(-k_{xp})$, in series with the impedance $Z_{\delta\delta,rem}$. The characteristic impedance of the transmission line is given by [39]

$$Z_{0,s} = -\frac{2j}{D'_s(k_{xp})}. \quad (2.15)$$

Figure 2.7 shows a comparison between the characteristic impedance of the transmission line calculated with (2.15) and the methods described in [47] and [49]. The characteristic impedance is calculated for a slotline in the presence of a dielectric slab

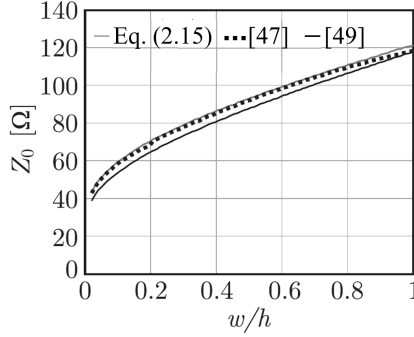


Figure 2.7: Comparison between the characteristic impedance of a slotline in the presence of a dielectric slab with $h = \lambda_0/40$ and $\epsilon_r = 10$. The characteristic impedance is shown as a function of the ratio between w and h .

of height $h = \lambda_0/40$ and a relative permittivity equal to $\epsilon_r = 10$, for the sake of comparison with [47] and [49]. It can be seen that the characteristic impedance as a function of the ratio between w/h corresponds well to the values found in previously published literature.

The resistance and reactance representing the radiation emanating from the feed and the reactive energy around the feed respectively, are represented as a lumped impedance, $Z_{\delta\delta,\text{rem}}$. This impedance is compared to values estimated by CST in Fig. 2.8, by calculating the input impedance of an infinite slot, and subtracting $Z_{\delta\delta,\text{TL}}$ as calculated with (2.13). The height of the dielectric slab is $h = \lambda_d/20$ and the relative permittivity of the material is $\epsilon_r = 4$. The value for $Z_{\delta\delta,\text{rem}}$ is shown for $\delta = \lambda_0/50$ and for $\delta = \lambda_0/100$ both for $w = \lambda_0/50$ in Fig. 2.8(a) and for $w = \lambda_0/100$ in Fig. 2.8(b). It can be seen that the real part of the impedance does not depend on the length of the gap. The reactance calculated with our method is slightly lower than the reactance found from CST. This difference is larger for wider slots and can be explained by the approximation of electrically narrow slots used to define $D_s(k_x)$ in (2.3).

2.3.2. Residue Contribution of the Mutual Impedance

Similarly, by using the residue theorem, the polar contributions of the mutual impedance $Z_{g\delta}$, defined in (2.11), can be written as

$$Z_{g\delta,\text{TL}} = -j \frac{F_\delta(k_{xp})F_g(-k_{xp})}{D'_s(k_{xp})} e^{-jk_{xp}d} \quad (2.16)$$

Figure 2.9 shows the comparison between the total integral $Z_{g\delta}$ and the contribution due to the residue $Z_{g\delta,\text{TL}}$, as a function of frequency. The slot under consideration is printed on a dielectric slab. It can be seen that the difference between the total mutual impedance and the residue contribution ($|Z_{g\delta} - Z_{g\delta,\text{TL}}|$) decreases with the frequency, since the distance between the two basis functions becomes larger in terms of the wavelength. This effect can be interpreted by noting that, for small distances, the interaction between the feed and the termination is not only described by the propagating mode

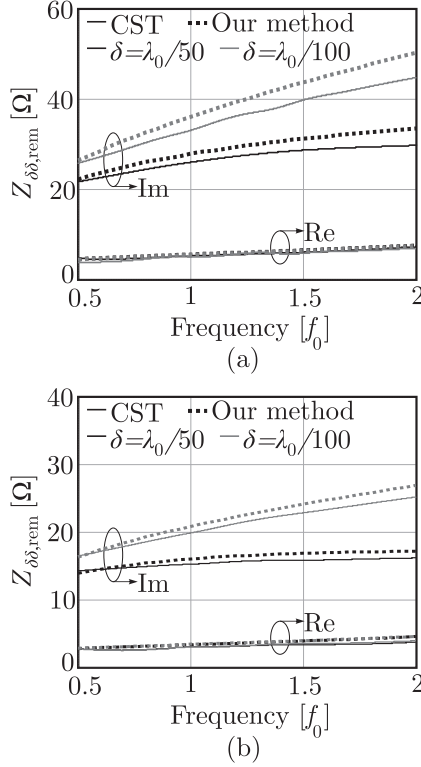


Figure 2.8: Comparison between the lumped impedance $Z_{\delta\delta,rem}$ as found using our method and extracted from CST. The slot is in the presence of a slab with $h = \lambda_d/20$ and $\epsilon_r = 4$. The impedances are shown for $\delta = \lambda_0/50$ and for $\delta = \lambda_0/100$. (a) $w = \lambda_0/50$. (b) $w = \lambda_0/100$.

(residue) but also by space-wave coupling. For larger distance, the space wave contribution is less important, due to its geometrical spreading, thus the residue component, which has no spreading, becomes dominant.

By approximating the mutual impedance with its residual contribution, the equivalent model introduced for infinite slots can be extended to semi-infinite slots as shown in Fig. 2.10(a). An additional impedance transformer is included at the termination of the slot with turn ratio $n_g = F_g(-k_{xp})$. Similarly to (2.13) and (2.14), we can define the contribution of the transmission line to the self-impedance of the edge basis function as

$$Z_{gg,TL} = \frac{1}{2} Z_{0,s} n_g^2 = -j \frac{F_g(-k_{xp})^2}{D'_s(k_{xp})} \quad (2.17)$$

and the remaining contribution to the total self-impedance as

$$Z_{gg,rem} = Z_{gg} - Z_{gg,TL}. \quad (2.18)$$

The length of the transmission line section separating the two transformers is equal to the distance between the feeding point and the metallic interruption (d).

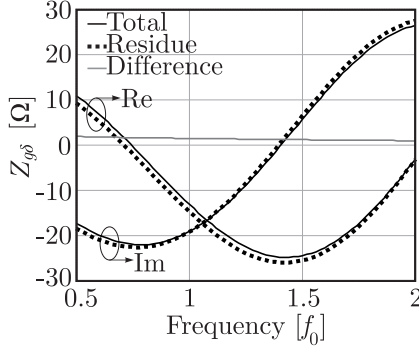


Figure 2.9: Comparison between the total mutual impedance $Z_{g\delta}$ and the contribution due to the residue as a function frequency. The geometrical parameters are set to: $d = \lambda_0/4$, $w = \lambda_0/50$, $\delta = \lambda_0/40$, $\lambda_d/20$ and $\epsilon_r = 4$.

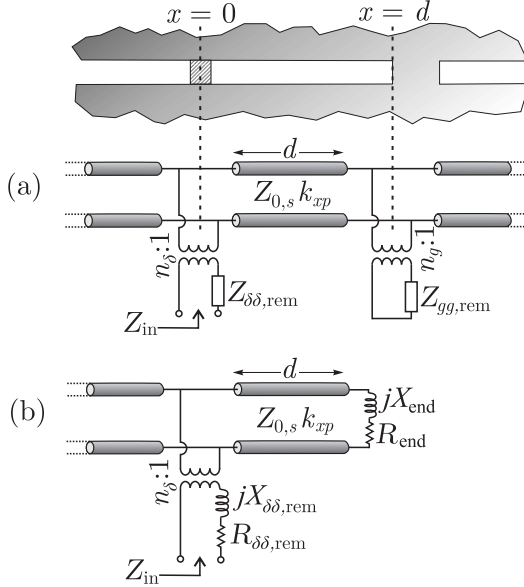


Figure 2.10: Equivalent transmission line of the semi-infinite slot: (a) transformers and impedances associated with the feeding point and the termination, in parallel to an infinite line; (b) lumped equivalent termination impedance.

We can also define a single lumped impedance to represent the end point as

$$Z_{\text{end}} = \frac{\left(Z_{gg,\text{rem}}/n_g^2 \right) Z_{0,s}}{\left(Z_{gg,\text{rem}}/n_g^2 \right) + Z_{0,s}} = R_{\text{end}} + jX_{\text{end}}. \quad (2.19)$$

The end-point impedance can be represented as a resistor accounting for radiation

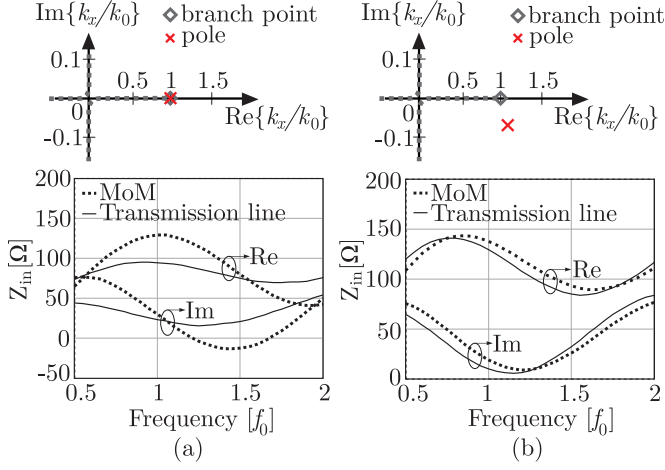


Figure 2.11: Comparison between the input impedance of a semi-infinite slot in a lossy ground plane calculated with our method and CST for (a) $\sigma = 6 \times 10^7$ S/m and (b) $\sigma = 1000$ S/m. The geometrical parameters of the structure are $d = \lambda_0/4$, $w = \lambda_0/90$ and $\delta = \lambda_0/90$. The locations of the pole with respect to the branch point are also shown.

and an inductor accounting for the reactive energy at the termination, such that the equivalent circuit of the semi-infinite slot becomes as in Fig. 2.10(b).

2.3.3. Input Impedance and Accuracy of the Circuit Model

The input impedance of the slot can be found from the circuit as

$$Z_{\text{in,TL}} = Z_{\delta\delta,\text{rem}} + n_{\delta}^2 \frac{Z_{\text{end}}^{\text{rep}} Z_{0,s}}{Z_{\text{end}}^{\text{rep}} + Z_{0,s}} \quad (2.20)$$

where

$$Z_{\text{end}}^{\text{rep}} = Z_{0,s} \frac{Z_{\text{end}} + j Z_{0,s} \tan(k_{xp} d)}{Z_{0,s} + j Z_{\text{end}} \tan(k_{xp} d)}. \quad (2.21)$$

Figure 2.11 shows the comparison between the input impedance of a semi-infinite slot in free-space calculated using the previously introduced method of moments and with the transmission line model. The distance between the end point of the slot and the feeding gap $d = \lambda_0/4$, the width of the slot is $w = \lambda_0/90$ and the length of the feeding gap is $\delta = \lambda_0/90$. Two different conductivities of the ground plane are considered: $\sigma = 6 \times 10^7$ S/m (copper) and $\sigma = 1000$ S/m. The corresponding distances between k_{xp} and k_0 are $0.0003k_0$ and $0.11k_0$, respectively, as shown in the figure. It can be seen that for $\sigma = 6 \times 10^7$ S/m the transmission line does not describe the input impedance accurately, as the distance between the pole k_{xp} and the branch point k_0 in the complex k_x -plane is too small to separate the two contributions. In the case when $\sigma = 1000$ S/m this distance is larger, thus the polar contribution can be extracted and represents the wave launched along the slot better.

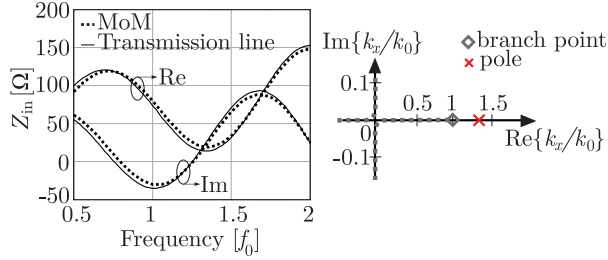


Figure 2.12: Comparison between the input impedance of a semi-infinite slot on a dielectric substrate calculated with the transmission line model and the MoM. The geometrical parameters of the structure are $d = \lambda_0/4$, $w = \lambda_0/50$, $\delta = \lambda_0/40$, $h = \lambda_d/20$ and $\epsilon_r = 4$. The location of the pole with respect to the branch point is also shown.

Figure 2.12 shows a similar comparison when a small dielectric is introduced. The dimensions of the structure are the same as in Fig. 2.5(b). The presence of a thin dielectric is an effective way to separate the space wave and the guided wave contributions. Indeed, a good accuracy of the equivalent transmission line model can be observed in Fig. 2.12, as the distance between k_{xp} and k_0 is $0.34k_0$ at $f = f_0$.

As pointed out earlier, the accuracy of the equivalent transmission line model depends on the distance d between the feed and the end point. This dependence can be explained by the space-wave interaction between the two basis functions, that is not accounted for in the transmission line model. The space-wave coupling can be comparable to the guided-wave interaction for small distances, but its effect has less and less impact as the distance increases, due to the spherical spreading of the space wave. To highlight this effect, Fig. 2.13 shows the relative error of the input impedance of a semi-infinite slot calculated with the transmission line circuit, as a function of the distance d , for three values of the width w . The relative error is defined as

$$\epsilon_{\text{rel}} = \frac{|Z_{\text{in,MoM}} - Z_{\text{in,TL}}|}{|Z_{\text{in,MoM}}|} \times 100\%. \quad (2.22)$$

The slot has a feeding gap with size $\delta = \lambda_0/40$ and is printed on a thin dielectric substrate, with height $h = \lambda_d/20$ and relative permittivity $\epsilon_r = 4$. It can be seen that the relative error decreases as a function of the distance. The periodic peaks in the relative error correspond to minima in the impedance, with values that are close to zero, thus in these points small absolute errors correspond to high relative errors. Moreover, narrower slots yield smaller errors, because of reduced radiation associated with the basis functions and more dominant guiding effect along the slot.

2.3.4. Finite Slot

When considering a finite slot, as depicted in Fig. 2.14(a), the edge-singular electric current is induced on both metallic interruptions. For a center-fed finite slot, the MoM solution can be then derived in the same way as for the semi-infinite slot, by replacing the basis function edge basis function $f_g(x)$ with a pair of such basis functions at the two edges $f_g^{\text{double}}(x)$, as shown in Fig. 2.14(b). Due to symmetry, the two edge-singular

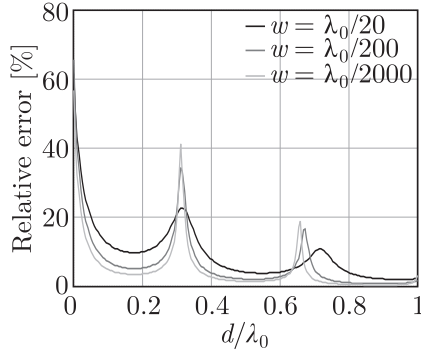


Figure 2.13: Relative error with respect to the input impedance for the transmission line circuit, representing a semi-infinite slot on a thin dielectric substrate, as a function of the distance between the feeding point and the end of the slot, d . The length of the feeding gap is $\delta = \lambda_0/40$. The relative permittivity of the dielectric is $\epsilon_r = 4$ and the height of the slab is $h = \lambda_d/20$.

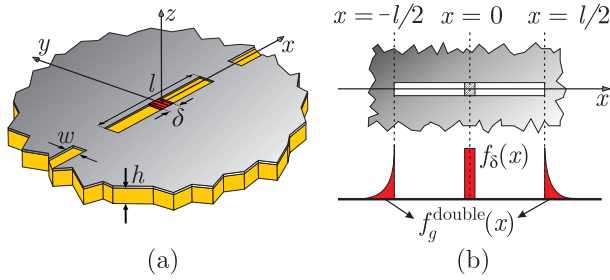


Figure 2.14: (a) Finite slot on a dielectric substrate and (b) space domain basis functions with respect to their location along the finite slot.

currents at the edges have the same amplitude, thus the basis functions can be written in the spectral domain as:

$$F_g^{\text{double}}(k_x) = F_g(k_x) e^{jk_x l/2} + F_g(-k_x) e^{-jk_x l/2} \quad (2.23)$$

where l is the length of the slot. Following the procedure described earlier, the equivalent transmission line model for the finite slot becomes the one in Fig. 2.15(a). If the two arms of the slot are equal, the input impedance of the slot can be found from the circuit as

$$Z_{\text{in}} = Z_{\delta\delta, \text{rem}} + n_{\delta}^2 \frac{1}{2} Z_{\text{rep}}^{\text{end}} \quad (2.24)$$

where $Z_{\text{rep}}^{\text{end}}$ is defined in (2.21). Figure 2.15(b) shows the input impedance of a finite slot in the presence of a dielectric substrate calculated using our MoM solution, a CST simulation and the equivalent transmission line model. The length of the slot is $l = \lambda_0/2$, the width of the slot is $w = \lambda_0/50$ and the length of the delta-gap is $\delta = \lambda_0/40$. The relative permittivity of the dielectric is $\epsilon_r = 4$ and the height of the substrate is $h = \lambda_d/20$. A very

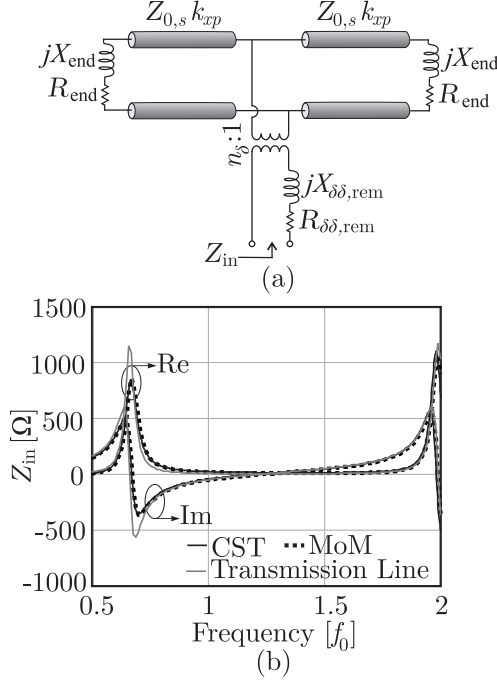


Figure 2.15: (a) Equivalent transmission line circuit representing a finite slot. (b) Comparison between the input impedance of a finite slot in the presence of a dielectric substrate calculated with the transmission line model, our MoM and CST. The geometrical parameters of the structure are $l = \lambda_0/2$, $w = \lambda_0/50$, $\delta = \lambda_0/40$, $\epsilon_r = 4$, $h = \lambda_d/20$.

good agreement between the MoM and CST is observed. The transmission line model also describes well the resonance frequencies and the values of the impedance. The accuracy of the approximated transmission line model is better for higher frequency, for which the electrical distance between the feed and the slot ends is larger.

2.4. Analysis of the Slot Termination

In the previous sections an impedance has been introduced, which describes the end point of the slot. A more detailed analysis of the characteristic behavior of the fields close to the termination is presented in this section, with the aim to provide more physical insight to the reactive and radiative nature of the end point as a function of the slot width.

2.4.1. Voltage Distribution on the Slot

To this purpose, Fig. 2.16 shows the voltage along the semi-infinite slot calculated with the MoM and with the transmission line circuit. For example, we assume that the feeding gap is centered at $x = 0$, the termination is located at $x = \lambda_0$ and the slot is infinitely extended for $x < 0$. Two cases are considered for the slot width: $w = \lambda_0/20$ in Fig. 2.16(a) and $w = \lambda_0/2000$ in Fig. 2.16(b), with λ_0 being the wavelength at the calculation fre-

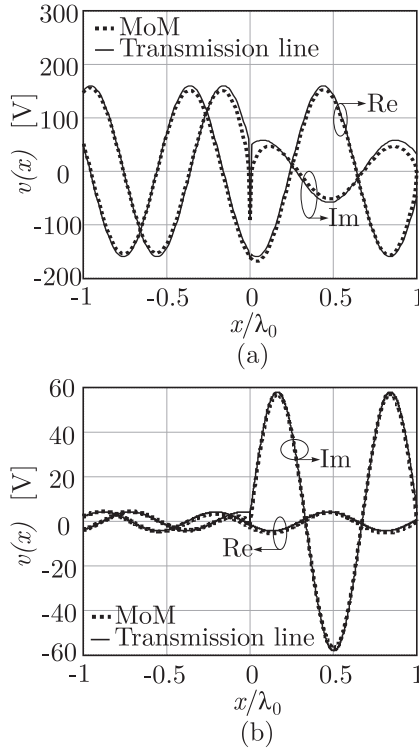


Figure 2.16: Comparison between the voltage along a semi-infinite slot on a dielectric substrate calculated with the transmission line model and the MoM, for slot of width (a) $w = \lambda_0/20$ and (b) $w = \lambda_0/2000$. The excitation current is $i_\delta = 1\text{A}$, the geometrical parameters of the structure are $d = \lambda_0$, $\delta = \lambda_0/500$, $h = \lambda_d/20$ and $\epsilon_r = 4$.

quency f_0 . In the transmission line, the voltage along the line is described by the sum of two forward and backward traveling sine waves, while in the MoM solution the voltage is given by (2.8). Clear differences can be seen between the two methods in the proximity of the feeding gap and the end point, for the larger slot width in Fig. 2.16(a). The voltage calculated using the transmission line model is not zero at the end point, but equal to the voltage across the load Z_{end} . On the contrary, the voltage calculated with the MoM goes to zero at the end point, but it deviates from the sinusoidal distribution close to the termination. For the narrower slot in Fig. 2.16(b), the discrepancy near the discontinuities is much less apparent.

The deviation from the sine profile can be explained by observing the real field distribution on the slot, evaluated with a three-dimensional full-wave method. The electric field along the slot is oriented in the transverse direction, as the tangential component of the electric field on a perfect electric conductor must be zero. However, near the end of the slot, the field lines bend in order to be normal to the metal on all three sides. This effect can be observed in Fig. 2.17(a), which depicts the vector field lines near the edge,

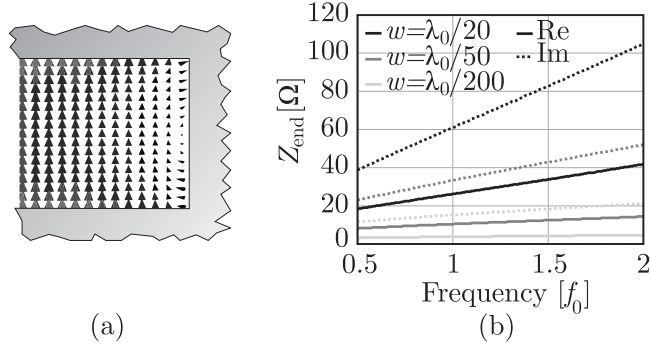


Figure 2.17: (a) Electric field vector lines inside a semi-infinite slot near the end point; (b) Values of the end-point impedance Z_{end} as a function of frequency for three different widths of a semi-infinite slot on a dielectric substrate. The height of the substrate is $h = \lambda_d/40$ and the relative permittivity is $\epsilon_r = 4$.

calculated in CST. Since the magnetic current (or the voltage) along the slot is orthogonal to the electric field, the magnetic current also bends. This bending is more significant for wider slot and gives rise to a reactive field concentrated around the termination, as well as space waves radiated in all directions.

For very narrow slots, the voltage near the end point follows more closely the sinusoidal behavior, i.e. the voltage reflection coefficient at the termination is closer to -1 and the end-point impedance is more similar to a short circuit. Figure 2.17(b) shows the value of Z_{end} for different slot widths. It can be seen that, indeed, both the inductance and the radiation resistance associated with the end point decrease for narrower slots.

2.4.2. Power Balance

The transmission line circuit can be used to find the power radiated from the feeding gap and from the end point of the slot, as well as the power launched in the semi-infinite slotline. The radiated power, P_{rad} , is found as the sum of the power dissipated in $R_{\delta\delta,\text{rem}}$ and R_{end} , while the power launched along the slotline in the form of a quasi-TEM wave is indicated as P_{TEM} . In order to compare the values of radiated power calculated with our circuit and with CST, a constant power equal to 0.5 W is fed to the structure by a generator with an internal impedance Z_{gen} . The accepted power, entering the circuit, can be found as

$$P_{\text{acc}} = 0.5(1 - |S_{11}|^2) = P_{\text{rad}} + P_{\text{TEM}} \quad (2.25)$$

where $S_{11} = (Z_{\text{in}} - Z_{\text{gen}})/(Z_{\text{in}} + Z_{\text{gen}})$. Figure 2.18 shows the comparison of the power balance calculated with the circuit and from CST, showing a good agreement. The structure under consideration is a semi-infinite slot, on a thin dielectric slab, with parameters $w = \lambda_0/50$, $\delta = \lambda_0/40$, $d = 0.45\lambda_0$, $h = \lambda_d/20$ and relative permittivity of the dielectric $\epsilon_r = 4$. The generator impedance is equal to $Z_{\text{gen}} = 100\Omega$. It can be noted that the power launched in the semi-infinite slot is maximum at the frequencies where the length of the shorted stub is an odd multiple of $\lambda_{\text{eff}}/4$, where λ_{eff} is the effective wavelength of the transmission line at f_0 . For this condition, low radiation occurs. On the contrary, when

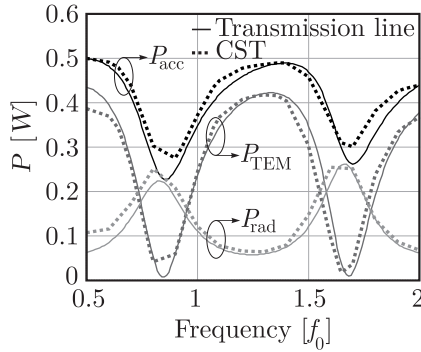


Figure 2.18: Comparison between the radiated power and the power launched into the semi-infinite slotline calculated with the equivalent circuit and CST. The geometrical parameters are: $w = \lambda_0/50$, $\delta = \lambda_0/40$, $d = 0.45\lambda_0$, $h = \lambda_d/20$, $\epsilon_r = 4$ and $Z_{\text{gen}} = 100\Omega$.

the length d is a multiple of $\lambda_{\text{eff}}/2$, the impedance seen from the terminated arm is much lower than the slot characteristic impedance, thus almost the entire accepted power is radiated.

Another interesting property of the derived transmission line model is the possibility to quantify the portion of radiated power that is associated with the feed point and the terminations of the slot, $P_{\text{rad},\delta}$ and $P_{\text{rad},\text{end}}$, respectively. Figure 2.19 shows the power balance of a semi-infinite (a) and a finite slot (b) in the presence of a dielectric slab. The slot parameters are $w = \lambda_0/20$, $\delta = \lambda_0/40$, $h = \lambda_d/20$ and $\epsilon_r = 4$ for both cases. In Fig. 2.19(a), the distance between the feeding gap and the end point is $d = \lambda_{\text{eff}}/4$ and the generator impedance is equal to $Z_{\text{gen}} = 100\Omega$. The length of the slot in Fig. 2.19(b) is $l = \lambda_{\text{eff}}/2$ and the generator impedance is equal to $Z_{\text{gen}} = 300\Omega$.

It can be seen that, for the semi-infinite slot in 2.19(a), the radiated power emerges in approximately equal parts from the feed and the end point, independently on the length of the stub. A different condition occurs in the case of a finite slot, in Fig. 2.19(b), for which most of the power is radiated from the terminations, when the slot length is resonant ($l = \lambda_{\text{eff}}/2$). This observation suggests that, since the semi-infinite slot is non-resonant, the radiation appears to emerge equally from the feed and the termination. Such a property is also exploited in connected arrays of slots [56], which consist of long slots periodically fed at multiple points to achieve wideband performance. Also in this case, because of the non-resonant property, the power is radiated evenly from all the feeding gaps of the array, effectively generating a uniform field distribution over the antenna aperture.

The resonant slot exhibits an opposite behavior, where the terminations have a dominant contribution to radiation compared to the feeding gaps. Indeed, in this condition, the currents are low at the feed location and very high at the end points.

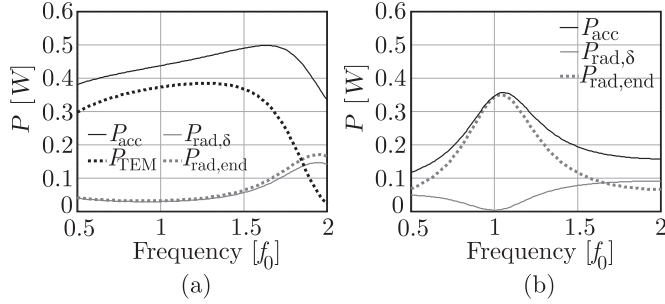


Figure 2.19: Power balance of a (a) semi-infinite slot with $d = \lambda_{eff}/4$ and $Z_{gen} = 100\Omega$. (b) finite slot with $l = \lambda_{eff}/2$ and $Z_{gen} = 300\Omega$. The slots are printed on a dielectric substrate. The remaining geometrical parameters are $w = \lambda_0/20$, $\delta = \lambda_0/40$, $h = \lambda_d/20$ and $\epsilon_r = 4$.

2.5. Multiple Feeding Points

The analysis can be extended to include multiple feeding points along the slot, as shown in Fig. 2.20(a). In this case, the MoM solution presented in Sec. 2.3.4 can be extended by adding extra basis functions for each feeding point. The resulting numerical method is very efficient since the total number of basis functions is equal to the number of feeds plus two for the terminations of the slot. A successful application of this method is the analysis of finite array performance in connected slot arrays [57]. The MoM shown here can enable the simulation of large arrays, even in the presence of artificial dielectrics, that otherwise would be impractical with a general purpose commercial solver.

Besides the efficient numerical analysis, the equivalent transmission line model can be generalized to account for multiple feeds. The additional feeding points are represented in the transmission line by adding multiple transformers with impedances $Z_{\delta\delta,rem}$ and generators, as shown in Fig. 2.20(b). This representation is convenient to visualize the mutual coupling between different feeds in a slot in terms of waves propagating in the transmission line, which represent waves guided by the slot. Moreover, the different contributions to the total power radiated can be evaluated by finding the power dissipated in the individual radiation resistances associated with the feeds and the terminations.

As an example we consider a slot with two feeding points, separated by $l_{sep} = \lambda_0$ and the distance to the edges is $l_{edge} = \lambda_0$. The width of the slot is $w = \lambda_0/40$ and the size of the delta-gap is $\delta = \lambda_0/30$. The slot is printed on a thin dielectric slab with $h = \lambda_d/40$ and $\epsilon_r = 4$. The active impedance seen from the ports can be found by applying the superposition principle and considering the contribution from each feed separately. The two generator impedances are $Z_{gen,1} = Z_{gen,2} = 50\Omega$. Figure 2.21 shows a comparison between the active impedance calculated using the transmission line model and CST. A good agreement can be observed.

2.6. Conclusions

An equivalent transmission line model for planar slots embedded in generic stratified media was presented. The procedure started with deriving an efficient method of mo-

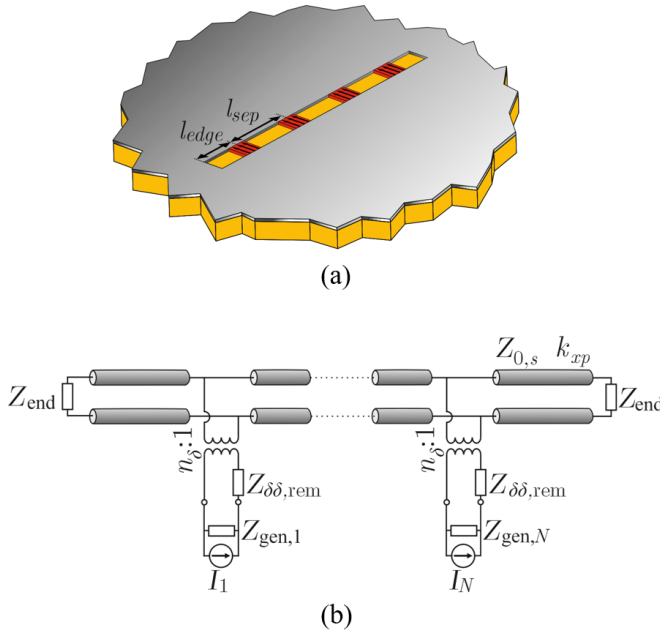


Figure 2.20: (a) Slot with multiple feeding points printed on a dielectric slab. (b) Equivalent transmission line model of a finite slot with multiple feeding points.

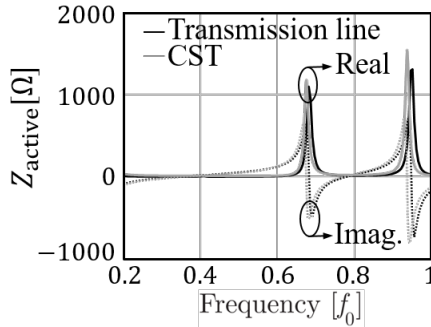


Figure 2.21: Comparison between the active impedance of a slot with two feeding points calculated with the equivalent transmission line model and CST. The geometrical parameters are $l_{sep} = \lambda_0$, $l_{edge} = \lambda_0$, $w = \lambda_0/40$, $\delta = \lambda_0/30$, $h = \lambda_d/40$, $\epsilon_r = 4$ and $Z_{gen,1} = Z_{gen,2} = 50 \Omega$

ments solution for semi-infinite slots, with only two basis functions, one located at the feeding point and one at the termination of the slot. The basis functions were chosen such that they properly account for the reactive energy localized at these points. The procedure was then extended to a double termination, as to find the input impedance of a finite slot antenna with arbitrary length.

Based on the numerical solution, an equivalent transmission line circuit was derived, by extraction of the pole contribution from the mutual impedance integrals. To be able to separate the residue contribution from the space wave, a thin dielectric slab or losses in the metal can be introduced. The radiation is described in the model as resistances located at the feed and the end points. This approach allows representing the radiation from the slot as the generation of different space waves, one associated with the feeding gap and two emerging from the end points. The physical dimensions and the shape of the basis functions was accounted for in the circuit by means of transformers.

Chapter 3

Closed-Form Analysis of Artificial Dielectrics with Non-Identical or Non-Square Layers

This chapter presents a general analysis to describe non-periodic artificial dielectric layers (ADLs). Closed-form expressions for the equivalent layer impedance are given for generic plane-wave incidence, assuming that each individual layer can differ from the others in terms of geometrical parameters. By dropping the assumption of identical layers, the given formulas are of more general applicability for flexible designs artificial dielectric slabs that are not uniform along the stratification. Also, non-square patches are considered, where the ADLs have different dimensions in the x - and y -directions. Such rectangular patches provide more degrees of freedom and allow optimization of the two planes separately. The analytical expressions account for the interaction between layers due to higher-order Floquet modes, thus remain valid for arbitrarily small electrical distance between layers.

3.1. Introduction

For the electromagnetic modeling of ADLs, a number of numerical solutions proposed for the efficient analysis of generic multilayer metasurfaces can be used, for example [61–63]. More recently, analytical formulas to describe ADLs were presented in [24, 28] for aligned layers (Fig. 3.1(a)) and generalized in [29] to include a shift between even and odd layers (Fig. 3.1(b)). An extension of the method to include the finite conductivity of the metal was presented in [36]. All the mentioned works provide a transmission line model to represent the propagation of a generic plane wave within the ADLs. In such equivalent circuit, each layer is represented as an equivalent shunt impedance, which can be expressed in closed-form as a function of the geometrical parameters of the ADLs. Compared to other works with similar scope [64–66], the equivalent impedances in [29, 36] include the reactive coupling between layers due to higher-order Floquet modes. Given the very small electrical distance between layers in typical ADL

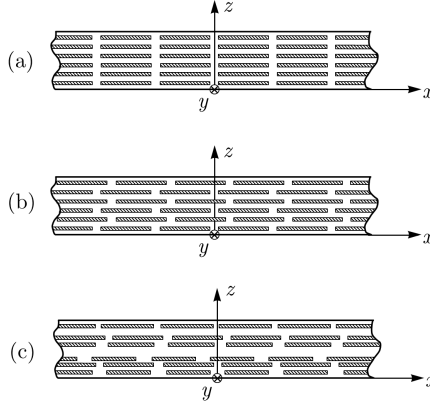


Figure 3.1: Two-dimensional side view for artificial dielectric slabs with (a) aligned, (b) shifted and (c) non-periodic layers along z .

designs, such coupling is very large and must be taken into account.

The previous works [28, 29, 36] only contemplated z -periodic structures, where the layers of patches are all identical, aligned as in Fig. 3.1 (a) or alternatively shifted to realize a glide symmetric structure [37] as in Fig. 3.1 (b). In this chapter, we propose a technique to generalize the method to deal with non-periodic structure, as the one depicted in Fig. 1(c). The structure is still doubly periodic in the x - y plane, but each layer along the z -axis can have different geometrical parameters, namely the gaps between patches, the distance and the shift to the layer above or below. The closed-form expressions given here can be used to design more complex non-uniform ADLs that can provide a variation of effective permittivity along the direction of stratification z .

Another limitation of the previously published analysis of ADLs is the square shape of the patches and the unit cell. Because of the square shape, many terms during the derivation of the analytical expression simplify, resulting in the decoupling of the TE and TM modes in the equivalent transmission line model. However, non-square patches allow for an extra degree of freedom in the design of matching layers with ADLs. For example, one can design the layers with the intent to shape the radiation pattern in the E- and H-plane separately. Another useful application of ADLs with non-square characteristics is the design of polarizers. Due to the difference in the geometrical parameters in x - and y -directions, the TE and TM modes are no longer decoupled, allowing for example to generate a circular polarized signal from a linear polarized signal.

3.2. z -Aperiodic Artificial Dielectric Layers

This section describes the derivation of the closed-form expressions for the analysis of z -aperiodic ADLs. First the problem definition is explained and the impedances in the equivalent transmission line model are found. Hereafter the model is validated by comparison with full wave simulation results.

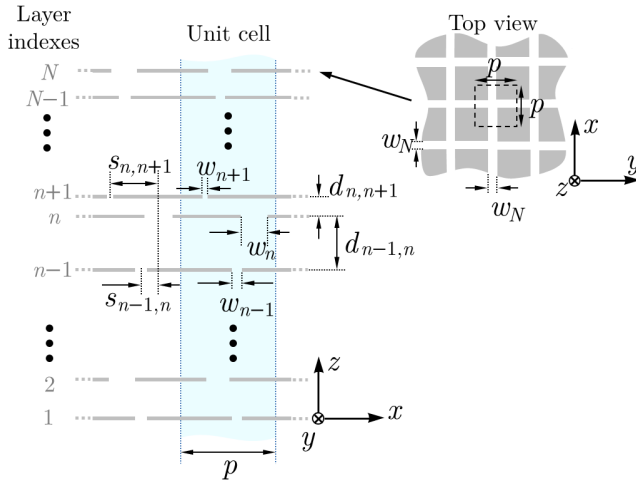


Figure 3.2: Cross section view of the unit cell of z -aperiodic ADLs, with definition of the geometrical parameters.

3.2.1. Problem Definition and Equivalence Principle

The geometry under consideration is shown in Fig. 3.2 and consists of N layers with indexes $n \in [1, 2, \dots, N]$. Each layer is an array of perfectly conducting square patches, infinitely thin along z and doubly periodic in the transverse dimensions. The periods are equal along x and y and given by p . Although the transverse periods are assumed to be the same for all the layers, all other geometrical parameters can vary in each layer and they are function of the index n . The gaps between the patches in the n -th layer are characterized by width w_n both along x and y . The distance between any pair of contiguous layers, with indexes n and $n + 1$, is denoted by $d_{n,n+1}$ and can change arbitrarily along the stratification. Also the mutual shift between adjacent layers $s_{n,n+1}$ can vary with n and can be an arbitrary portion of the unit cell.

A plane wave is assumed to propagate in the negative z -direction within the ADL structure. By applying the Schelkunoff's equivalence principle [67], three surfaces S_{n+1} , S_n and S_{n-1} are defined as in Fig. 3.3(a) and they are filled with a perfect electric conductor (Fig. 3.3(b)) so that two closed regions are created. Equivalent surface magnetic currents \mathbf{m}_n can be defined in correspondence of the gaps in the original problem. These current densities $\mathbf{m}_n(\boldsymbol{\rho}; w_n)$ are functions of the position $\boldsymbol{\rho} = x\hat{\mathbf{x}} + y\hat{\mathbf{y}}$ and depend on the width of the gaps w_n characteristic of the n -th layer.

Due to the image theorem, the magnetic currents radiating within parallel plate waveguides are equivalent to an infinite number of current contributions radiating in free space, as described in Fig. 3.4. The continuity of the transverse scattered magnetic field at the n -th layer (assumed to be located at $z = 0$) can be expressed as:

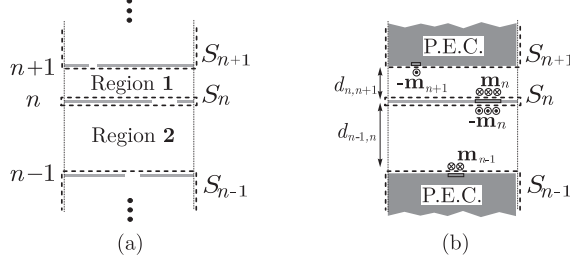


Figure 3.3: (a) Original problem and (b) equivalent problem with unknown magnetic current distributions.

$$\begin{aligned}
& \sum_{i \text{ even}} \int_{-\infty}^{\infty} \int_{-\infty}^{\infty} 2\mathbf{m}_n(\boldsymbol{\rho}'; w_n) \mathbf{g}(\boldsymbol{\rho} - \boldsymbol{\rho}', i d_{n,n+1}) d\boldsymbol{\rho}' - \\
& \sum_{i \text{ odd}} \int_{-\infty}^{\infty} \int_{-\infty}^{\infty} 2\mathbf{m}_{n+1}(\boldsymbol{\rho}'; w_{n+1}) \mathbf{g}(\boldsymbol{\rho} - \boldsymbol{\rho}', i d_{n,n+1}) d\boldsymbol{\rho}' + \\
& \sum_{i \text{ even}} \int_{-\infty}^{\infty} \int_{-\infty}^{\infty} 2\mathbf{m}_n(\boldsymbol{\rho}'; w_n) \mathbf{g}(\boldsymbol{\rho} - \boldsymbol{\rho}', i d_{n-1,n}) d\boldsymbol{\rho}' - \\
& \sum_{i \text{ odd}} \int_{-\infty}^{\infty} \int_{-\infty}^{\infty} 2\mathbf{m}_{n-1}(\boldsymbol{\rho}'; w_{n-1}) \mathbf{g}(\boldsymbol{\rho} - \boldsymbol{\rho}', i d_{n-1,n}) d\boldsymbol{\rho}' = 0 \quad (3.1)
\end{aligned}$$

where i is the index of the spatial infinite sum of current contributions resulting from the image theorem. The observation and the source points are $\boldsymbol{\rho}$ and $\boldsymbol{\rho}'$, respectively, and \mathbf{g} is the free-space dyadic Green's function, which links the magnetic field to magnetic sources. Since the structure is not periodic along z , the current densities on the layers are not related by either Floquet boundary condition or glide symmetry conditions. However, we assume here that the magnetic currents on different layers are approximately related as

$$\mathbf{m}_{n+1}(\boldsymbol{\rho}; w_{n+1}) \approx \mathbf{m}_n(\boldsymbol{\rho} - \mathbf{s}_{n,n+1}; w_{n+1}) e^{-j\psi_{n,n+1}} \quad (3.2)$$

$$\mathbf{m}_{n-1}(\boldsymbol{\rho}; w_{n-1}) \approx \mathbf{m}_n(\boldsymbol{\rho} - \mathbf{s}_{n-1,n}; w_{n-1}) e^{-j\psi_{n-1,n}} \quad (3.3)$$

where $\mathbf{s}_{n,n+1} = s_{n,n+1} \hat{\mathbf{x}} + s_{n,n+1} \hat{\mathbf{y}}$ is the vector shift along x and y and $\psi_{n,n+1}$ is a phase shift describing the propagation from one layer to the next. The conditions (3.2) and (3.3) imply that the magnetic current densities on different layers have the same longitudinal distribution along the slots, shifted in space and with a phase delay, while only the transverse distribution changes because of the different gap widths w_n . This assumption allows writing (3.1) only in term of a single unknown distribution \mathbf{m}_n . Such condition is sufficient to apply the same procedure as in [29] to find the equivalent layer reactance

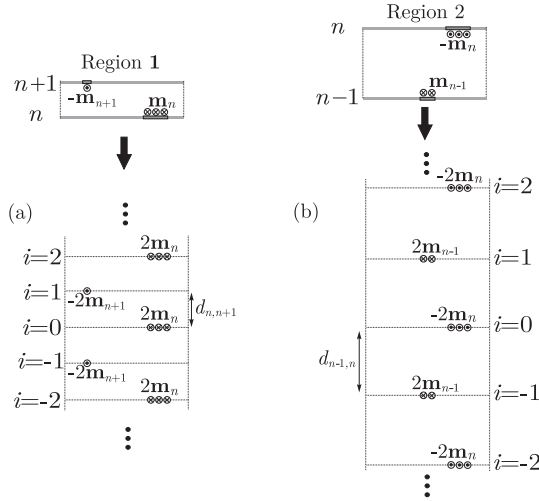


Figure 3.4: Application of image theorem for (a) Region 1 and (b) Region 2, defined in Fig. 3.3.

analytically. The method is described in detail in [24, 28] and consists of expanding the unknown magnetic current in only four entire domain basis functions, that are enough to describe the total current distribution for any generic plane-wave incidence. The basis functions have closed-form Fourier transform, thus Galerkin projection can be applied in the spectral domain, leading to a system of 4 linear equations. The properties of the chosen basis functions allow to further simplify the problem in a system of only 2 equations, leading to an analytical solution for the equivalent layer impedance.

3.2.2. Equivalent Impedance of a Layer in a Non-Periodic Sequence

By following the procedure described in the previous section, the equivalent layer impedance is derived. For the internal layers, i.e. for $n \in [2, 3, \dots, N-1]$, the layer susceptance can be written as a Floquet expansion with indexes m :

$$B_n = \frac{jp}{\zeta_0 \lambda_0} \sum_{m \neq 0} \left\{ S_m(w_n) [f_m(d_{n,n+1}) + f_m(d_{n-1,n})] + S_m(w_{n+1}) g_m(s_{n,n+1}, d_{n,n+1}) + S_m(w_{n-1}) g_m(s_{n,n-1}, d_{n,n-1}) \right\} \quad (3.4)$$

where we introduced the functions

$$S_m(w) = \frac{\left| \text{sinc}\left(\frac{\pi m w}{p}\right) \right|^2}{|m|} \quad (3.5)$$

$$f_m(d) = -\cot\left(\frac{-2j\pi|m|d}{p}\right) \quad (3.6)$$

$$g_m(s, d) = e^{j2\pi m s/p} \csc\left(\frac{-2j\pi|m|d}{p}\right). \quad (3.7)$$

In the function definition, we omitted the dependence on the period p , since it is assumed to be fixed and equal for all the layers. For the first and last layers ($n = 1$ and $n = N$), because of the absence of one of the adjacent layers, the susceptance changes as

$$B_1 = \frac{jP}{\zeta_0 \lambda_0} \sum_{m \neq 0} \{S_m(w_1)[-j + f_m(d_{1,2})] + S_m(w_2)g_m(s_{1,2}, d_{1,2})\} \quad (3.8)$$

$$B_N = \frac{jP}{\zeta_0 \lambda_0} \sum_{m \neq 0} \{S_m(w_N)[-j + f_m(d_{N-1,N})] + S_m(w_{N-1})g_m(s_{N-1,N}, d_{N-1,N})\}. \quad (3.9)$$

An equivalent transmission line circuit, similar to the one introduced in [28] and [29], can be used for the ADL with non-identical layers. The equivalent reactances of the individual layers are represented in terms of the susceptances as follows:

$$Z_{n,TM} = \frac{-j}{B_n} \quad (3.10)$$

and

$$Z_{n,TE} = \frac{-j}{B_n \left(1 - \frac{\sin^2(\theta)}{2}\right)} \quad (3.11)$$

for the TM and TE modes, respectively, where θ is the angle of incidence of an incoming plane wave.

These reactances are placed as shunt impedances along a z -oriented transmission line, which describes the propagation of a generic plane wave through the ADL. An example of a five-layer structure is shown in Fig. 3.5(a) and its TE and TM equivalent transmission line circuits in Fig. 3.5(b).

3.2.3. Validation of the Closed-Form Solutions

To validate the provided formulas, some numerical examples are considered in this section. The reflection and transmission coefficients are calculated with the analytical transmission line models and compared with CST simulations of the same structure, for TE and TM incident plane waves. All given examples assume an ADL structure consisting of five layers, with period in x - and y -direction $p = 0.0785\lambda_0$, where λ_0 is the wavelength in free space at 5 GHz. The angle of incidence of the plane wave is $\theta = 60^\circ$.

Figure 3.6 shows the S-parameters of the plane wave, when the width of the gap between the patches is varied for each layer, while all other parameters are constant. The inter-layer distance in the z -direction is $d = 0.012\lambda_0$, and no shift between the layers is present. The widths of the gaps are $w_1 = 0.01\lambda_0$, $w_2 = 0.015\lambda_0$, $w_3 = 0.02\lambda_0$, $w_4 = 0.025\lambda_0$ and $w_5 = 0.03\lambda_0$.

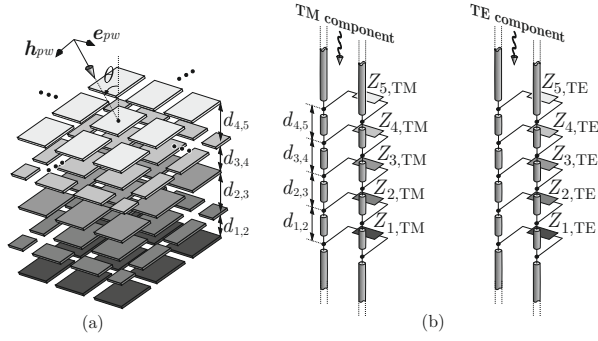


Figure 3.5: (a) Plane wave incident on a structure of five ADLs with non-identical layers; (b) Equivalent circuits for TE and TM components.

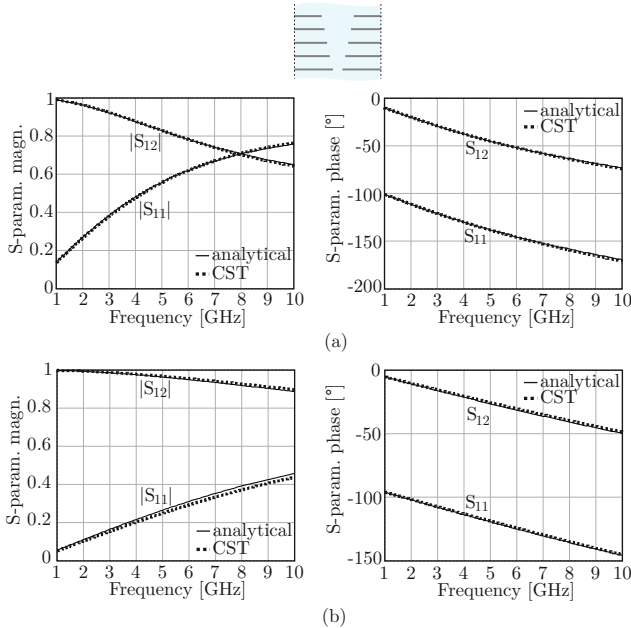


Figure 3.6: Amplitude and phase of the reflection and transmission coefficients of a plane wave incident on an ADL consisting of five layers. The value of w_n is varying between the layers: $w_1 = 0.01\lambda_0$, $w_2 = 0.015\lambda_0$, $w_3 = 0.02\lambda_0$, $w_4 = 0.025\lambda_0$ and $w_5 = 0.03\lambda_0$. The other geometrical parameters are constant: $p = 0.0785\lambda_0$, $d = 0.012\lambda_0$. No shift between the layers is present. λ_0 is the wavelength in free space at 5 GHz. The angle of incidence $\theta = 60^\circ$. (a) TE-incidence. (b) TM-incidence.

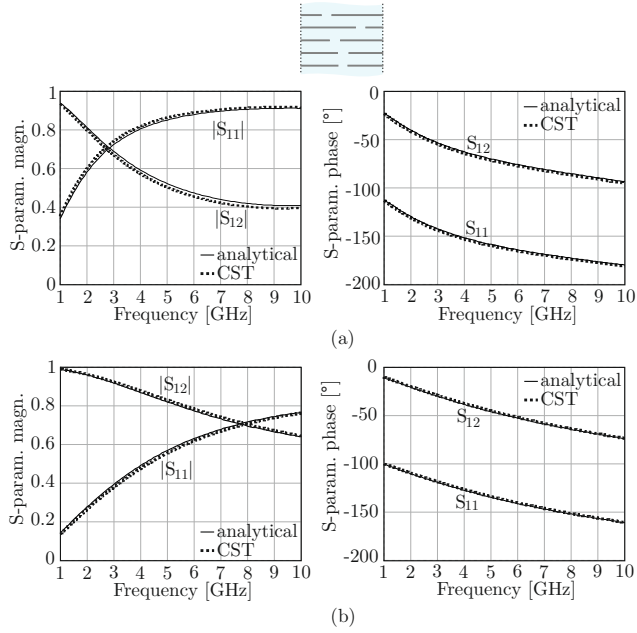


Figure 3.7: Amplitude and phase of the reflection and transmission coefficients of a plane wave incident on an ADL consisting of five layers. The shift between adjacent layers is varying throughout the structure: $s_{1,2} = 0$, $s_{2,3} = 0.1p$, $s_{3,4} = 0.3p$ and $s_{4,5} = 0.4p$. The other geometrical parameters are constant: $p = 0.0785\lambda_0$, $d = 0.012\lambda_0$ and $w = 0.01\lambda_0$. λ_0 is the wavelength in free space at 5 GHz. The angle of incidence $\theta = 60^\circ$. (a) TE-incidence. (b) TM-incidence.

Figure 3.7 shows the S-parameters for the same structure, when the width of the gaps between the patches is constant, $w = 0.01\lambda_0$, and the relative shift between adjacent layers is varying: $s_{1,2} = 0$, $s_{2,3} = 0.1p$, $s_{3,4} = 0.3p$ and $s_{4,5} = 0.4p$.

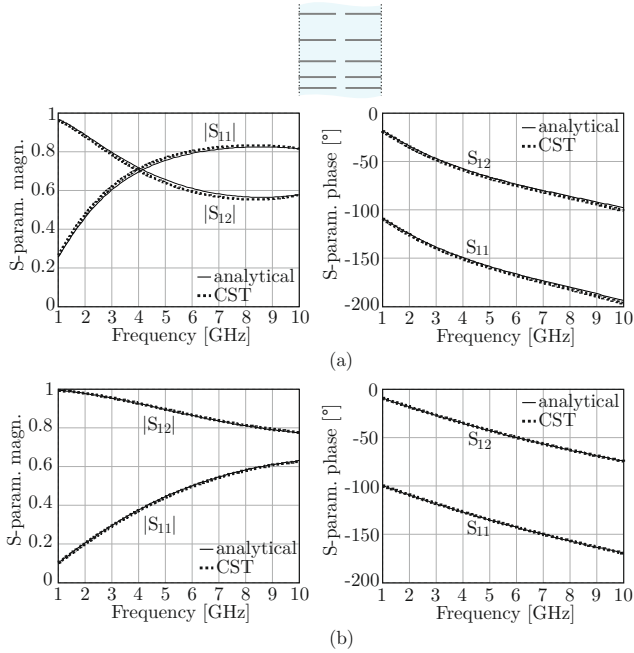


Figure 3.8: Amplitude and phase of the reflection and transmission coefficients of a plane wave incident on an ADL consisting of five layers. The distance in z -direction between adjacent layers is varying throughout the structure: $d_{1,2} = 0.01\lambda_0$, $d_{2,3} = 0.015\lambda_0$, $d_{3,4} = 0.02\lambda_0$ and $d_{4,5} = 0.025\lambda_0$. The other geometrical parameters are constant: $p = 0.0785\lambda_0$ and $w = 0.01\lambda_0$. No shift between the layers is present. λ_0 is the wavelength in free space at 5 GHz. The angle of incidence $\theta = 60^\circ$. (a) TE-incidence. (b) TM-incidence.

Figure 3.8 refers to varying values of the distance between adjacent layers: $d_{1,2} = 0.01\lambda_0$, $d_{2,3} = 0.015\lambda_0$, $d_{3,4} = 0.02\lambda_0$ and $d_{4,5} = 0.025\lambda_0$. The width of the gap between the patches is constant, $w = 0.01\lambda_0$, and no relative shift between the layers is present.

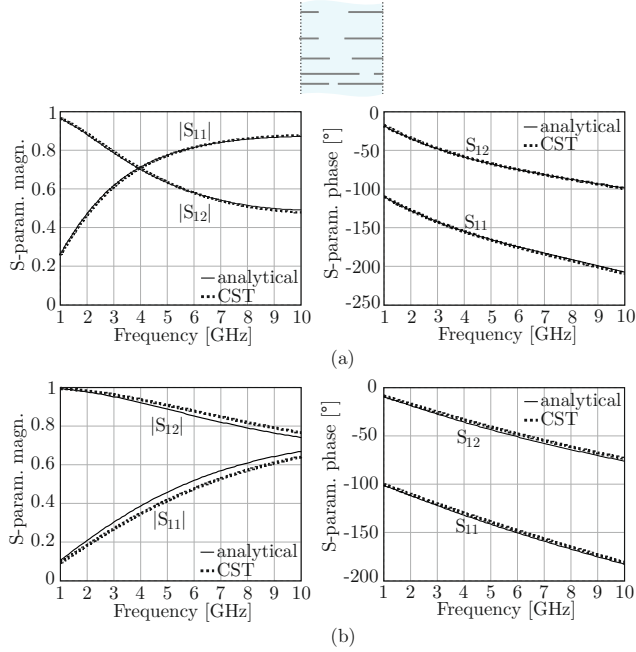


Figure 3.9: Amplitude and phase of the reflection and transmission coefficients of a plane wave incident on an ADL consisting of five layers. The period in x and y is $p = 0.0785\lambda_0$. The other geometrical parameters are changing throughout the structure: $w_1 = 0.01\lambda_0$, $w_2 = 0.015\lambda_0$, $w_3 = 0.02\lambda_0$, $w_4 = 0.025\lambda_0$ and $w_5 = 0.03\lambda_0$, $s_{1,2} = 0$, $s_{2,3} = 0.1p$, $s_{3,4} = 0.3p$ and $s_{4,5} = 0.4p$, and $d_{1,2} = 0.01\lambda_0$, $d_{2,3} = 0.015\lambda_0$, $d_{3,4} = 0.02\lambda_0$ and $d_{4,5} = 0.025\lambda_0$. λ_0 is the wavelength in free space at 5 GHz. The angle of incidence $\theta = 60^\circ$. (a) TE-incidence. (b) TM-incidence.

In the final example, the three characteristic geometrical parameters are varied all together. The widths of the gaps are $w_1 = 0.01\lambda_0$, $w_2 = 0.015\lambda_0$, $w_3 = 0.02\lambda_0$, $w_4 = 0.025\lambda_0$ and $w_5 = 0.03\lambda_0$. The distance between the layers is growing with the indexes $d_{1,2} = 0.01\lambda_0$, $d_{2,3} = 0.015\lambda_0$, $d_{3,4} = 0.02\lambda_0$ and $d_{4,5} = 0.025\lambda_0$. The relative shift between the layers is decreasing: $s_{1,2} = 0.4p$, $s_{2,3} = 0.3p$, $s_{3,4} = 0.1p$ and $s_{4,5} = 0$. The resulting reflection and transmission coefficients are shown in Fig. 3.9 for TE- and TM-incidence.

In all presented results a good agreement between the analytical formulas and CST is observed.

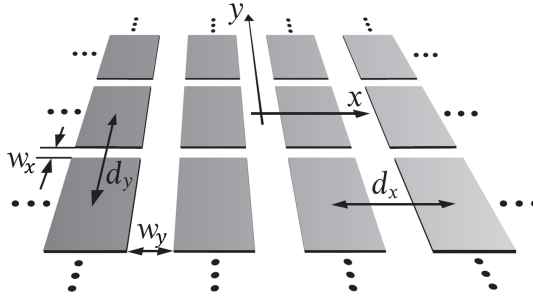


Figure 3.10: Single layer of rectangular patches with geometrical parameters.

3.3. Analysis of Non-square Artificial Dielectric Layers

3.3.1. Closed-Form Analysis of a Single Layer

The theory of artificial dielectric layers developed in earlier works [28–30] and in the first part of this chapter, always considered square patches arranged in a square periodic lattice. This assumption greatly simplifies the analysis of the scattering from the layer under generic plane-wave illumination. Indeed, for square patches small compared to the wavelength, the transverse electric (TE) and transverse magnetic (TM) modes of the plane wave are decoupled and the equivalent reactance of the layer is independent of the azimuthal plane of incidence.

In this section we generalize the theory to account for rectangular layers, as shown in Fig. 3.10, where both the period and the width of the gaps between the patches can be different along x and y . Following the same steps described in Appendix A the single layer can be represented as the following admittance matrix:

$$\mathbf{Y}_{\text{layer}} = \begin{bmatrix} jB_y \sin^2 \phi + jB_x \cos^2 \phi + Y_{\text{loop}} & j \sin \phi \cos \phi (B_y - B_x) \\ j \sin \phi \cos \phi (B_y - B_x) & jB_x \sin^2 \phi + jB_y \cos^2 \phi \end{bmatrix}. \quad (3.12)$$

The terms B_x and B_y represent the susceptance of the x - and y -oriented slots, respectively, given by

$$B_x = \frac{d_y k}{\pi \zeta} \sum_{m \neq 0} \frac{\text{sinc}^2(\pi m w_x / d_y)}{|m|} \quad (3.13)$$

$$B_y = \frac{d_x k}{\pi \zeta} \sum_{m \neq 0} \frac{\text{sinc}^2(\pi m w_y / d_x)}{|m|}. \quad (3.14)$$

where k and ζ are the phase constant and the intrinsic impedance of the medium surrounding the layer. The admittance Y_{loop} is an additional term only present for TE incidence, associated with currents loops over the patches [30], given by

$$Y_{\text{loop}} = \sin^2 \theta \left(\frac{j}{B_x} + \frac{j}{B_y} \right)^{-1}. \quad (3.15)$$

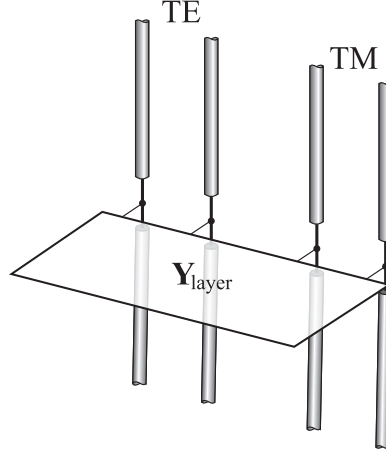


Figure 3.11: Equivalent transmission line model for a plane wave incident on a layer of periodic rectangular patches. The layer is represented as a 2-port admittance matrix $\mathbf{Y}_{\text{layer}}$.

It can be seen from (3.12) that indeed the TE and the TM transmission lines are no longer decoupled as the matrix is not diagonal. The resulting transmission line circuit for a plane wave traveling through the layer is shown in Fig. 3.11. Looking better at (3.12), the circuit representation of the non-square ADL can be drawn more explicit as in Fig. 3.12. The dependence of the azimuthal angle is represented as transformers, and the susceptances of the x - and y -oriented slots as series admittances. For square ADL (i.e. $B_x = B_y$) it can be seen that the matrix actually does simplify to a diagonal matrix, resulting in decoupled TE and TM transmission lines. This effect can be also observed from the circuit in Fig. 3.12. Under the condition $B_x = B_y$, for a purely TE incident wave, the incident current splits in the two branches of the circuit at the terminals aa' and form two equal and opposite contributions when reaching the terminals bb' . Since the total current is 0 at bb' , it is equivalent to a short circuit and thus no coupling occurs between TE and TM modes. Similarly, a purely TM incident wave would generate an equivalent short circuit at the terminal aa' and remains decoupled from the TE transmission line. Therefore, the given formulation also holds for square ADL.

3.3.2. Closed-Form Analysis of Multiple Layers

Also when multiple layers are considered, similar steps as in [30] can be followed to find the admittance matrices of the layers. In fact, the matrix for the individual layers is the same as in (3.12), but the expressions for the susceptances become

$$B_{x,\infty} = j \frac{d_y k}{\pi \zeta} \sum_{m \neq 0} \frac{\text{sinc}^2(\pi m w_x / d_y)}{|m|} \left[-\cot \left(-2j\pi |m| \frac{d_z}{d_y} \right) + e^{j2\pi m \frac{s_y}{d_y}} \csc \left(-j2\pi |m| \frac{d_z}{d_y} \right) \right] \quad (3.16)$$

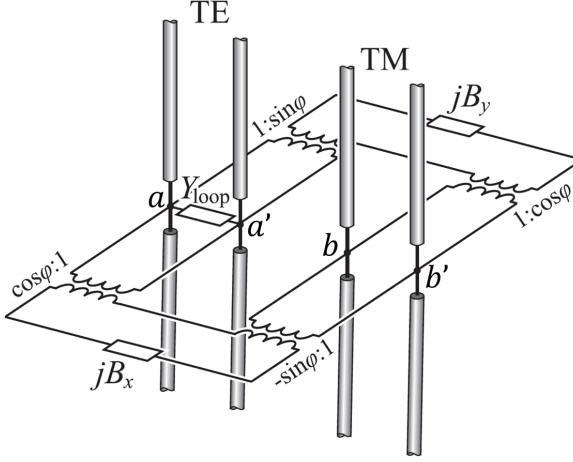


Figure 3.12: Explicit representation of the equivalent circuit representing the layer.

$$B_{y,\infty} = j \frac{d_x k}{\pi \zeta} \sum_{m \neq 0} \frac{\text{sinc}^2(\pi m w_y / d_x)}{|m|} \left[-\cot \left(-2j\pi |m| \frac{d_z}{d_x} \right) + e^{j2\pi m \frac{s_x}{d_x}} \csc \left(-j2\pi |m| \frac{d_z}{d_x} \right) \right] \quad (3.17)$$

$$B_{x,\text{semi-}\infty} = j \frac{d_y k}{\pi \zeta} \sum_{m \neq 0} \frac{\text{sinc}^2(\pi m w_x / d_y)}{|m|} \frac{1}{2} \left[-j - \cot \left(-2j\pi |m| \frac{d_z}{d_y} \right) + e^{j2\pi m \frac{s_y}{d_y}} \csc \left(-j2\pi |m| \frac{d_z}{d_y} \right) \right] \quad (3.18)$$

$$B_{y,\text{semi-}\infty} = j \frac{d_x k}{\pi \zeta} \sum_{m \neq 0} \frac{\text{sinc}^2(\pi m w_y / d_x)}{|m|} \frac{1}{2} \left[-j - \cot \left(-2j\pi |m| \frac{d_z}{d_x} \right) + e^{j2\pi m \frac{s_x}{d_x}} \csc \left(-j2\pi |m| \frac{d_z}{d_x} \right) \right] \quad (3.19)$$

where the subscript ∞ represents a layer with another layer both above and below, and semi- ∞ represents a layer either on the top or on the bottom.

To find the S-parameters of the total four-port structure considering multiple layers as shown in Fig. 3.13(a), one first splits the total transmission line structure in separate four-ports consisting of a single layer, Fig. 3.13(b). The ports are numbered as shown in the figure. The 4×4 S-parameter matrices for these layers including the pieces of transmission line can be found by terminating two ports at a time with matched impedances, i.e. $Z^{TE} = \zeta k / k_z$ and $Z^{TM} = \zeta k_y / k$, where $k_z = -j \sqrt{-(k^2 - k_x^2 - k_y^2)}$ with $k_x = k \sin(\theta) \cos(\phi)$, $k_y = k \sin(\theta) \sin(\phi)$ and θ and ϕ specify the direction of the plane wave under consideration. Once the 4×4 S-parameter matrices are found, the method described in Appendix B can be used to cascade these matrices to find the S-parameters of the two layer structure. This method can be repeated for n -layered non-square ADL stratifications.

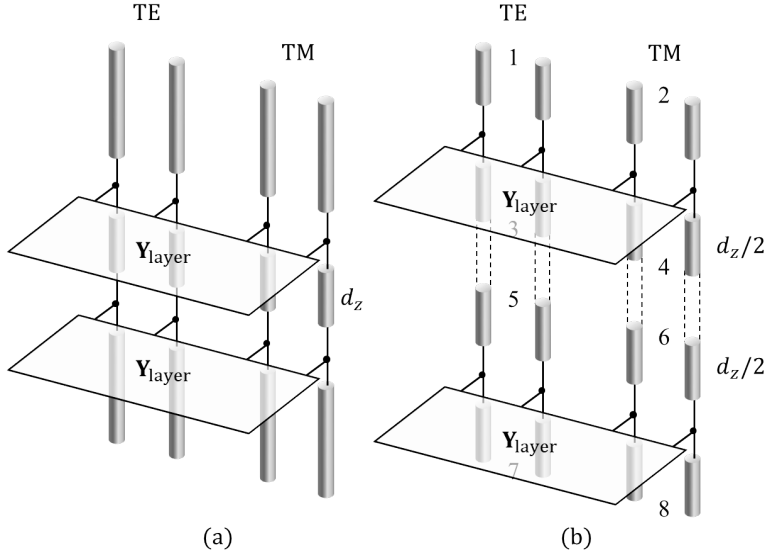


Figure 3.13: (a) Transmission line model of multiple layers non-square ADL. (b) Total four-port structure split in separate four-ports for each layer.

Figure 3.14 shows the amplitude and phase of the S-parameters of two non-square ADL structures. A comparison is shown between our analytical method and CST full wave simulation for a TE incident wave. A very good agreement can be seen between the curves for both structures, thus validating the analytical method.

3.4. Conclusion

We presented analytical formulas for the analysis of non-periodic ADLs. Closed-form expressions for the equivalent layer impedance for generic plane wave incidence were derived. The proposed formulas are more general than those presented in previous works. The individual layers may be different from each other in terms of geometrical parameters and the mutual distance and shift between adjacent layers may vary along the stratification. Results from the analytical formulas were validated by comparison with a commercial electromagnetic solver. By dropping the restriction of identical layers, the expressions can be used to design ADLs that are not uniform along the vertical dimension. Possible applications can be tapered impedance transformers to realize wideband matching slabs or wide angle impedance matching superstrates for broadband phased arrays.

Further generalizations are done on the analysis of ADLs, as structures with different geometrical parameters in x - and y -directions were studied. Closed-form expressions for the layer impedances in an equivalent transmission line model were derived, that describe these non-square ADLs. It is found that the TE and TM modes are no longer decoupled and that the coupling depends on the azimuthal angle of the incident plane wave. The method is validated by comparing S-parameters for arbitrary plane wave in-

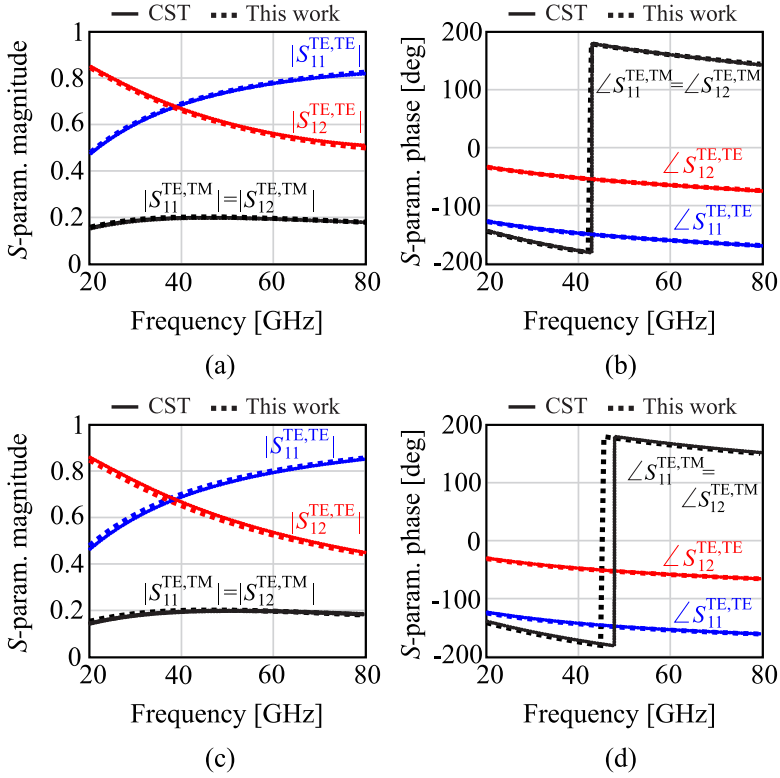


Figure 3.14: Scattering parameters of a plane wave incident from $\theta = 45^\circ$ and $\phi = 45^\circ$ on artificial dielectric layers: (a) magnitude and (b) phase of the S-parameters for 5 layers with $d_z = 0.012\lambda$, $d_x = 0.15\lambda$, $d_y = 0.2\lambda$, $w_x = 0.01\lambda$, $w_y = 0.02\lambda$, $s_x = s_y = 0$; (c) magnitude and (d) phase of the S-parameters for 2 layers with $d_z = 0.012\lambda$, $d_x = 0.15\lambda$, $d_y = 0.2\lambda$, $w_x = 0.01\lambda$, $w_y = 0.02\lambda$, $s_x = 0.2d_x$ and $s_y = 0.2d_y$. λ is the free space wavelength at 80 GHz.

cidence with full wave simulations.

Chapter 4

Efficient Waveguide Power Combiners at mm-Wave Frequencies

In this chapter, an efficient power combiner for mm-wave frequency transmitters is investigated. The combiner is based on a parallel plate waveguide (PPW) excited with multiple parallel feeds. The Doherty power combiner scheme can be also integrated in the proposed concept, to increase the efficiency of the amplifiers when implementing amplitude modulation. The advantage of the proposed PPW combiner with respect to other concepts, e.g. the ones based on substrate integrated waveguide (SIW), is the wider bandwidth and the scalability to an arbitrary number of inputs. Measured results from a demonstrator realized in standard printed circuit board (PCB) technology are presented. Two variations of the combiner are implemented, one terminated with a 50Ω coaxial output, and another integrated with an antenna. In the latter case, the waveguide is folded so that both the power combiner and the antenna fit within a half wavelength size, and thus would be compatible with a dense array implementation.

4.1. Parallel Plate Waveguide Combiner

4.1.1. Single-Feed and Multi-Feed PPW

We consider a PPW as shown in Fig. 4.1(a). For the transverse electromagnetic (TEM) mode, neglecting fringing fields, the characteristic impedance is given by

$$Z_{\text{PPW}} = \zeta \frac{h}{w} \quad (4.1)$$

where ζ is the intrinsic impedance of the material inside the PPW, h is the height of the PPW and w is its width. If a delta-gap source is exciting the PPW of semi-infinite length, the input impedance of the source is approximately equal to Z_{PPW} .

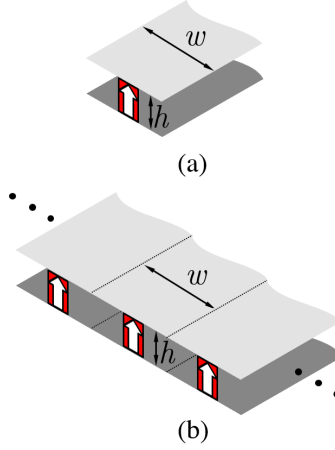


Figure 4.1: (a) Single PPW fed with a lumped port depicted as a red rectangle and (b) multiple connected PPWs in parallel.

If one considers a periodic version of the same geometry (Fig. 4.1(b)), where an infinite array of PPW fed by delta-gap sources are connected in the transverse dimension, the active input impedance of each source is also approximately equal to $Z_{\text{act}} = \zeta h/w$, where w now refers to the transverse period. Therefore, assuming that no power leaks from the sides of the PPW, i.e. the height h is much smaller than the wavelength, the input impedances in both configurations shown in Fig. 4.1 are the same and frequency independent.

4.1.2. Comparison between SIW and PPW Combiners

To emphasize the non-dispersive properties of PPW combiner, Fig. 4.2 shows a comparison between the active input impedances of a 12-feed power combiner implemented in a substrate integrated waveguide (SIW) and in a PPW, over the frequency range of interest. The propagation in the waveguide is along x , while the feeds are arrayed along the y -direction. The height of the structure is $h = 101\mu\text{m}$ and the width of the sections is $w = 400\mu\text{m}$, also equal to the center-to-center distance between feeds. The waveguides are filled with a dielectric with relative permittivity $\epsilon_r = 3.66$, such that the characteristic impedance from (4.1) is $Z_{\text{PPW}} = 50\Omega$. The normalization impedance of the ports are all set to $Z_{\text{port}} = 50\Omega$ and the feed are all exited with equal amplitude and phase. Due to the symmetric nature of the structures, only the impedance of 6 ports are shown. It is clear from Fig. 4.2 that the active input impedance seen from the different ports inside the SIW is not only frequency dependent, but also largely varying from port to port. Moreover, the ports close to the metal side walls show very low input resistance, which can result in poor matching. It can be expected that, in the SIW case, providing different weights to the feeds according to the sinusoidal distribution of the fundamental TE_{10} mode would improve the variability of the input impedance among different ports. However, this would require a specific adjustment of the amplitudes from each PA that depends on the number of inputs, and the PAs cannot all operate simultaneously at equal and maximum

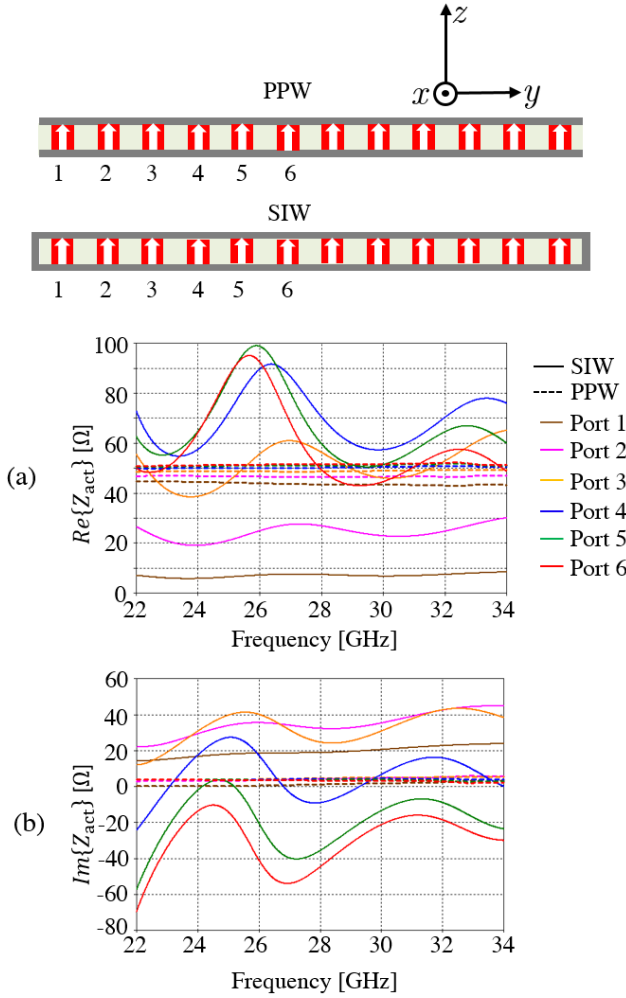


Figure 4.2: Comparison of active (a) input resistance and (b) input reactance seen from 12 ports feeding a PPW (dashed) and a SIW (solid). Because of symmetry, only the impedances of 6 feeds are shown.

power.

On the contrary, the active impedances for the PPW in Fig. 4.2 are nearly constant with frequency and show very little variation between the different ports, when fed with equal amplitudes. This allows to add more feeds in parallel without the need of re-optimizing the structure, unlike the SIW case.

4.2. PPW Implementation of a Doherty Combiner

In this section we propose a concept that combines the PPW parallel combiner with the Doherty scheme. The Doherty combiner [15] provides a matching network, which aims

at maximizing the efficiency of the PAs over a range of output power.

4.2.1. Ideal Two-way Series Doherty Circuit

A circuit model of the structure under analysis is shown Fig. 4.3(a), which represents a two-way series Doherty combiner [17]. This consists of two PAs, one referred as ‘main’ and the other as ‘peaking’, connected by a quarter-wave transmission line with characteristic impedance Z_0 . The output load is indicated as Z_l and can represent, for instance, a waveguide or a radiating structure. The two PAs are assumed to be identical and can be represented as equivalent, voltage controlled, Norton current sources, as described in Appendix A. By tuning the control signal v_{in} , both the current and the impedance of the Norton sources vary, to provide a desired level input power.

To implement the Doherty scheme, the values of the equivalent generator currents for the main and peaking PAs, I_m and I_p , depend on v_{in} as follows:

$$I_m(v_{in}) = v_{in}/Z_{norm} \quad (4.2)$$

$$I_p(v_{in}) = \begin{cases} j(2v_{in} - 1)/Z_{norm} & v_{in} \geq 0.5 \\ 0 & \text{otherwise} \end{cases} \quad (4.3)$$

where Z_{norm} is a frequency-dependent normalization impedance, which depends on the maximum value of v_{in} that satisfies the condition (C.4). The generator currents are plotted in Fig. 4.3(b) as a function of v_{in} . Following the steps as described in [70], it is found that the characteristic impedance of the quarter-wave section must satisfy the condition $Z_0 = Z_l/2$.

The normalized input impedance, as seen from the main PA and the peaking PA, of an ideal combiner as a function of v_{in} , is shown in Fig. 4.3(c). It can be seen that the input impedance of the main PA is constant $Z_{in,m} = Z_l$ until $v_{in} = 0.5$ (referred to as power back-off), after which it decreases to half its original value $Z_{in,m} = Z_l/2$. The input impedance of the peaking PA starts from infinity at power back-off and drops to $Z_{in,p} = Z_l/2$ for $v_{in} = 1$ (full power).

4.2.2. PPW Implementation

A PPW implementation of the two-way Doherty combiner is shown in Fig. 4.4(a). The PPW consists of two sections, one quarter-wave long between the main PA and the peaking PA, with height h_1 , and another representing the output waveguide, with height h_2 and characteristic impedance equal to Z_l . The heights of the two sections are related by $h_1 = h_2/2$, so that the characteristic impedance of the quarter wave section is $Z_0 = Z_l/2$, from (4.1). The PAs are represented as delta-gap sources located in slots etched on the top metal plate of the PPW.

Similar to the structure described in Sec. 4.1, multiple feeds can be placed in each slot as in Fig. 4.4(b), without significantly altering the input impedances seen by the feeds. This allows for easy scalability of the number of feeds in each slot, depending on the required output power, without the need of re-optimizing the structure. The width of the PPW increases with number of parallel feeds N and the characteristic impedance of the entire PPW decreases accordingly as Z_l/N , but can be tapered to a higher impedance and be connected, for instance, to a radiating structure.

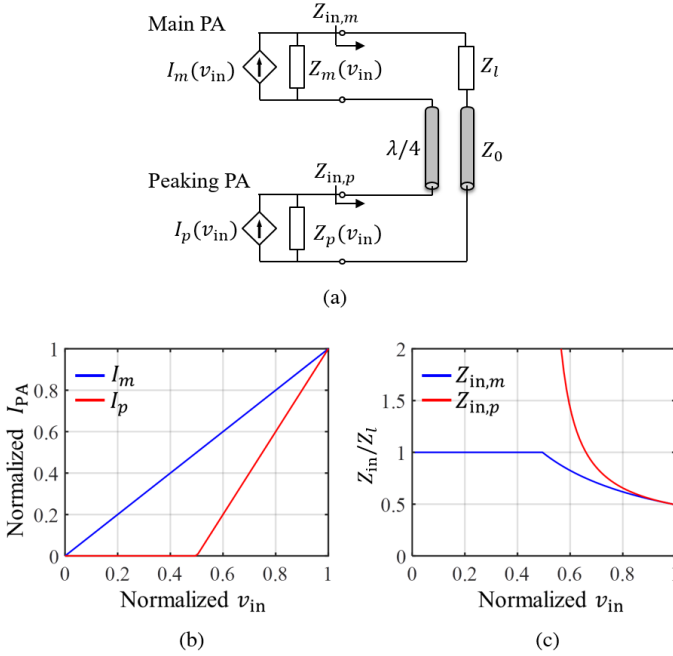


Figure 4.3: (a) Circuit representation of a two-way series Doherty combiner, (b) normalized generator current and (c) input impedance of an ideal combiner as seen from the main PA and the peaking PA as a function of v_{in} .

As an example, the PPW Doherty combiner with three main and three peaking PAs is considered. The PPW is filled with a material with $\epsilon_r = 3.66$. The width of the three PPW sections is $w = 750\mu\text{m}$, $h_1 = 101\mu\text{m}$ and $h_2 = 202\mu\text{m}$. From (4.1), the characteristic impedances of the two waveguide sections are $Z_0 = 25\Omega$ and $Z_l = 50\Omega$.

4.2.3. Simulated Results for Impedance and Efficiency

The structure is simulated in CST and the S-parameters are combined in post-processing to calculate the active impedances and the efficiency. The inputs representing the main PAs are numbered 1, 2 and 3, while the peaking PAs are numbered 4, 5 and 6. Figure 4.5(a) shows the active impedances seen from the main PAs at power back-off, for which ports 1, 2 and 3 are active, while ports 4, 5 and 6 are switched off. The passive ports are assumed to be terminated on a load $Z_p = 480\Omega$, which represents the parasitics of the PA when it is inactive, as described in Appendix A. The figure also shows the generator impedance Z_m , as a function of frequency. It can be seen that the value of the generator impedance Z_m differs from the ideal value of 50Ω and varies as a function of the frequency, to satisfy the condition (C.4). The stepped nature of the generator impedance curve is due to the assumption that the PA is composed of a finite number of sub-PAs, that are either on or off (see Appendix A), resulting in a quantized characteristic.

Similarly, the active input impedances and the generator impedances at full power, when all 6 ports are active, are shown in Fig. 4.5(b). In this case, the input impedances

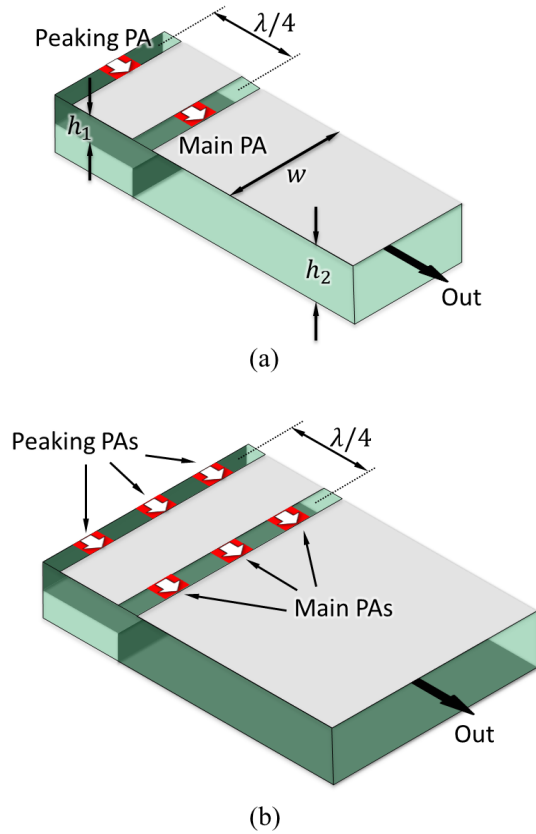


Figure 4.4: PPW implementation of a Doherty power combiner, for (a) a single main and peaking PA and (b) multiple main and peaking PAs in parallel.

and the generator impedances are seen to be approximately equal to half of their values for the power back-off case, as expected.

The efficiency of the combiner is found as the ratio between the output power, P_{out} , and the supply power P_{supply} . Figure 4.6(a) shows the efficiency of the combiner at 28 GHz as a function of the normalized input voltage v_{in} . The characteristic efficiency curve of a Doherty combiner can be observed, with peaks both at power back-off and at full power. The efficiency as a function of frequency is presented in Fig. 4.6(b). Three curves are shown: the efficiency at power back-off, the efficiency at full power and the average efficiency between these two points. It can be seen that, over the entire frequency range of interest, all three curves are higher than 60%. Note that the maximum theoretical efficiency is 79% from (C.3).

4.3. PCB Demonstrator

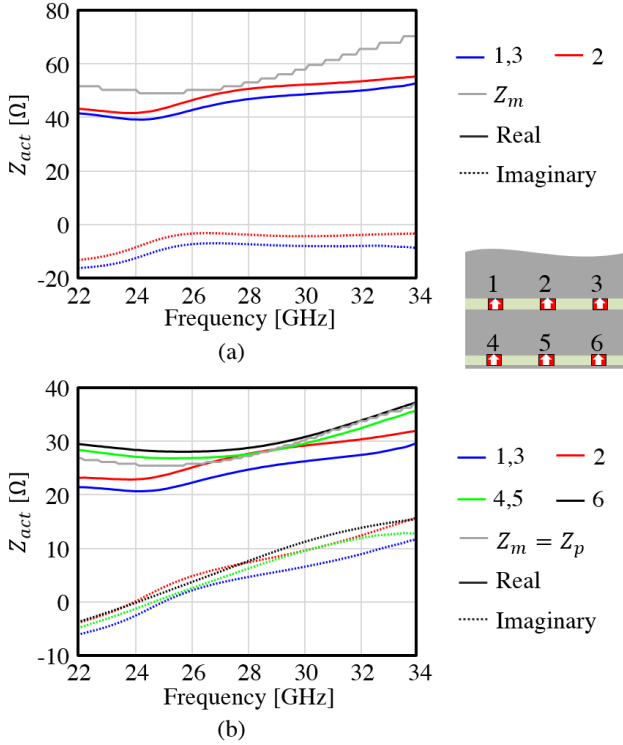


Figure 4.5: Active impedance seen from the six PAs in the PPW Doherty combiner (a) at power back-off and (b) at full power.

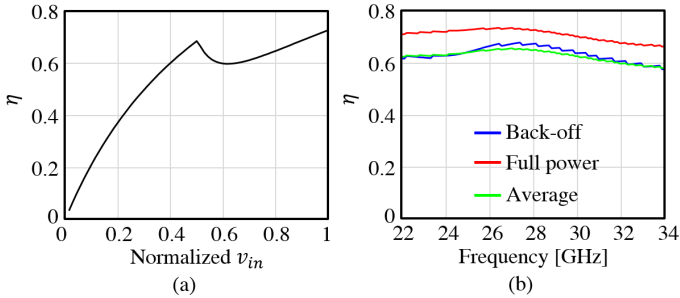


Figure 4.6: Efficiency of the PPW Doherty combiner (a) for increasing v_{in} at 28 GHz and (b) as a function of frequency. The efficiency is shown at power back-off, at full power and the average efficiency between back-off and full power.

4.3.1. PCB Design of the Combiner

To validate the concept described in the previous section, a demonstrator is fabricated in standard PCB technology. A 6-to-1 PPW Doherty combiner is designed, where the transition from the PPW with characteristic impedance $Z_l = 50/3 \approx 17\Omega$ to a 50Ω microstrip

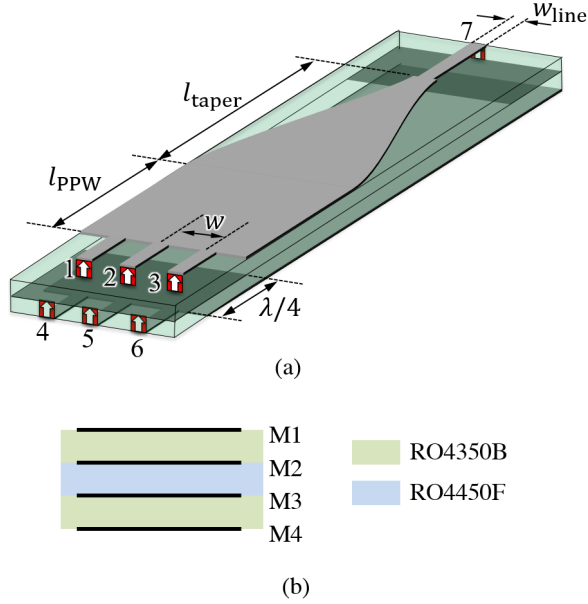


Figure 4.7: (a) Design of the 6-to-1 PPW Doherty combiner with a tapered impedance transformer from the PPW to the output microstrip; (b) schematic sideview of the PCB stack-up.

output is realized using a tapered impedance transformer of length l_{taper} , as shown in Fig. 4.7(a). A section with length l_{PPW} of straight PPW separates the feeding slots from the taper, to ensure that the desired TEM mode is formed before entering the PPW taper. Comparing Fig. 4.7(a) with Fig. 4.4(b), it can be seen that the feeding slots have been placed on the side of the PPW with the electric field oriented vertically. This allows for the feeding lines to be in the same metal layers as the top and bottom plates of the PPW, making the routing of the feeding microstrip lines more convenient. Figure 4.7(b) shows the schematic side view of the PCB stack-up. Four metal layers are considered, printed on Rogers RO4350B dielectric slabs ($\epsilon_r = 3.66$, $\tan \delta = 0.0037$ at 10 GHz) with a height of $101 \mu\text{m}$. The two slabs are then bonded together using Rogers RO4450F bond-ply ($\epsilon_r = 3.52$, $\tan \delta = 0.004$ at 10 GHz), of the same height.

The geometrical parameters of the design are: $h_1 = 101 \mu\text{m}$, $h_2 = 202 \mu\text{m}$, $w = 750 \mu\text{m}$, $l_{PPW} = 1.4 \text{mm}$ and $l_{taper} = 5.6 \text{mm}$. The resulting active impedances of the inputs are in the order of 50Ω and 25Ω at power back-off and full power, respectively. The width of the microstrip feeding lines is $w_{line} = 200 \mu\text{m}$, so that their characteristic impedance is 50Ω . The lines extend a few centimeters to reach top mounted 50Ω Rosenberger 02K722-40MS3 solderless connectors. Figure 4.8 shows the fabricated demonstrator. It can be seen from Fig. 4.8(a) that Tru-Reflect-Line (TRL) calibration lines are also present on the board, to de-embed the effect of the connectors and the different feeding lines, placing the reference plane of the measurements at the location where the microstrips feed the PPW. A thick slab of FR4 is added to the board as support structure to provide rigidity.

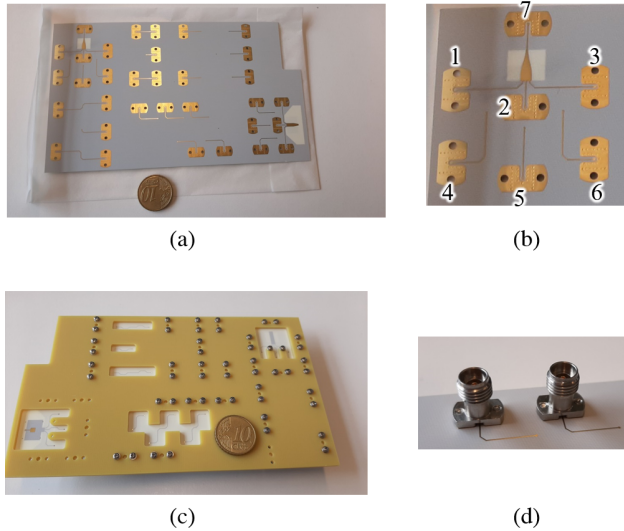


Figure 4.8: Photographs of the fabricated demonstrator: (a) entire board with demonstrator and TRL-calibration lines, (b) zoom of the 6-to-1 PPW Doherty combiner with port numbering; (c) back view of the assembled demonstrator board; (d) top mounted coaxial connectors.

4.3.2. Measured S-Parameters and De-Embedding of Feed Lines

All the 7-port S-parameters have been measured, with the passive ports terminated on 50Ω loads. Also the error boxes of the feeding lines have been characterized by measuring the TRL structures. When de-embedding the error boxes, the results in Fig. 4.9 are obtained for the passive reflection coefficients at the input ports. It can be seen that the measured curves oscillate around the simulated ones for most cases.

Nevertheless, a problem with port 5 is observed, i.e. the measured curve in Fig. 4.9(d) shows a clear resonance around 29 GHz that is not present in the simulation. To investigate the causes of this discrepancy, we apply the inverse Fourier transform of the S-parameters S_{ii} for $i = (4, 5, 6)$ and plot the time-domain signals associated with the ports 4, 5 and 6 in Fig. 4.10(a), as a function of the distance from the cable tip. From this analysis it can be observed that ports 4 and 6 only exhibit a main reflection at the end of the feeding line, as expected. On the contrary, S_{55} shows an additional unexpected reflection at a distance indicated by X , which corresponds to the region where the line of port 5 (line 5) runs underneath the connector of port 2 (see Fig. 4.10(b)). In this region several plating through hole vias are present, which causes a sinking effect of the microstrip line locally around the vias, as shown in Fig. 4.11. The prepreg tends to fill the via holes, so that the microstrip line locally drops closer to the ground plane, yielding a variation of the characteristic impedance.

This phenomenon occurs in the device under test, but not in TRL structure, where the vias are not present. To confirm the given explanation, we simulated the structure with a microstrip line locally sunk by $60\mu\text{m}$ and the simulated results reproduce better the measured ones, as shown in Fig. 4.12, for both the total structure and after de-embedding. In the remainder of the section, we then consider the simulated line 5 for the

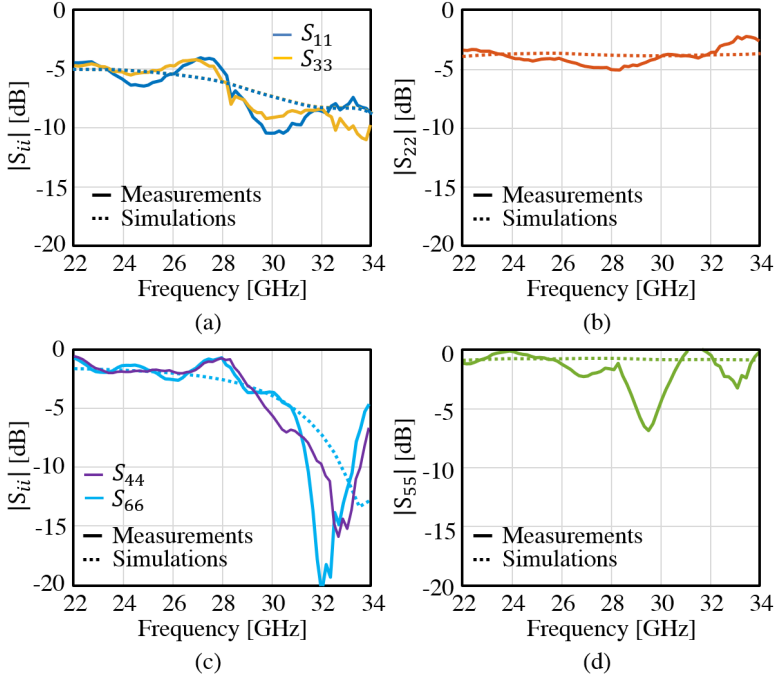


Figure 4.9: Comparison between simulated and measured reflection coefficients after de-embedding. (a) S_{11} and S_{33} . (b) S_{22} . (c) S_{44} and S_{66} . (d) S_{55} .

de-embedding of the error box, instead of the TRL measurements. While this approach improves the quality of the results for the device under test, the hybrid de-embedding procedure causes some residual inaccuracy in calibrating out the error boxes.

4.3.3. Impedance and Efficiency Results

The reflection coefficients in Fig. 4.9 are very high, because they refer to passive parameters. Instead, the structure is designed to be matched in terms of active reflection coefficients, i.e. when all ports are simultaneously excited.

In this section, the input ports are combined by a post-processing procedure, according to the Doherty combining scheme [15]. Figures 4.13(a) and (b) show the active impedance of the different ports as a function of the frequency at back-off and at full power, respectively. It can be seen that the active impedances of ports 1, 2 and 3 at back-off are oscillate around 50Ω , while at full power the active impedances fluctuate around 25Ω . The effect of the oscillations of the impedances compared to the ideal values can be quantified by investigating the PA efficiency as a function of frequency in Fig. 4.13(c). Three curves are shown: the PA efficiency at back-off, at full power and the average value between these two points. The measured efficiency is slightly lower than the simulated one, mainly due to residual mismatch of the error boxes. However, within the frequency band from 24 to 32 GHz all three curves of the PA efficiency are higher than 50% and oscillating around 60%, confirming the wideband characteristic of the combiner.

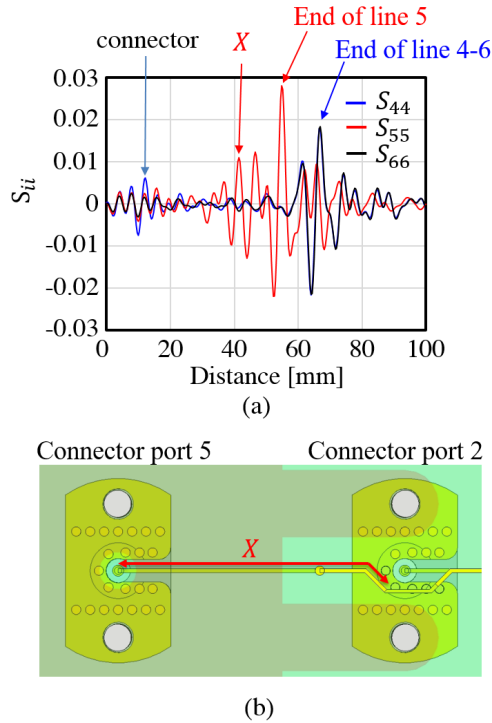


Figure 4.10: (a) Time domain analysis for S_{44} , S_{55} and S_{66} . Several expected reflections are indicated, as well as an unexpeted reflection. (b) Routing of line 5 to go underneath the vias of connector 2. Indicated distance plus the connector corresponds to X from (a).

The efficiency due to Ohmic losses and radiation of the structure can be estimated as

$$\eta_{\text{loss}} = \sum_{i=1}^7 |S_{i,7}|^2. \quad (4.4)$$

A comparison between the simulated and measured efficiency η_{loss} is shown in Fig. 4.14(a). The measured efficiency oscillates around the simulated value. Again, these fluctuations are consistent with the non-ideality of the TRL calibration. The efficiency shows values higher than 1 which is unphysical. This is due to an overestimation of the losses in the TRL structures. Figure 4.14(b) presents the insertion losses of the combiner both at back-off and at full power. It can be noted that the insertion losses for the two excitation cases are approximately equal, thus they do not increase when doubling the number of feeds from three to six.

4.4. Integration with Antenna

This section describes the integration of the PPW doherthy combiner with an antenna. A PCB demonstrator is fabricated and measurements are presented.

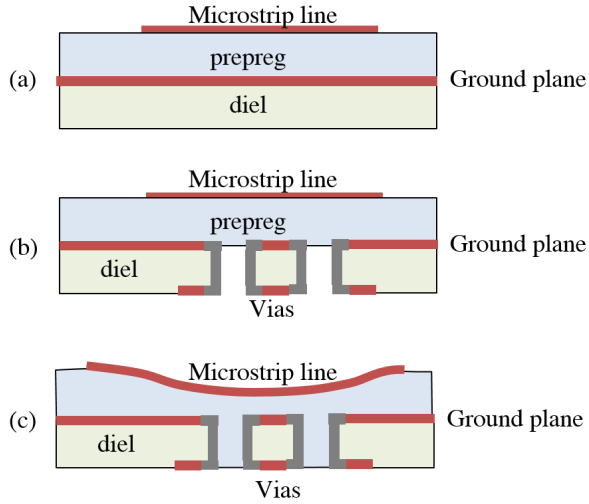


Figure 4.11: Effect of routing a microstrip line over vias in the ground plane: (a) microstrip line as designed; (b) metal plated vias are introduced beneath the line; (c) during the bonding process the melted prepreg thins down by filling the via holes, changing the characteristic impedance of the line.

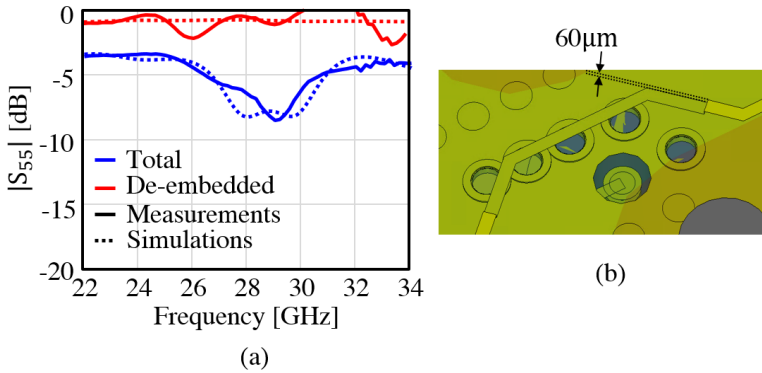


Figure 4.12: (a) Comparison between measured and simulated S_{55} with error boxes included and after de-embedding, where the error box of line 5 is simulated considering (b) a sunk region of the microstrip around the vias.

4.4.1. Design of the PPW Combiner with Antenna

An advantage of the proposed combiner is the convenient integration with a radiating element. In Sec. 4.3 the PPW was ended in a 50Ω microstrip output. In this section, the combiner is directly connected to an antenna. A conceptual drawing of the combiner-antenna co-design is shown in Fig. 4.15(a). A chip with the PAs can be connected in a flipped chip configuration to the PCB, so that the PAs excite the PPW. The waveguide has a tapered bottom plate, similar to the previous design, is folded over its top plate through a via and is connected to a patch antenna. The top plate of the waveguide now also serves as a backing reflector for the patch antenna. A matching layer is added above the patch

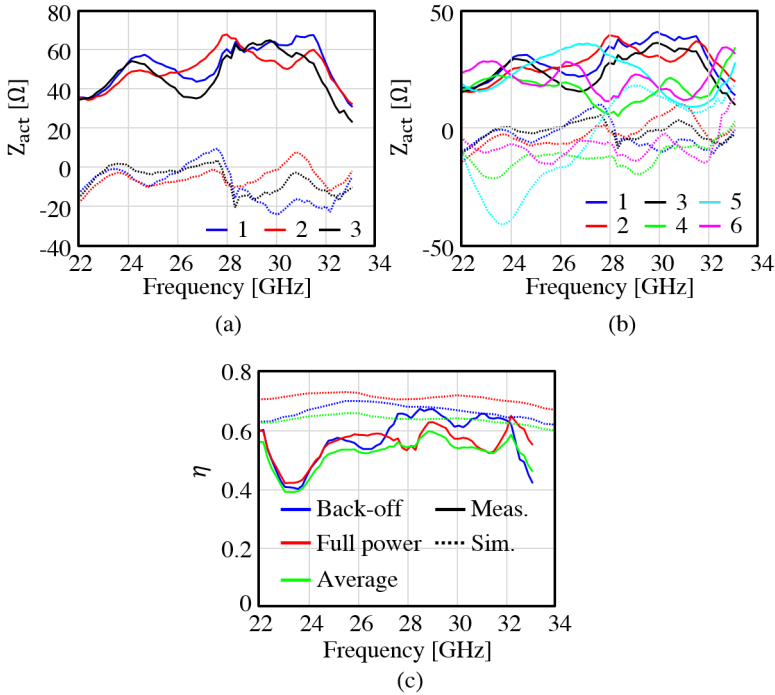


Figure 4.13: Active impedance seen from the PAs (a) at back-off and (b) at full power; (c) comparison between PA efficiency at back-off, full power and the average value, calculated from the simulated and measured structure.

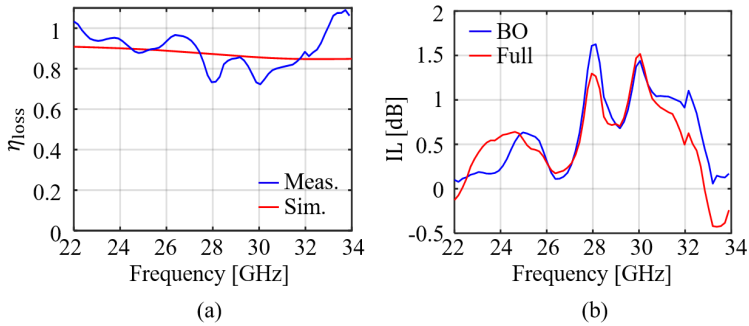


Figure 4.14: (a) Comparison between simulated and measured losses in the tapered 6-to-1 combiner. (b) Measured insertion losses of the combiner at back-off and at full power.

as superstrate, realized using artificial dielectric layers (ADLs) [28, 29]. By folding the waveguide, the total size of the structure can be reduced to fit within a half wavelength unit cell making it suitable to be implemented in a phased array.

In this chapter, we demonstrate the combiner-to-antenna transition, while the inte-

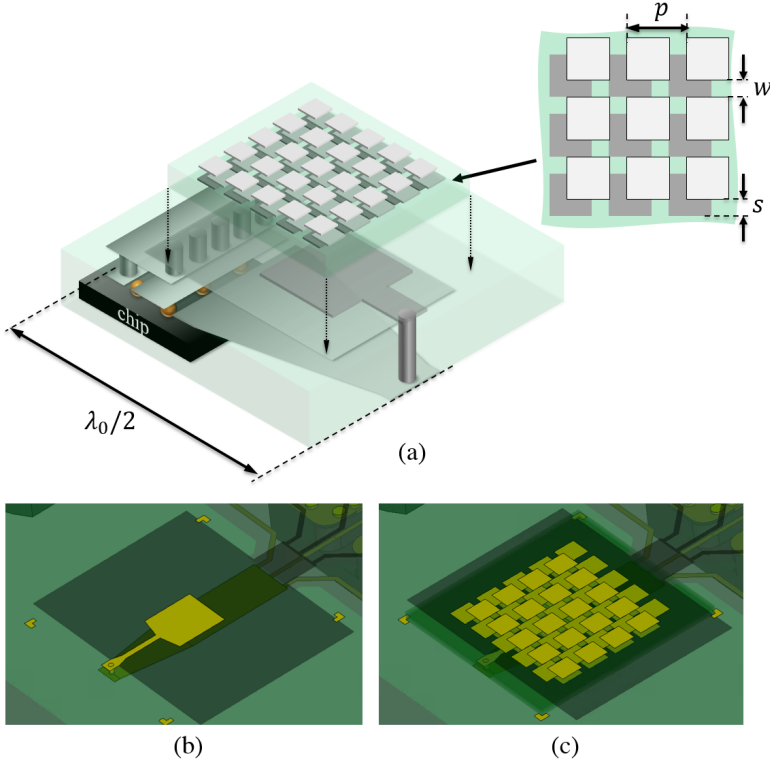


Figure 4.15: (a) Concept of combiner integrated with antenna within a half wavelength unit cell, with artificial dielectric layers added for impedance matching; (b) designed 6-to-1 combiner with antenna and (c) same structure with artificial dielectric superstrate.

gration with the chip will be the scope of the next chapter. The 6-to-1 combiner with the antenna are designed with the same layer stack-up as the combiner alone. The PPW Doherty combiner until the taper is identical to the design depicted in Fig. 4.7. The plate on M1 is tapered to a smaller width and is connected through a via to M4, where the patch antenna is printed (see Fig. 4.15(b)). The total size of the patch antenna is $2.1 \times 2.1 \text{ mm}^2$, to resonate around 28 GHz. Because of the very close proximity of the patch antenna to the backing reflector, a three layer ADL superstrate is added as a matching layer [69]. The ADL superstrate enhances the front-to-back ratio of the antenna, therefore improving the impedance matching. The ADLs are also fabricated in the same layer stack-up, cut out and glued to the board on top of the antenna (see Fig. 4.15(c)). The dimensions of the ADL, as depicted in the inset of Fig. 4.15(a), are: $p = 1.2 \text{ mm}$, $w = 0.3 \text{ mm}$ and $s = 0.35p$, so that the effective relative permittivity of the ADL for normal incidence is $\epsilon_r = 70$. The patch antenna is matched to 25Ω , allowing for a shorter tapered section transforming from 17Ω to 25Ω , rather than to 50Ω as for the combiner with coaxial output.

The 6-to-1 combiner with antenna is simulated in CST and the active S-parameters

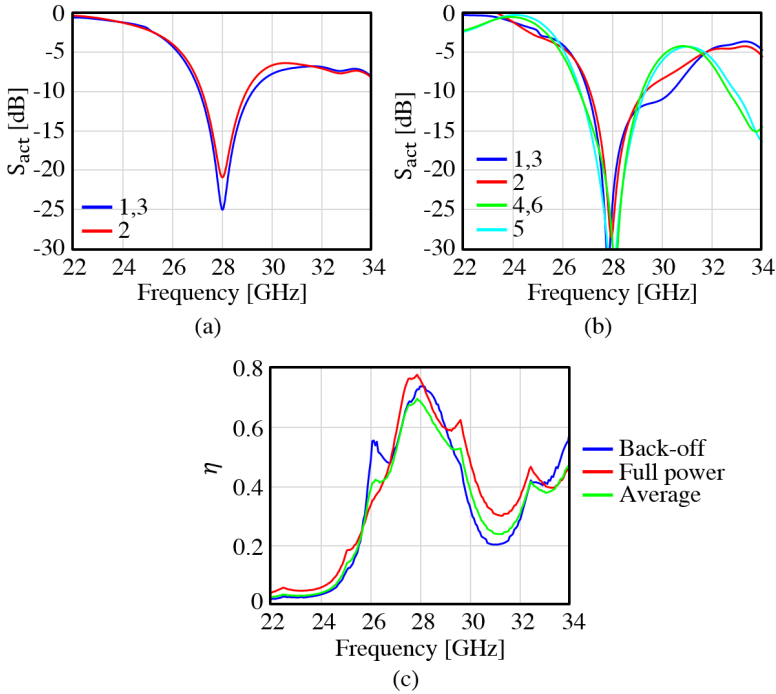


Figure 4.16: Active S-parameters of the combiner with antenna and ADL superstrate. (a) Back-off. (b) Full power. (c) Operating efficiency of the PAs, calculated as described in Sec. 4.2

are considered both at back-off ($Z_m = 50\Omega$, $Z_p = 480\Omega$) and at full power ($Z_m = Z_p = 25\Omega$). The resulting S-parameters are shown in Figs. 4.16(a) and (b). It can be seen that the total structure is well matched ($S_{act} < -10$ dB) over about a 2 GHz bandwidth centered at 28 GHz. Although wider bandwidth could be achieved by increasing the distance between the patch antenna and the backing reflector, the scope of this prototype is to demonstrate the combiner-antenna transition more than to maximize the bandwidth.

Figure 4.16(c) shows the simulated operating efficiency at back-off, full power and the average efficiency between these two points for the combiner integrated with the antenna. It can be seen that all three curves are higher than 0.5 within the impedance matching band of the antenna.

4.4.2. Measured S-Parameters

The fabricated demonstrator of the 6-to-1 combiner with antenna is shown in Fig. 4.17. The feeding network is identical to one used for the combiner without antenna in Sec. 4.3. Figure 4.18 shows the comparison between several measured and simulated S-parameters of the total structure, including the feeding lines and the connectors. It can be seen that most measured curves follow a similar trend as the simulated ones. Similar comparison was observed for ports 4, 5, and 6, not shown here for the sake of brevity. It can be seen that, while all the simulated values are slightly higher than the measured

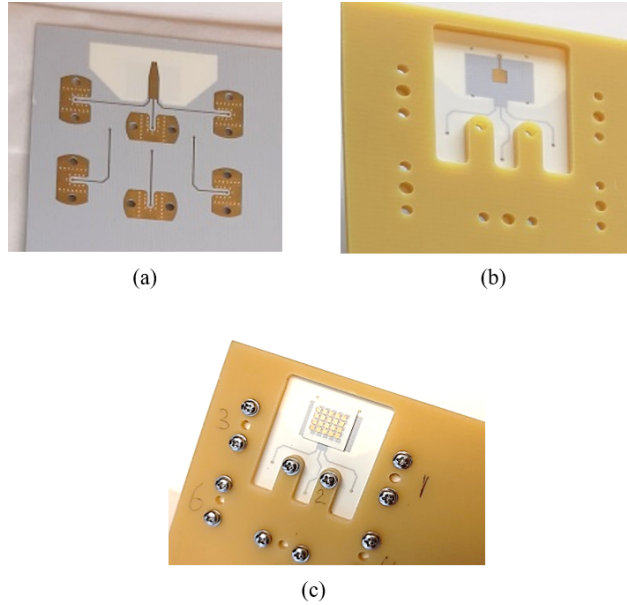


Figure 4.17: Fabricated 6-to-1 combiner with antenna. (a) Back. (b) Front without connectors and ADL. (c) Front with connectors and ADL attached.

ones, S_{22} shows a different behavior, as well as an unexpected dip at 33 GHz. This discrepancy is also visible in the phases of the S-parameters, as shown in Fig. 4.19. A good agreement can be seen for most curves, however there is a phase difference between the simulated and measured values for the S-parameters involving port 2.

By applying an inverse Fourier transform on the spectrum of the S-parameters, a time-domain analysis is performed. Figure 4.20 shows the time-domain reflection coefficient of ports 1, 2 and 3 for the combiner without antenna (Sec. IV) and with antenna. In both figures, clear reflections can be seen at the end of the feeding lines, as expected. However, it can be seen that an extra reflection occurs for port 2, at a distance that corresponds to the connector. This problem appears to be due to a local compression of the PCB after screwing the solderless connectors multiple times.

4.4.3. Radiation Characteristics

The measured radiation pattern of the antenna is presented in Figs. 4.21(a) and (b), compared with simulations, for both E - and H -plane at 28 GHz. Both co- and cross polarization show a good comparison. Higher differences are observed at very wide angles, especially in the H -plane. These are due to the absorbers placed beside the antenna to shield the edges of the support structure, as schematically shown in Fig. 4.21(c).

Figure 4.22 shows a comparison between gain and directivity of the structure when port 1 is excited. Measured results are compared with simulation from CST Studio Suite. The measured value for the directivity is calculated by estimating the radiated power from a linear interpolation between the two principal planes. For the simulated gain, a

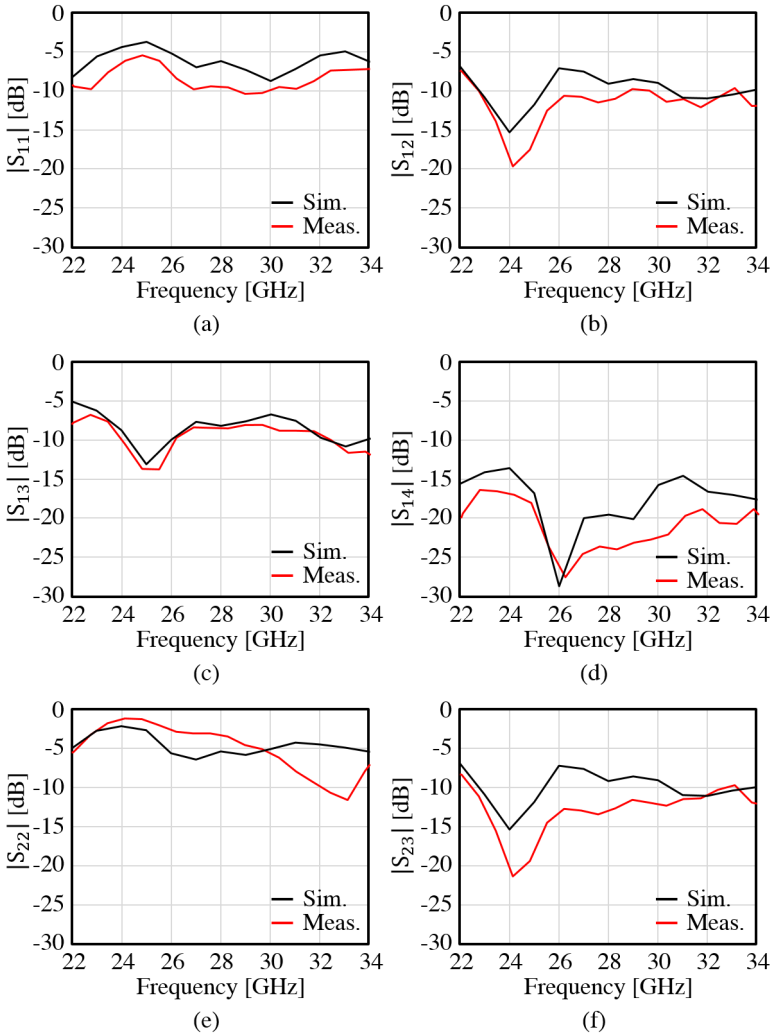


Figure 4.18: Comparison between simulated and measured amplitude of (a) S_{11} , (b) S_{12} , (c) S_{13} , (d) S_{14} , (e) S_{22} , (f) S_{23} .

range is presented between an upper bound, corresponding to surface roughness equal to $0.4 \mu\text{m}$, and a lower bound referring to a root mean square roughness of $2.8 \mu\text{m}$, as specified in [78]. The measured gain is observed to mostly fall within this range.

It is important to note that, in the region of maximum gain around 27 GHz, the difference between directivity and gain is approximately 5 dB in both simulations and measurements. This value includes the effect of the feeding lines. Simulations of the structure without the feeding lines shows that about 1 dB total losses are associated with the power combiner and the antenna.

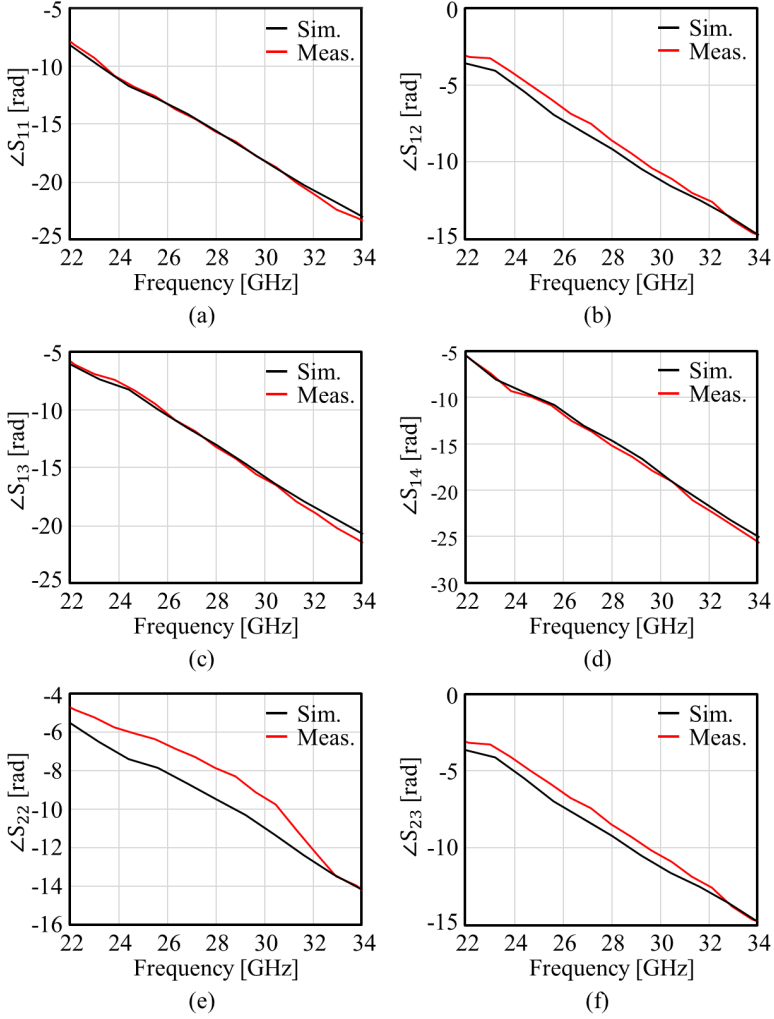


Figure 4.19: Comparison between simulated and measured phase of (a) S_{11} , (b) S_{12} , (c) S_{13} , (d) S_{14} , (e) S_{22} , (f) S_{23} .

4.5. Conclusions

We presented an efficient and wideband power combiner based on a PPW structure. The proposed design is meant to combine signals from multiple PAs operating in the 28 GHz band for increased output power. The PPW is excited at several locations periodically spaced in the transverse dimension. The active impedances of the ports were shown to be very similar between the different ports and constant with frequency, allowing for wideband operation. A Doherty combiner scheme was also implemented in the PPW combiner, so that two sets of feeding points, representing main and peaking sources, can support a higher operating efficiency of the PAs over a range of output power. Based

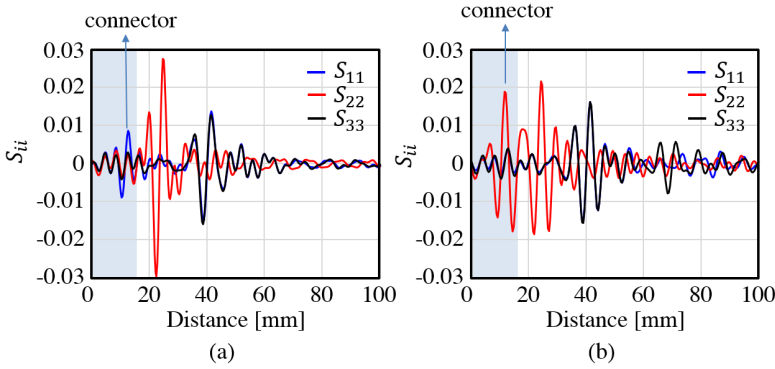


Figure 4.20: Time domain representation of the measured values of S_{11} , S_{22} and S_{33} for (a) the structure with the tapered impedance transformer from Sec. 4.3, and (b) the structure with the antenna.

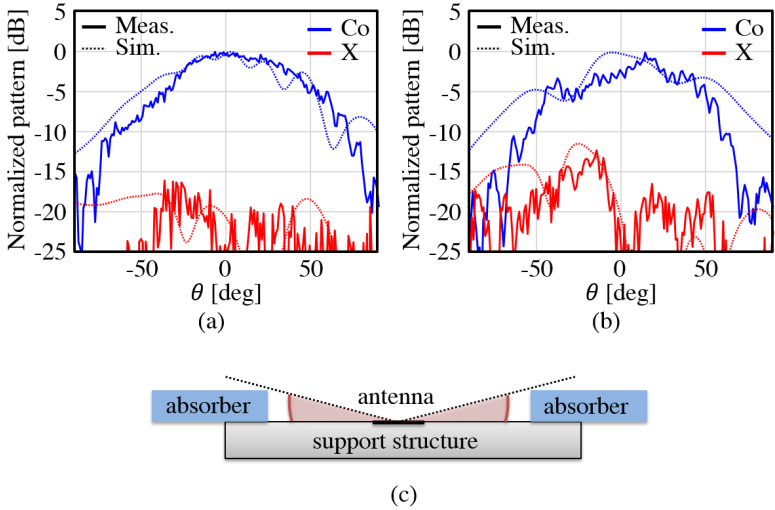


Figure 4.21: Comparison between measurements and CST of the normalized (a) E -plane and (b) H -plane patterns, while exciting port 1 at 28 GHz; (c) Schematic drawing of measurement setup, explaining lower values for high angles.

on the required power, the number of inputs connected in parallel can be easily changed.

A 6-to-1 combiner was fabricated in standard PCB technology and measurement results were presented, showing good agreements with simulated results. The efficiency of the structure, accounting for both operating efficiency of the PAs and the impedance mismatch of the combiner, was found to be around 60% over a large bandwidth, from 24 to 32 GHz that includes several relevant 5G bands for mm-wave communication.

A design of the 6-to-1 Doherty combiner integrated with an antenna was also presented. The measured S-parameters of the total structure show a good agreement with the simulations. Also, the radiation characteristics of the antenna compare well with the expected values from simulations. The waveguide folds over itself to reduce the size of

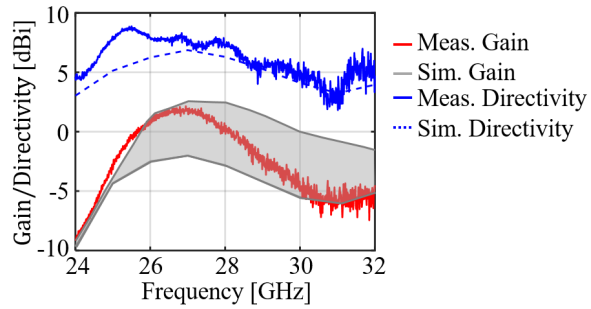


Figure 4.22: Comparison between simulation and measurement of gain and directivity.

the antenna + combiner to fit within $0.5\lambda \times 0.5\lambda$, making it suitable for possible array implementations.

Chapter 5

Implementing a PPW Combiner with Active Components

This chapter describes the implementation of the PPW combiner including active components. The waveguide is connected to an integrated circuit (IC) hosting the power amplifiers (PAs), using a flipped-chip configuration. The PA outputs feed the PPW through a slot. The shape of the slot is altered from a straight line to a meandering shape, to accommodate the aligned outputs of the IC. The transition between the IC and the PCB is discussed and the simulated performance is analyzed in terms of active input impedance for both single-ended and differential ports. The transition to a slot antenna with an artificial dielectric layer superstrate is also designed. Finally, two chips are combined with an array of two slot antennas to realize radiative spatial combining.

5.1. Coupling Slot Design

5.1.1. Meandered Slot

The first difference between the combiner presented in Ch. 4 and the design when connected to an IC is the shape of the slot. In the passive design, we considered the slots to be fed by single ended microstrip lines, as can be seen in Fig. 5.1(a). However, the output of the IC under consideration is differential, which results in a feeding structure as shown in Fig. 5.1(b), where the outputs of the IC are connected to the two sides of the slot using solder balls. However, arranging the outputs of the PAs in the configuration depicted in Fig. 5.1(b) was proven to be very difficult, because it would introduce asymmetry and unbalanced lines in the design of the PAs. For this reason, it is preferred that the outputs of the IC are all aligned. An alternative configuration of the slot that is compatible with these aligned feeding points consists of a meandered slot, as can be seen in Fig. 5.1(c).

To verify that the impedance behavior of the meandered slot is the same as that of a straight slot, a full-wave simulation of the two structures is done in CST. As an example, we consider slots fed in three points, with the geometrical parameters $w = 550\mu\text{m}$,

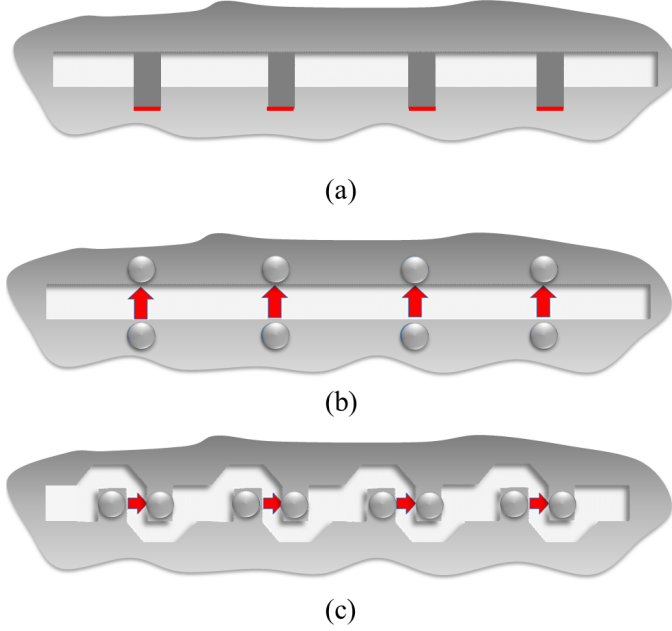


Figure 5.1: Schematic representation of a slot with its feeding structure. (a) Single ended microstrip feeds. (b) Differential feeds. (c) Differential feeds with aligned feeding points.

$h = 100\mu\text{m}$, $w_s = 100\mu\text{m}$. The PPW is filled with a dielectric with relative permittivity $\epsilon_r = 6$ and the port impedances are $Z_{\text{port}} = 50\Omega$. Figure 5.2(a) and (b) show structures under consideration. The comparison between the impedance of the combiner fed by a straight slot and the meandering slot are shown in Fig. 5.2(c). Due to symmetry the impedance of ports 1 and 3 are equal. It can be seen that the impedances are approximately equal and differ by up to 5Ω . For the given example, the real part of the impedance is approximately equal to $Z_{\text{PPW}} = 56\Omega$ as expected from (4.1), while the imaginary part is about 25Ω and can typically be adjusted with the size of the feed and the width of the slot. The required active input reactance is typically not equal to 0, but it should be inductive to improve matching with the PA and to compensate for the parasitic effects.

5.1.2. Combiner Design and Matching to PA

In Ch. 4 a purely real output impedance of the PAs was assumed, where the PA was designed such that any inductive and capacitive parasitics would cancel out. However, for the PAs on the IC considered here this is not the case. Instead, the ideal differential output impedance of the PAs is $Z_{\text{PA}} = (27 + j22)\Omega$. The PAs are connected to the PCB with the waveguide via the output pads on the IC and solder balls, as shown in Fig. 5.3(a). The output pads add a capacitance, $C_{\text{pad}} = 50\text{fF}$, and the solder bump an inductance, $L_{\text{SB}} = 50\text{pH}$, as shown in Fig. 5.3(b), so that the desired differential input impedance of the waveguide becomes $Z_{\text{WG,ideal}} = (22 + j6)\Omega$. In order to make the actual Z_{WG} close to this ideal value, we choose the Rogers RO3010 ($\epsilon_r = 11.2$) with a height of $h = 130\mu\text{m}$

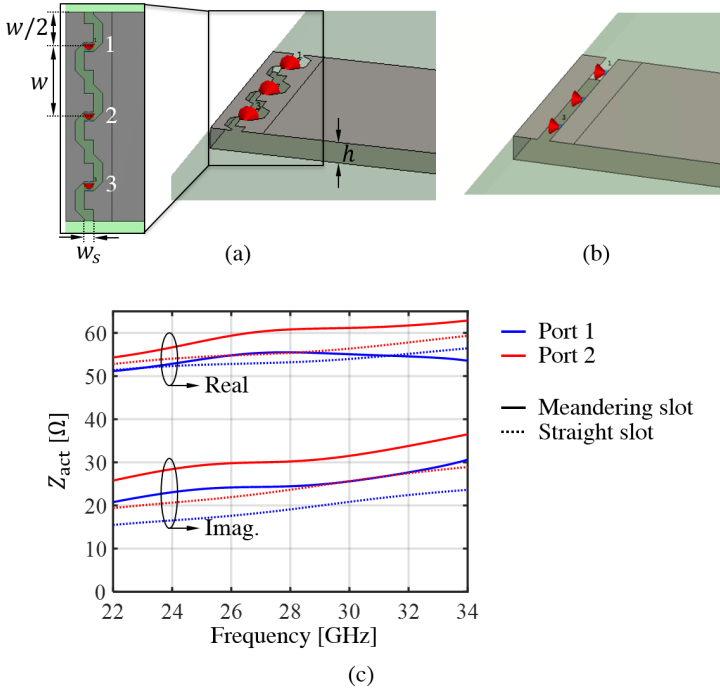


Figure 5.2: Comparison between impedance behavior of a PPW fed by (a) meandering slot or (b) a straight slot, (c) real and imaginary part of the impedance.

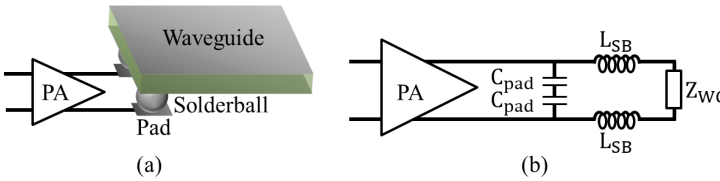


Figure 5.3: Connection between PA and waveguide via output pads and solderballs: (a) schematic overview and (b) equivalent circuit.

as the medium inside the PPW. The distance between the outputs of the IC was fixed by the PA design to $w = 550 \mu\text{m}$, so that, from (4.1), the impedance of the waveguide equals $Z_{PPW} = 26.6 \Omega$.

We designed the 4-to-1 PPW combiner as shown in Fig. 5.4(a), as the IC under consideration has four PAs. A stepped impedance transformer consisting of four $\lambda/4$ sections (where the wavelength in the dielectric is considered) is added to the waveguide, to transform the impedance of the PPW from approximately 6Ω to a microstrip line of 40Ω . The widths of the four sections are: $w_1 = 1.9 \text{ mm}$, $w_2 = 1 \text{ mm}$, $w_3 = 370 \mu\text{m}$ and $w_4 = 140 \mu\text{m}$. Rather than closing the waveguide behind the slot with a short circuit, an open ended stub with a length of $\lambda/4$ is chosen. This is because, due to the design rules of the PCB and the meandering shape of the slot, the short could not be placed close

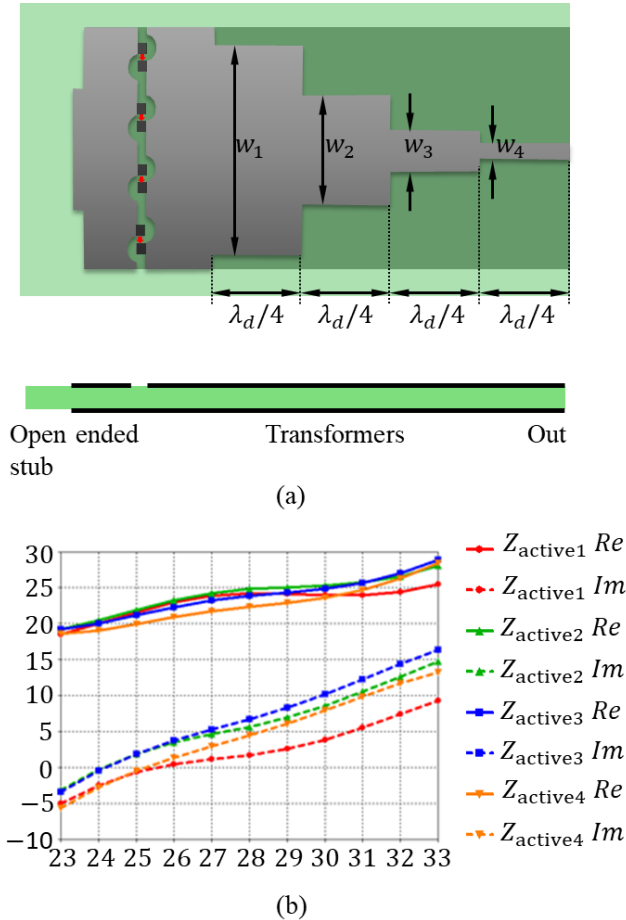


Figure 5.4: (a) 4-to-1 PPW combiner with a stepped impedance transformer to 40Ω . (b) Active impedance of the four ports.

enough to the slot, causing the impedance to change significantly. The extension in the center of the waveguide behind the feeding points is added to reduce the differences of impedances among the four ports, as the center feeds exhibit slightly higher active impedance with respect to the edge feeds. The active impedances of the four ports are shown in Fig. 5.4(b). It can be seen that, at the center frequency of 28 GHz, the impedance of all four ports is approximately equal to the desired value $Z_{\text{WG,ideal}} = (22 + j6)\Omega$.

5.2. Impact of the IC

While designing the waveguide combiner, the impact of the IC itself cannot be neglected. The IC is added above the slot, as shown in Fig. 5.5(a). Solder bumps connect the output pads on the bottom metal layer of the IC to the PCB. A layer of passivation with a height of $3\mu\text{m}$ separates the output pads from the ground plane of the IC. The output pads

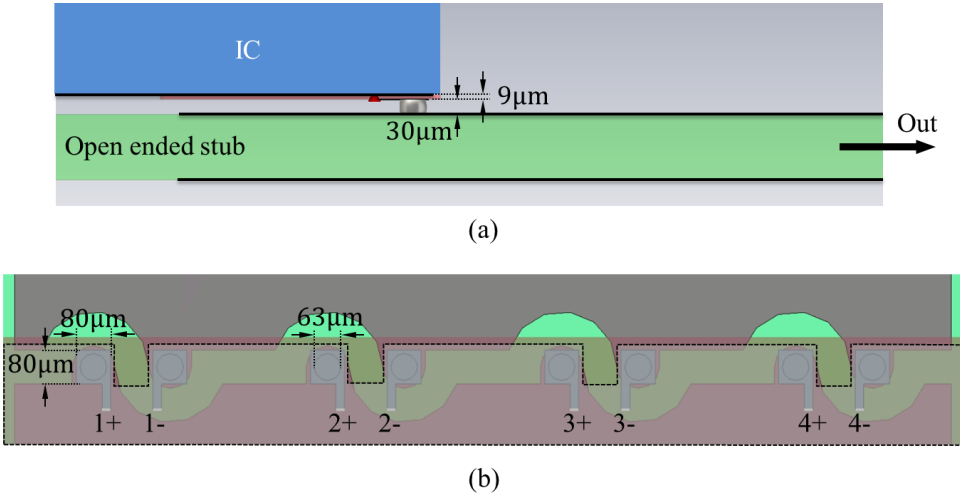


Figure 5.5: Transition from the PAs to the PCB (a) side view, (b) details of the transition on the IC. The dashed outline shows the ground plane of the IC.

are $80 \times 80 \mu\text{m}^2$ in size, and the solder bumps have a height of $30 \mu\text{m}$ and a diameter of $63 \mu\text{m}$. The width of the slot $w_s = 80 \mu\text{m}$. From the output pads, short thin microstrip lines are added that connect to the PAs on the chip. It can be seen that, rather than four differential outputs, the IC has eight pseudo-differential outputs, where e.g. ports 1+ and 1- have a 180° phase shift. Since the output pads and solder balls are included in the structure, the desired differential impedance of the combiner is $Z_{PA} = (27 + j22) \Omega$, or for each of the eight pseudo-differential ports $Z_{PA,p.d.} = (13.5 + j11) \Omega$.

5.2.1. Undesired Air Gap Mode

One effect of adding the IC to the combiner structure is the excitation of an undesired PPW mode between the continuous ground plane of the IC and the top metal plate of the waveguide, as shown in Fig. 5.6(a). Besides a loss of efficiency, as some power launched in the undesired PPW mode is not entering the combiner, this PPW mode also results in a large difference in the impedances of the individual ports. This effect can be observed in Fig. 5.6(b), where the active input impedance of the individual single-ended ports in a pseudo differential excitation are shown. A large impedance variation among the different ports can be seen, caused by the non symmetric structure of the slot and by the energy propagating in the air gap and being reflected back to the feed. Also, the differential impedance, when the impedances related to the positive and negative ports of the four PAs are summed, is shown in Fig. 5.6(b), where it can be observed that the combined impedance of the differential feeds are approximately equal. Although the asymmetry of the slot cannot be corrected because of the arrangement of the bumps, a mitigating solution for the undesired air-gap mode is proposed.

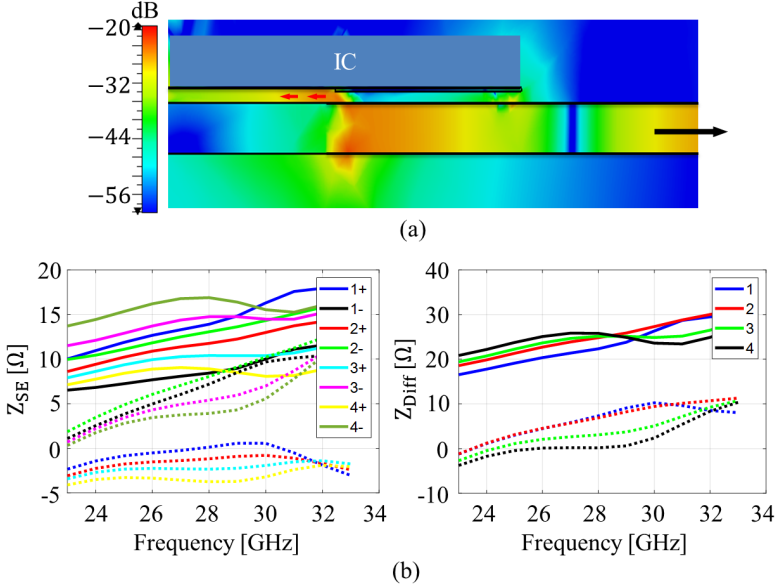


Figure 5.6: (a) Undesired PPW mode excited between the PCB and the ground plane of the IC. (b) Active impedance of the feeds, single ended and differential. Solid: real part, dotted: imaginary part.

5.2.2. Folded Open Stub

The waveguide open ended stub is folded to a lower dielectric layer, as it can be observed from the side view in Fig. 5.7(a). The slot between the two layers has a width of $w_{s,\text{fold}} = 100 \mu\text{m}$. The second layer consists of a $101 \mu\text{m}$ thick slab of Rogers RO4450F ($\epsilon_r = 3.52$). By folding the open ended stub to a lower layer, the effect of the undesired PPW mode between the PCB and the ground plane of the IC is reduced. This can be seen from the active impedance of the single ended feeds as shown in Fig. 5.7(b). Compared to the impedances shown in Fig. 5.6(b), of the structure without the folding, it can be seen that the impedances of the individual ports are more similar to the desired value. The differential impedances are still approximately equal.

5.2.3. Co-Optimization of the PA Circuit and Combiner

The length of the stub, l_{stub} , is optimized together with the full circuit simulation of the PAs for best performance of the entire system. The 9-port S-parameter files from CST are imported in ADS to consider the total output power of the PAs and the combiner as well as the error vector magnitude (EVM). This full circuit simulation is performed in another Ph.D. project, and will not be discussed in detail here. It is found that the EVM of the PAs with the combiner was good, i.e. < -30 dB. The final value of $l_{\text{stub}} = 1.16$ mm which resulted in maximum total output power reaching a watt-level magnitude. To reduce the undesired PPW mode even further, two solder balls are stacked, so that the total height between PCB and IC is now $60 \mu\text{m}$. This increases the inductance of the solder balls, but this effect is accounted for in the simulation.

The active impedance as seen from the eight single ended feeding points is shown in

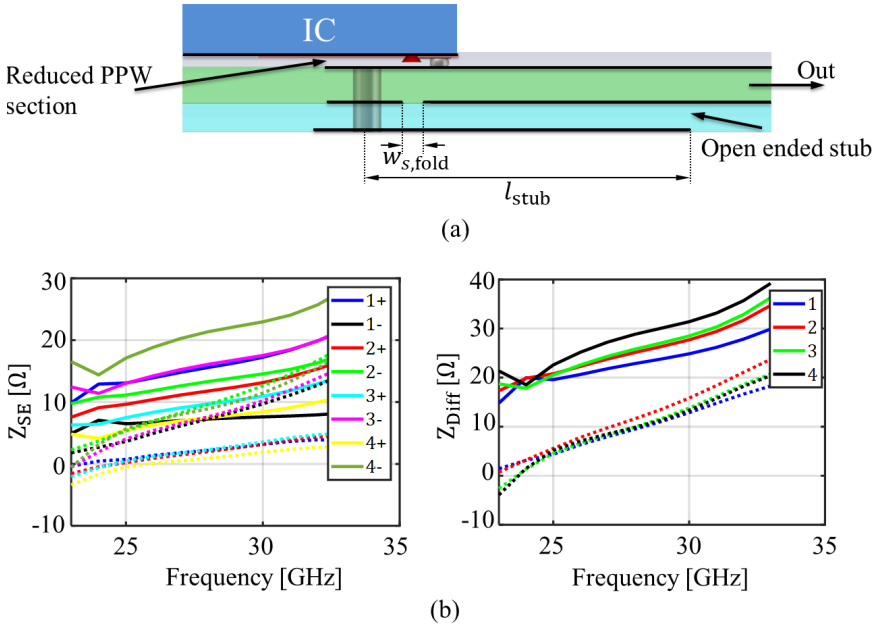


Figure 5.7: (a) Combiner with the open ended stub folded in another layer to reduce the effect of an undesired PPW mode between the ground plane of the IC and the top metal plate of the waveguide. (b) Active impedance of the feeds, single ended and differential. Solid: real part, dotted: imaginary part.

Fig. 5.8(a). It can be seen that, due to the asymmetry between the positive and negative feeds with respect to the slot, there is a large variation between the active impedance seen from each port. However, when the impedances related to the positive and negative ports of the four PAs are summed, as shown in Fig. 5.8(b), the active impedances are very similar and close to the desired value of $(27 + j22)\Omega$ at the center frequency of 28 GHz.

5.3. Output of the Combiner

Similar to the combiner presented in Ch. 4, two types of outputs are considered for the combiner: a coaxial connector and an antenna.

5.3.1. Coaxial Output

The structure of the combiner with the transition to the connector output is shown in Fig. 5.9. A transition is designed to convert the microstrip output of the combiner to a larger microstrip line with increased width and distance from the ground plane to adapt to the coaxial line dimensions. The reflection and transmission coefficient of the transition is shown in Fig. 5.10, where a good matching is shown. The used connector is an end launch Southwest Microwave 2.92 mm connector [71].

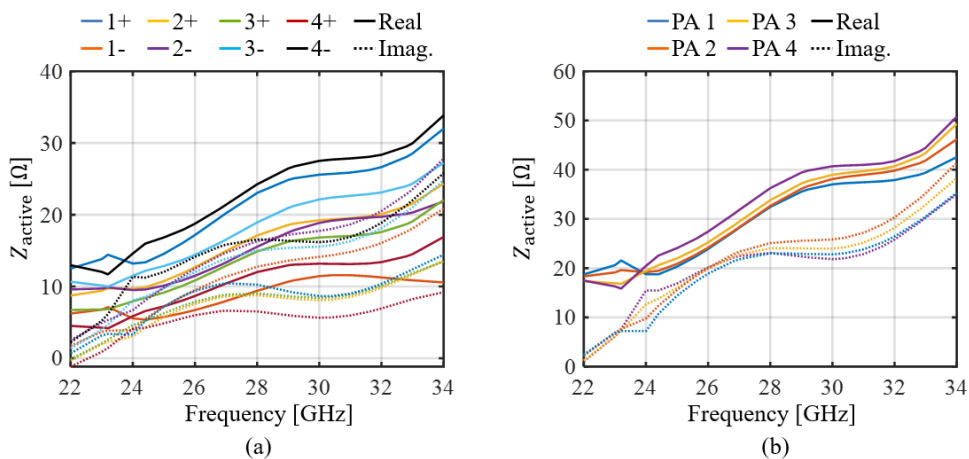


Figure 5.8: Active impedances as seen from the different PAs feeding the combiner. (a) Single ended impedance. (b) Differential impedance.

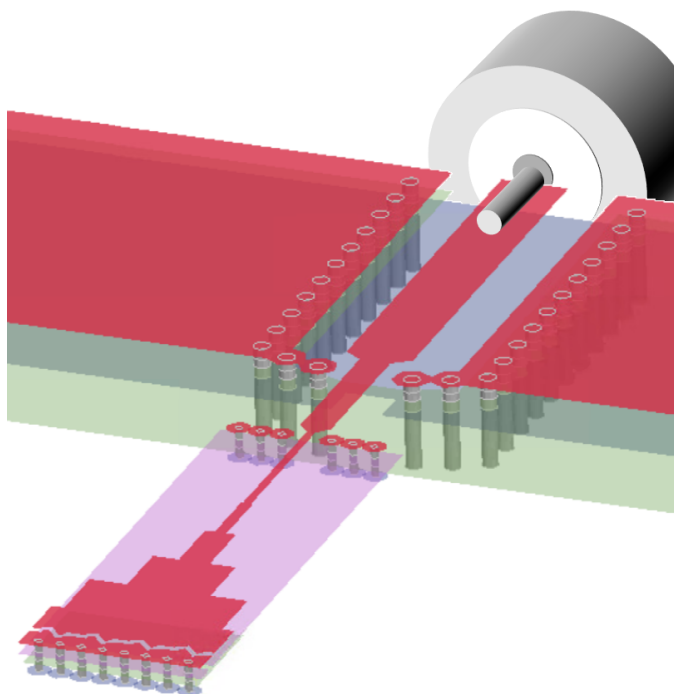


Figure 5.9: 4-to-1 Combiner with transition to an edge mounted connector as output.

5.3.2. Single Antenna Output

As an antenna element a cavity backed slot antenna is chosen. A two layer ADL superstrate is added for impedance matching purposes. The stack-up of the designed PCB is

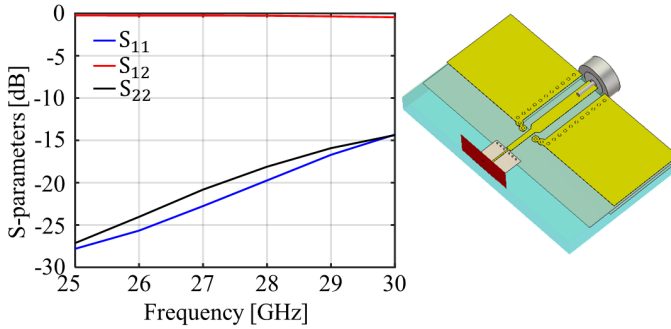


Figure 5.10: Reflection and transmission coefficient of the transition from the combiner to the coaxial connector.

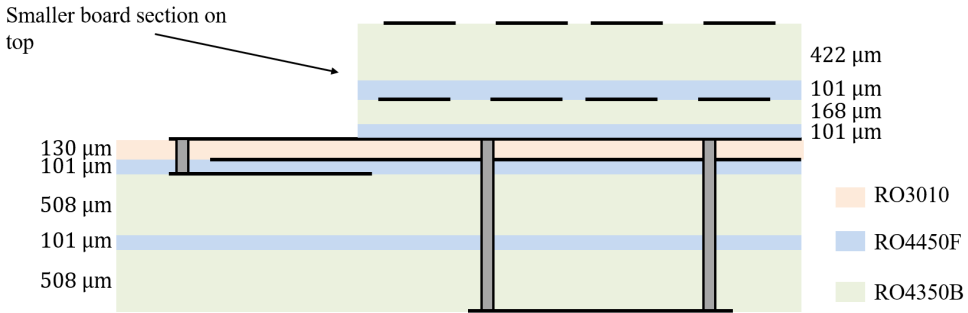


Figure 5.11: Stack-up of PCB with power combiner and the cavity backed slot with ADL superstrate.

shown in Fig. 5.11. The designed slot antenna with the 4-to-1 combiner is shown in Fig. 5.12. The length of the slot is $l_s = 3.5$ mm and its width is $w_s = 0.6$ mm. The height of the cavity is $h_{cav} = 1.348$ mm and its planar dimensions are $x_{cav} = 3.8$ mm and $y_{cav} = 3.8$ mm. The geometrical parameters of the ADL are $p = 1$ mm, $w = 150 \mu\text{m}$, $d_z = 523 \mu\text{m}$ and $s_x = 0$ and $s_y = 0.5p$. The reflection coefficient normalized to 50Ω is shown in Fig. 5.13. It can be seen that the antenna including the transition is well matched over the frequency band of interest.

5.3.3. Two-Antenna Array

Another structure is considered, with two identical structures mirrored next to each other, as shown in Fig. 5.14. By exciting the two combiners simultaneously from two ICs, the power radiated by the two antennas is combined in the air, creating an 8-to-1 combiner to further increase the output power.

5.4. Conclusions

The integration of the power combiner with an active circuit was presented. The PPW combiner is altered compared to the original design to facilitate the landing of the IC with the PAs. The slot is meandered, so that the output pads from the IC could be all on

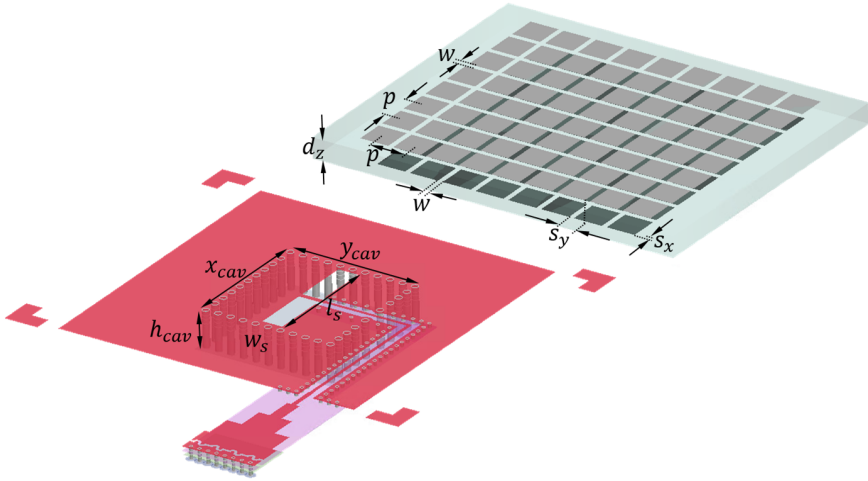


Figure 5.12: Combiner with cavity backed slot antenna as output.

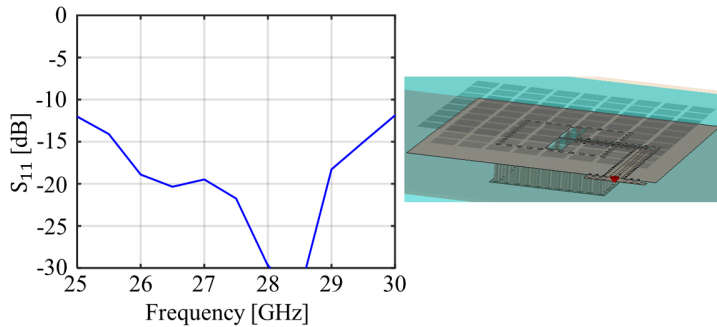


Figure 5.13: Reflection coefficient of the transition from the combiner to the cavity backed slot antenna.

a line. Also, to reduce an undesired PPW mode between the IC and the top metal plate of the waveguide, the open ended stub of the combiner is folded to a lower layer in the PCB. The active impedance of the different feeding points is optimized for the optimal operating conditions of the PAs. A PCB is designed, where the combiner has either a connector as output, or a cavity backed slot antenna.

A prototype of the presented structure is currently being manufactured and will be tested in future work.

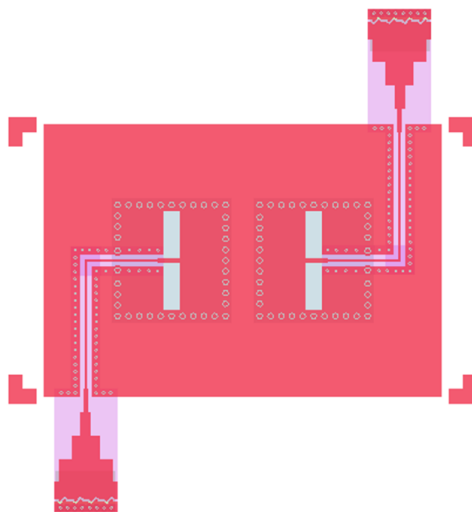


Figure 5.14: Two combiners with cavity backed slot antennas next to each other to further increase output power.

Chapter 6

Phased Array with Pattern Shaping and Scan Loss Reduction for Millimeter Waves

In this chapter, we investigate antenna concepts to reduce the scan loss in phased array design. Planar slot antenna elements are used in array configuration, in combination with artificial dielectrics layers located in the close proximity of the array, to achieve pattern shaping. Spectral domain representations are used for the analysis of the leaky waves propagating within the stratification. The artificial dielectric superstrate supports leaky waves that can be optimized to enhance the gain in a specific angular region or to enlarge the array field-of-view. By controlling the amplitude and phase of the antenna elements, the proposed concepts can be used to realize adaptive arrays, which can change their combined radiation pattern in different operating conditions. A design of a four element array is fabricated in standard printed circuit board technology and the results are presented, showing good agreement with simulations.

6.1. Slot with ADL Superstrate in Free Space

To illustrate the antenna concept, we first assume that the slot radiators and the ADL superstrate are in free space. Although not physically realizable, this ideal case allows highlighting the main radiation mechanism.

6.1.1. Single Slot

The geometry under consideration is shown in Fig. 6.1 and consists of a slot oriented along x , in the presence of a two-layer ADL superstrate. Each ADL is realized as a doubly periodic array of electrically small square patches. The period p is assumed to be smaller than a quarter wavelength, within the frequency band of investigation. The width of the gaps between the patches is w and the relative shift between the top and bottom layer is s . The distance between the slot plane and the bottom ADL is h_1 and the distance be-

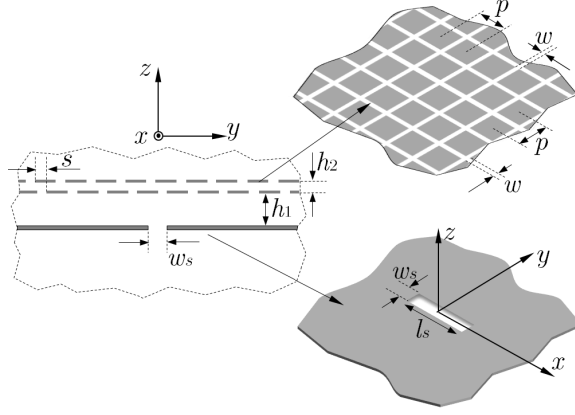


Figure 6.1: Slot in the presence of an ADL superstrate, with the characteristic geometrical parameters.

tween the two ADLs is h_2 . The slot is assumed to be electrically narrow, with width w_s , much smaller than the wavelength, while the slot length is indicated as l_s . For the calculation of the directivity and radiation patterns, only the upper hemisphere is considered in this section. For example, this can be realized in practice with a cavity-backed slot, which radiates only in the upper half space.

When the ADLs are illuminated by a near source rather than a plane wave, the procedure presented in [28] can be used to evaluate the far field of the source in the presence of the ADLs. The approach involves expanding the radiated field from the source in a spectrum of plane waves and using the equivalent transmission line model in Fig. 6.2. For each plane wave, characterized by the wavenumbers k_x and k_y along the x - and y -directions, the propagation constant on the line is given by $k_z = (k_0^2 - k_p^2)^{1/2}$, where k_0 is the free space wavenumber and $k_p^2 = k_x^2 + k_y^2$. Z_0^{Ti} is the characteristic impedance of the transmission lines for either the transverse magnetic (TM) or the transverse electric (TE) modes: $Z_0^{TM} = \zeta_0 k_z / k_0$ and $Z_0^{TE} = \zeta_0 k_0 / k_z$, where $\zeta_0 = 120\pi\Omega$. The ADLs are represented in the circuit by two shunt reactances (X_1^{Ti} and X_2^{Ti}), where Ti can refer to either TM or TE components of the wave. This circuit allows to define the spectral dyadic Green's function of the ADL stratification, which can be derived from the current and voltage solutions of these transmission lines when fed by a unit voltage generator at $z = 0$. If we assume the two layers to be identical, the equivalent reactance X^{Ti} is known in closed-form as a function of the geometrical parameters [29]:

$$X^{TM} = \frac{-1}{B}, \quad X^{TE} = \frac{-1}{B \left(1 - \frac{k_p^2}{2k_0^2}\right)} \quad (6.1)$$

where B is the susceptance of the layers, given by

$$B = j\omega\epsilon_0 \frac{p}{2\pi} \sum_{m \neq 0} \frac{|\text{sinc}(\pi m \frac{w}{p})|^2}{|m|} F_m(h_2, p, s) \quad (6.2)$$

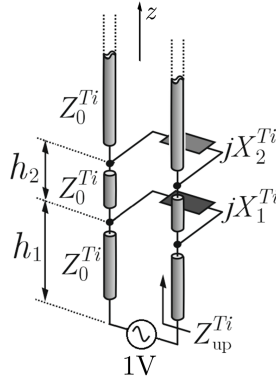


Figure 6.2: Transmission line equivalent circuit of a source in the presence of two ADLs, for both TE and TM waves.

with

$$F_m(d_z, p, s) = -j - \cot\left(-j2\pi|m|\frac{h_2}{p}\right) + e^{j2\pi m \frac{s}{p}} \csc\left(-j2\pi|m|\frac{h_2}{p}\right). \quad (6.3)$$

The spectrum of the magnetic current on the slot is defined assuming a sinusoidal distribution in the longitudinal direction

$$M_l(k_x) = 2k_0 \frac{\cos(k_x l_s/2) - \cos(k_0 l_s/2)}{(k_0^2 - k_x^2) \sin(k_0 l_s/2)} \quad (6.4)$$

and edge-singular in the transverse direction:

$$M_t(k_y) = J_0(k_y w_s/2) \quad (6.5)$$

where J_0 is the Bessel function of the first kind and zeroth order. The electric field in the far field on a hemisphere with radius r_0 , can be found for all observation angles θ_0 and ϕ_0 using the stationary phase point approximation as

$$E_\xi(r_0, \theta_0, \phi_0) \approx jk_{z0} G_{\xi x}^{em}(k_{x0}, k_{y0}, z = h_1 + h_2) \times M_l(k_{x0}) M_t(k_{y0}) \frac{e^{-jk_0 r}}{2\pi r_0} \quad (6.6)$$

where ξ can refer to the x , y or z component of the field, $k_{x0} = k_0 \sin\theta_0 \cos\phi_0$, $k_{y0} = k_0 \sin\theta_0 \sin\phi_0$ and $k_{z0} = k_0 \cos\theta_0$. $G_{\xi x}^{em}$ is the electric field Green's function in the ξ -direction due to x -oriented magnetic currents and is evaluated from the transmission line in Fig. 6.2, above the stratification ($z = h_1 + h_2$).

Figure 6.3(a) shows the directivity of the slot in the presence of the ADLs at a single frequency $f = f_0$ in the two principal planes. The geometrical parameters of the structure are: $l_s = \lambda_0/2$, $w_s = \lambda_0/15$, $h_1 = 0.08\lambda_0$, $h_2 = 0.03\lambda_0$, $p = 0.2\lambda_0$, $w = 0.06\lambda_0$ and

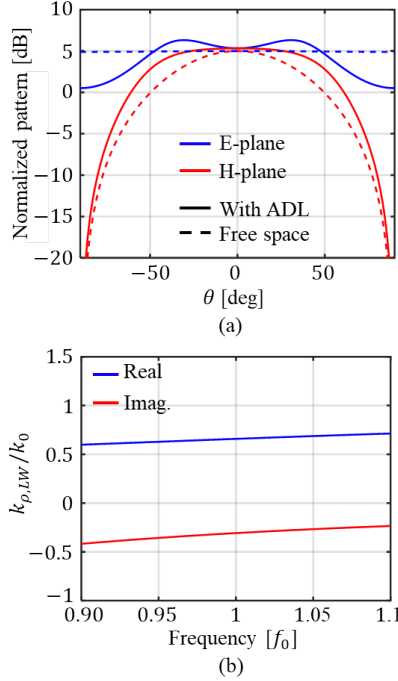


Figure 6.3: (a) Directivity of a slot in free space and in the presence of the ADL superstrate. The geometrical parameters of the structure are: $l_s = \lambda_0/2$, $w_s = \lambda_0/15$, $h_1 = 0.08\lambda_0$, $h_2 = 0.03\lambda_0$, $p = 0.2\lambda_0$, $w = 0.06\lambda_0$ and $s = 0.3p$. (b) Dispersion curve of the TM₀ leaky wave pole supported by the structure.

$s = 0.3p$, where λ_0 is the free space wavelength at f_0 . The directivity of the slot in free space, i.e. without the ADL superstrate, is also shown as a reference.

A clear increase in directivity in the E -plane is visible towards $\theta = \pm 35^\circ$, which corresponds to the TM₀ leaky wave supported by the structure. Figure 6.3(b) shows the dispersion curve of the leaky wave pole. The pole can be found by solving the dispersion equation $Z_{\text{up}}^{\text{TM}} = 0$, where $Z_{\text{up}}^{\text{TM}}$ is the impedance seen upwards from the slot through the TM transmission line model of the stratification, as shown in Fig. 6.2. The sign of the square root $k_z = \pm (k_0^2 - k_\rho^2)^{1/2}$ is chosen such that we consider the poles of the Green's function located on the bottom Riemann sheet. The angle of maximum radiation in the element pattern can be related to the leaky wave pole as [72]

$$\theta_{LW} = \tan^{-1} \left(\frac{\text{Re}\{k_{\rho,LW}\}}{\text{Re}\left\{\sqrt{k_0^2 - k_{\rho,LW}^2}\right\}} \right). \quad (6.7)$$

The imaginary part of the leaky wave pole is related to the attenuation constant of the leaky wave and can be used to determine the required distance between the slot and the truncated edges of the ADLs, such that reflection from the edges of the structure becomes negligible.

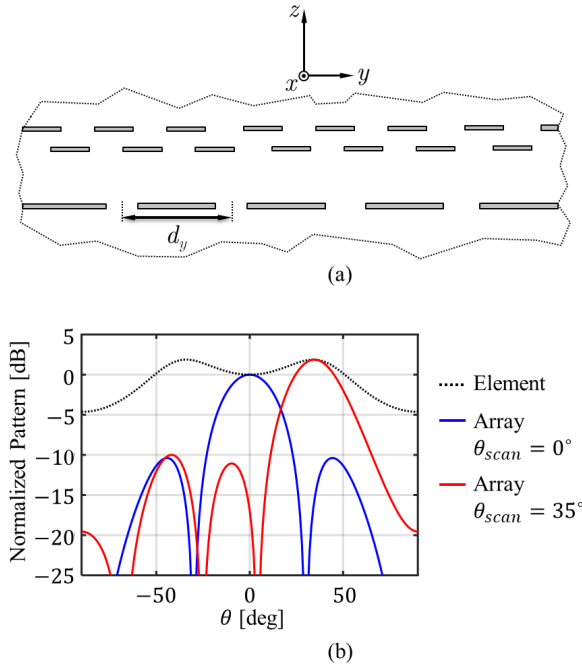


Figure 6.4: (a) Array of four slots in the presence of an ADL superstrate in free space. The slots are displaced in y -direction by a distance of $d_y = \lambda_0/2$. (b) Normalized radiation patterns of the array while scanning to broadside direction and to 35° . Also the element pattern shape is shown.

Although a simple slot in free space has a constant radiation pattern in the E -plane and would therefore satisfy our requirement for a broad element pattern, this is not practically implementable. As the slot radiates the same amplitude towards $\pm 90^\circ$ as to broadside, the finiteness of the ground plane will cause significant diffraction and the pattern would be strongly dependent on the size of the ground plane. The ADL superstrate allows for an increase of gain towards a certain angle, while decreasing the power radiated to $\pm 90^\circ$, making the patterns less sensitive to the truncation of the ground plane.

6.1.2. Array of Slots

We now consider the same slot element in an array configuration, as shown in Fig. 6.4(a). As an example, we consider four slots that are displaced by a distance d_y in the y -direction and fed with a linear phase shift for scanning in the E -plane. This number of elements is realistic considering the limited number of channels coming from a mm-wave chip. Figure 6.4(b) shows the normalized radiation pattern of the array of four slots, with $d_y = \lambda_0/2$. The pattern is shown for broadside and scanning to 35° . It can be seen that the leaky waves characterizing the element patterns can be used to enhance the directivity of the array when scanning in specific directions.

To implement a variable beamwidth, instead of applying a linear phase shift between the excitation of the four slots, one can apply a quadratic phase distribution [73], placing

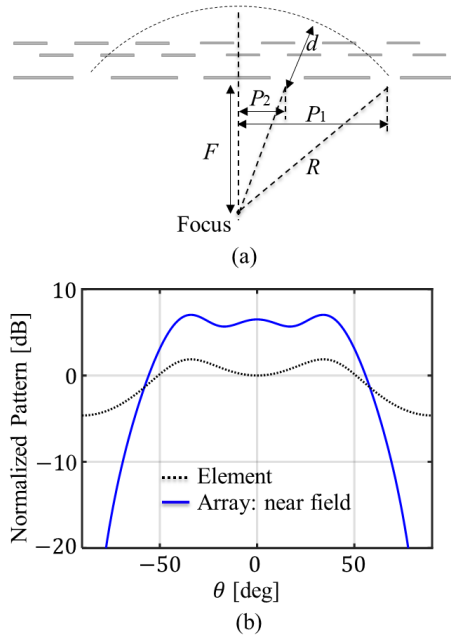


Figure 6.5: (a) Geometry of the array for the quadratic phase shift. (b) Normalized radiation patterns of a single slot and of the array of four slots while focusing in the near field.

a virtual focus point behind the array, as shown in Fig. 6.5(a). This configuration creates a diverging pattern that realizes a large beamwidth. For the four element array, the phase difference between the outer and the inner elements can be calculated by assuming virtual sources located along a circle centered around a focus point. This is achieved by applying a phase shift to the inner elements equal to $\beta_q = k_0 d$, where $d = R - (P_2^2 + F^2)^{1/2}$ is the distance between the inner elements and the circle with radius $R = (P_1^2 + F^2)^{1/2}$. This is combined with a tapered amplitude of the excitations $A = [0.6 \ 1 \ 1 \ 0.6]$, to reduce the oscillations in the pattern. In the array under consideration, $P_1 = 1.5d_y$ and $P_2 = 0.5d_y$. Figure 6.5(b) shows the pattern of the array with a phase distribution of $\phi = [0^\circ \ 101^\circ \ 101^\circ \ 0^\circ]$ (corresponding to $F = 0.7\lambda_0$), normalized to the broadside value of the isolated element pattern, which is also shown. It can be seen that by applying a quadratic phase shift between the elements, the pattern of the array is still wide and the amplitude is about 6dB higher than that of an isolated element resulting in higher transmitted power.

By switching between the linear phase shift and the near field focus, the same array can be used both to scan to large angle with enhanced gain, or to have a wide field-of-view.

6.2. Study on Gain Enhancement and Mutual Coupling

In the previous section, only radiation properties were considered. However, when trying to optimize also the impedance matching, a trade-off must be made between pattern control and mutual coupling. The leaky waves supported by the cavity between the antennas and the ADL superstrate enhance the element gain pattern in certain directions, but can also lead to higher mutual coupling since they travel in the air gap from one antenna element to the neighboring one. The increase of mutual coupling is undesired, as it causes a deterioration of the active impedance matching when scanning.

To address this trade-off, a study is done, similar to the one presented in [74], for cavity backed slots in the presence of the ADL superstrate, as shown in Fig. 6.6. The slots are oriented along x , and both the cavity backed slots and the ADLs are considered to be printed on a dielectric with relative permittivity $\epsilon_r = 3.5$. When including the dielectric layers, the Eqs. (6.1)-(6.4) can still be used, but replacing ϵ_0 and k_0 with ϵ_{av} and k_{av} , i.e. the average permittivity and wavenumber between the media above and below the artificial dielectric layer or the slot plane. A parametric study is performed, where the distance between the slot array and the ADL superstrate, h_1 , is varied, as well as the effective refractive index of the ADL by varying the value of w . Since the slots are identical, the mutual coupling, S_{12} is found from the mutual admittance as [75]:

$$S_{12} = \frac{-2Y_{12}Y_0}{(Y_{11} + Y_0)^2 - Y_{12}^2} \quad (6.8)$$

where Y_0 is the normalization admittance of the two slots. The mutual admittance can be evaluated as a spectral integral as [74]:

$$Y_{12} = \frac{-1}{(2\pi)^2} \int_0^{2\pi} \int_0^\infty |M(k_\rho, \alpha)|^2 G_{xx,up}^{hm}(k_\rho, \alpha) e^{-jk_\rho \cos(\alpha - \pi/2)d_y} k_\rho dk_\rho d\alpha \quad (6.9)$$

where $M(k_\rho, \alpha) = M_l(k_\rho, \alpha)M_t(k_\rho, \alpha)$ from (6.4) and (6.5), and k_ρ and α are related to the spectral variables k_x and k_y as $k_\rho = (k_x^2 + k_y^2)^{1/2}$ and $\alpha = \tan^{-1}(k_y/k_x)$. $G_{xx,up}^{hm}$ is the x -component of the spectral Green's function for magnetic fields due to magnetic currents oriented along x , for the medium above the slots, which is found analytically as described in the previous section (Fig. 6.2), and d_y is the center-to-center distance between the slots.

The self admittance can be computed as the sum of two terms:

$$Y_{11} = Y_{11,up} + Y_{11,down} \quad (6.10)$$

with

$$Y_{11,up} = \frac{-1}{(2\pi)^2} \int_0^{2\pi} \int_0^\infty |M(k_\rho, \alpha)|^2 G_{xx,up}^{hm}(k_\rho, \alpha) k_\rho dk_\rho d\alpha \quad (6.11)$$

and

$$Y_{11,down} = \frac{-1}{2\pi} \int_{-\infty}^\infty \frac{1}{w_{cav}} \sum_{m=-\infty}^\infty |M_t(k_{ym})|^2 G_{xx,down}^{hm}(k_x, k_{ym}) |M_l(k_x)|^2 dk_x \quad (6.12)$$

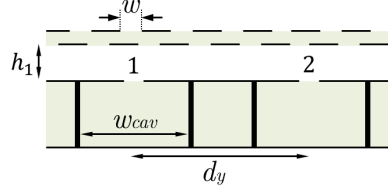


Figure 6.6: Geometry under consideration for the study on the gain enhancement and the mutual coupling, consisting of cavity backed slots with an ADL superstrate.

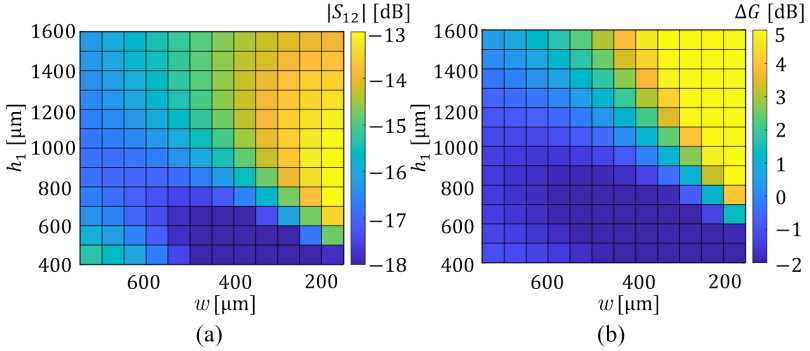


Figure 6.7: (a) $|S_{12}|$ and (b) ΔG of the element pattern of the cavity backed slots in the presence of the ADL superstrate while varying h_1 and w .

with $k_{ym} = -(2\pi m)/w_{cav}$ being the wavenumbers of the Floquet modes accounting for the periodic nature in y -direction enforced by the cavity side walls [27]. $G_{xx,down}^{hm}$ is the x -component of the spectral Green's function of the stratification below the slots. For a fair comparison of S_{12} , one must make sure that the slots are well matched, therefore we impose $Y_0 = Y_{11}$. Besides the mutual coupling, the gain enhancement, defined as $\Delta G = G(45^\circ) - G(0^\circ)$, is found from the isolated element patterns for every h_1 and w .

Figure 6.7 shows the resulting S_{12} and ΔG at a frequency of 30GHz, while varying h_1 from 400 μm to 1600 μm , and w from 750 μm to 150 μm . This variation of w corresponds to a variation of the effective refractive index of the ADL from 2.5 to 5. The other geometrical parameters are: $l_s = 5\text{ mm}$, $w_s = 0.2\text{ mm}$, $w_{cav} = 1.3\text{ mm}$, $d_y = 5\text{ mm}$, $h_2 = 0.2\text{ mm}$, $p = 1.2\text{ mm}$ and $s = 0$. Comparing the maps in Fig. 6.7(a) and (b), it can be seen a gradient of increasing ΔG corresponds to increasing values of mutual coupling. During the design phase, it was observed that mutual coupling above -15 dB leads to large variations of the active input impedance of the array elements when scanning in a $\pm 45^\circ$ angular range. Therefore, combinations of the parameters h_1 and w that provide a mutual coupling of -15 dB or lower are considered for the design. For this values of S_{12} the gain difference is close to 0 dB for the lower values of h_1 and increasing to about 2 dB for the higher values of h_1 . However, larger distances from the ADL also yield to more dispersive patterns and larger impedance variation with the frequency.

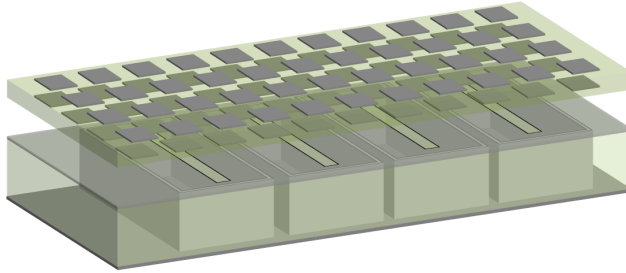


Figure 6.8: Geometry of the array of cavity backed slots in the presence of an ADL superstrate.

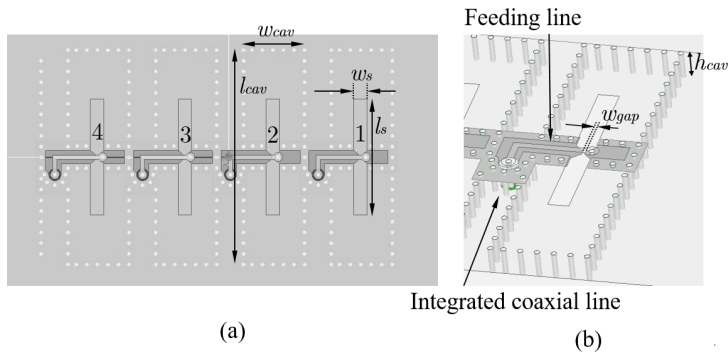


Figure 6.9: (a) Top view of the slot array and (b) 3-D view of an array element with feeding structure.

6.3. Array Design

An array design operating around 30 GHz is presented in this section, based on the schematic geometry shown in Fig. 6.8. It consists of four cavity backed slot antennas in the presence of a two-layer ADL superstrate separated by an air gap. Both the array and the ADL superstrate can be fabricated using standard PCB technology, where a foam layer can be used to realize the air gap between the slots and the ADL.

A more detailed figure of the designed array is shown in Fig. 6.9. Based on the trade-off presented in Sec. 6.2, the following geometrical parameters are derived: $l_s = 6.6$ mm, $w_s = 0.75$ mm, $w_{cav} = 3.4$ mm, $l_{cav} = 12.2$ mm, $h_{cav} = 1$ mm. The cavity is realized with via walls and the slot is fed with a grounded co-planar waveguide (GCPW), which in turn is connected to an integrated coaxial line to reach the feeding network below the ground plane. The GCPW is terminated on a short circuit with a via, where the slot is tapered to a narrower width $w_{gap} = 100$ μ m. The total size of the slot plane and the ADLs in x - and y -directions is 7.5 mm \times 17 mm.

The dimensions of the ADLs are $p = 1.2$ mm, $w = 0.4$ mm and $s = 0$. The layer stack-up of the demonstrator board is shown in Fig. 6.10(a). Three versions of the demonstrator are realized with different feeding networks to achieve the various radiation cases, i.e. broadside, scanning to 45° and the wide beam. The broadside, scanning and broad beam feeding networks are shown in Fig. 6.10(b)-(d) respectively.

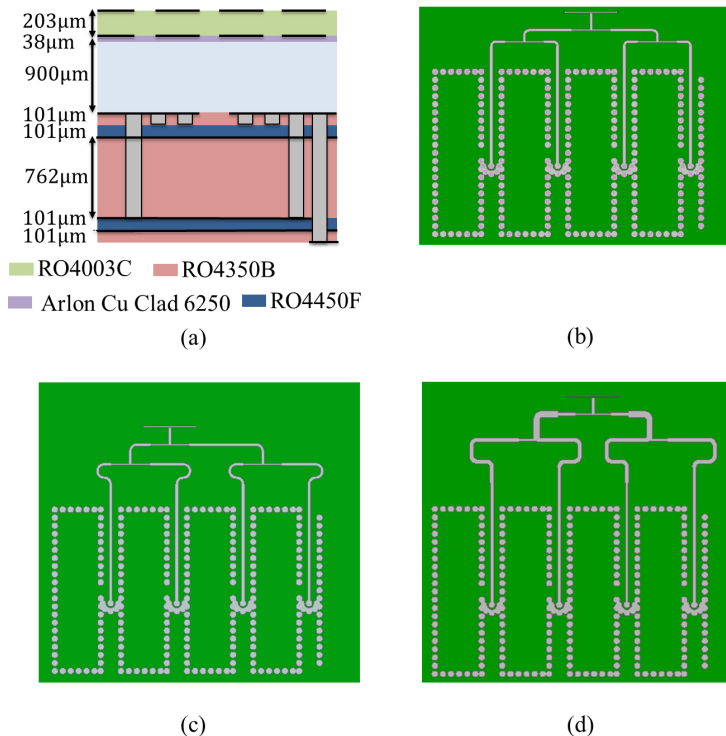


Figure 6.10: (a) Stack-up of the demonstrator board. Bottom views of the broadside (b), scanning (c) and broad beam (d) boards, showing the feeding networks.

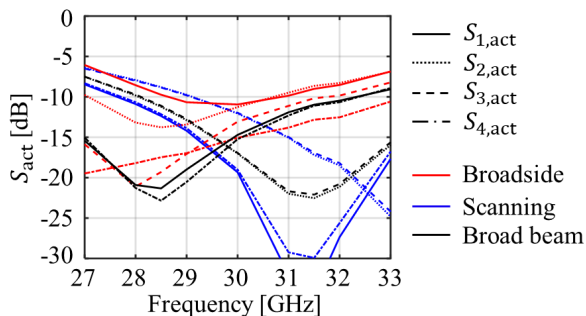


Figure 6.11: Active S-parameters of the four individual antenna element for the broadside beam, while scanning and for the broad beam.

Figure 6.11 shows the active S-parameters of the four individual slots for the three different excitations under consideration. It can be seen that a -10 dB impedance matching is achieved in the band from 29 to 31 GHz.

The simulated radiation patterns of the array for the three different excitations are shown in Fig. 6.12. For the broadside array both E- and H-plane patterns are shown for

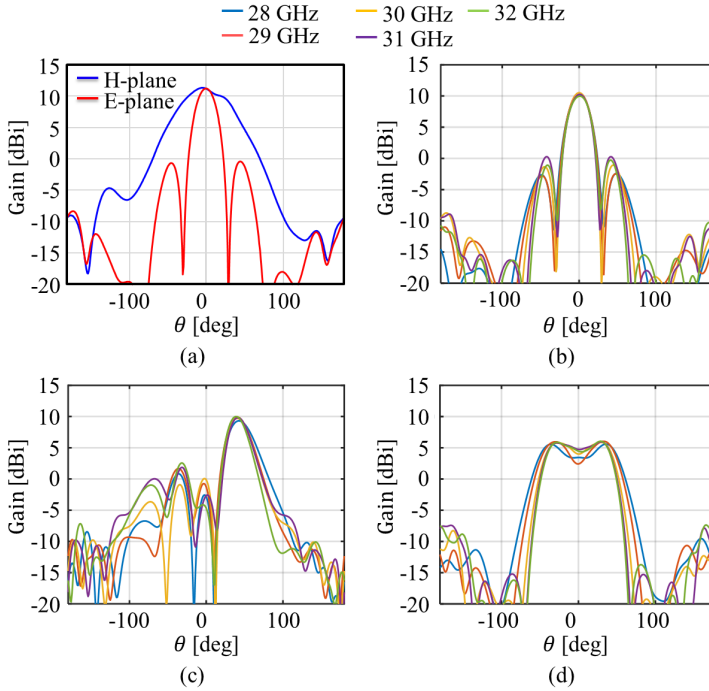


Figure 6.12: Gain of the four element array for (a) broadside scanning at 30 GHz (E- and H-plane), (b) scanning in the broadside direction (E-plane), (c) scanning towards 45° in the E-plane, (d) near field focus in the E-plane.

30 GHz in Fig. 6.12(a), while the E-plane patterns for multiple frequencies are shown in Fig. 6.12(b). The E-plane patterns at different frequencies are reported in Fig. 6.12(c) and (d), for scanning to 45° and for the wide beam case, respectively. It can be observed that the patterns are stable with frequency within the band of investigation. Also, when comparing Fig. 6.12(b) and Fig. 6.12(c) it can be seen that the gain while scanning to 45° is approximately equal to the gain for broadside scanning, as targeted by the design. Figure 6.12(d) shows that the same array can be used to generate a broad pattern when exciting all four slots with a quadratic phase distribution, thus increasing the effective isotropic radiated power compared to exciting a single slot of the array. The feeding network is designed to achieve an amplitude taper of $A = [0.6 \ 1 \ 1 \ 0.6]$ and a phase distribution of $\phi = [0^\circ \ 106^\circ \ 106^\circ \ 0^\circ]$.

6.4. Measurements

A prototype demonstrator has been manufactured for the experimental validation of the design. The three boards for the three different excitation modes are fabricated in standard PCB technology. The photos of the PCB are presented in Figs. 6.13. The artificial dielectric superstrate is fabricated as a separate board and can be attached on top of the three slot arrays.

Top mounted solderless Rosenberger 02K722-40MS3 50 Ω PCB connectors [76] are

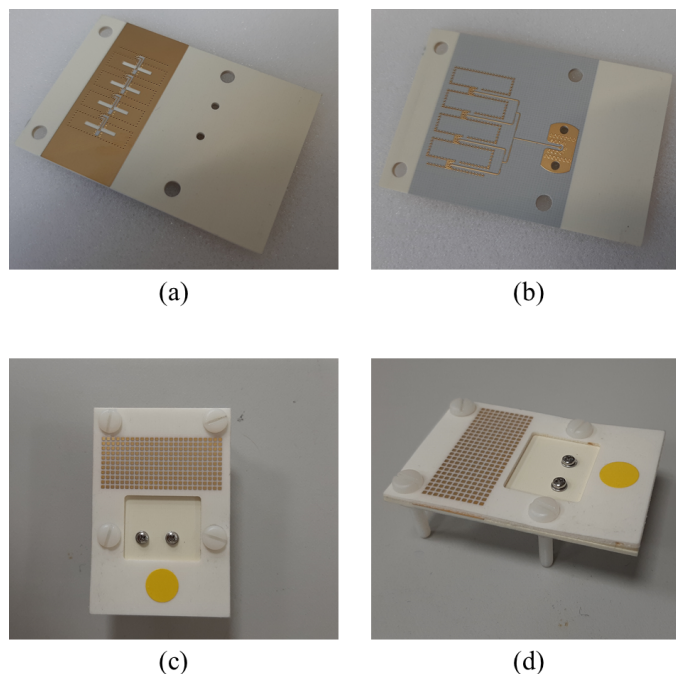


Figure 6.13: Photographs of fabricated demonstrator boards. (a) Top view of array without ADL superstrate. (b) Bottom view of broadside board. (c) Top view of assembled PCBs. (d) Overview of assembled PCBs.

used to connect to the input of the feeding networks. The array and the broadside feeding network can be seen in Figs. 6.13(a) and (b), whereas (c) and (d) show pictures of the assembled boards with the ADL superstrate. A back-to-back version of the feeding network has been also manufactured to assess the losses of the feeding lines.

The measured and simulated reflection coefficient of the three boards are shown in Fig. 6.14. The roughness of the copper is included in the simulation performed in HFSS using the Groiss method [77], with a root mean square roughness of $2.8\ \mu\text{m}$ [78]. The S-parameters from all three boards show a good agreement with simulations. It is worth to note that the reflection coefficients in Fig. 6.14 are lower than the previously presented levels at the slot terminals in Fig. 6.11, because of the added losses of the feeding networks.

Figure 6.15 shows the measured normalized E-plane patterns (co- and cross-polarizations according to the Ludwig 3 definition) for the three excitations for several frequencies. All patterns are normalized to the maximum of broadside array at 30 GHz. It can be seen that the patterns while pointing to the broadside direction (Fig. 6.15(a)) and while scanning to 45° (Fig. 6.15(c)) are stable with frequency, whereas the broad beam (Fig. 6.15(e)) shows more variations. This is in line with the simulated patterns as shown in Fig. 6.12. Also it can be seen that the measured amplitude for the broadside case and while scanning is approximately equal, and the broad beam is around 5 dB lower, again as is expected from simulation (Fig. 6.12). Finally, it can be seen that the cross polarization

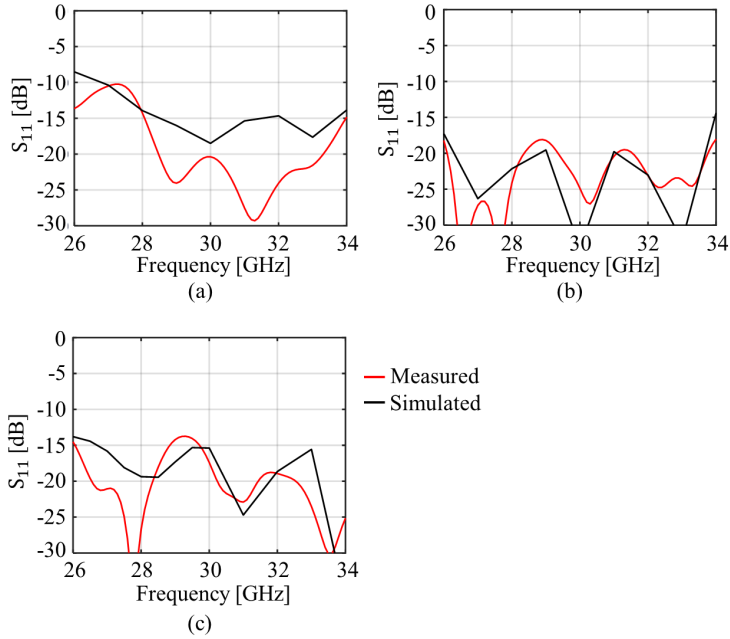


Figure 6.14: Measured S-parameters of the three boards: (a) broadside, (b) scanning and (c) broad beam.

amplitude for all three excitation cases is lower than -20 dB.

A comparison between the normalized patterns from simulation and from the measurements at 30 GHz is shown in Fig. 6.16. A good agreement can be seen for the broadside case, both for the E- and H-plane, and while scanning to 45° . For the broad beam, some discrepancy can be observed between measured and simulated patterns, since the measured beam appears to be slightly narrower and does not exhibit the two-peak characteristics of the simulated pattern.

To explain this difference in the patterns, a tolerance study is performed on several parameters, according to information provided by the manufacturer and from the material datasheets: h_1 is varied from the nominal value in the range $\pm 200 \mu\text{m}$, w is varied $\pm 50 \mu\text{m}$, the amplitudes of the elements ± 2 dB, the phase of the elements $\pm 15^\circ$. Also the dielectric constant of the Rohacell foam is varied from $\epsilon_r = 1$ to 1.2. Figure 6.17 shows several patterns in grey obtained by varying the parameters, compared to the measured pattern in black. It can be seen that the tolerances can explain the discrepancy as the black curve falls within the range of grey patterns.

Figure 6.18(a) reports a comparison between the simulated and measured values of the gain as a function of frequency for the broadside array, showing a good agreement. The losses of the broadside feeding network are shown in Fig. 6.18(b), both from simulations and measurements. The feeding network losses are measured by means of a back-to-back structure as in the inset of the figure and divided by 2 to account only for half of the transition. The oscillatory behavior in the measurement is due to some reflections occurring at the connectors, which is not accounted for in the simulations. It can

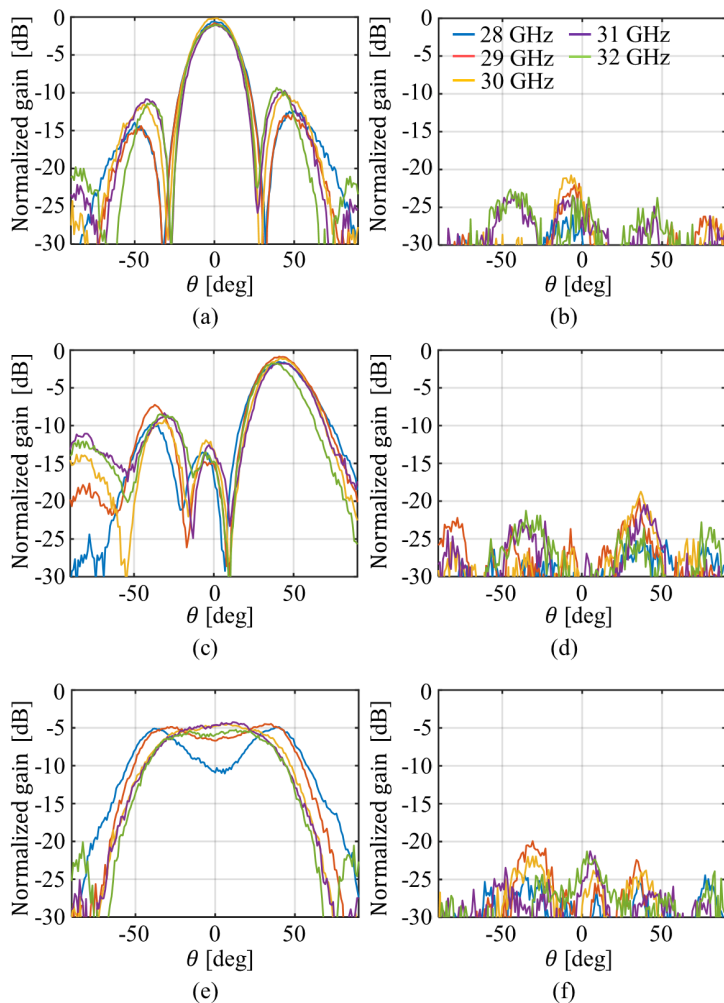


Figure 6.15: Measured, normalized E-plane patterns of the array for several frequencies in broadside direction co- (a) and cross-pol. (b), scanning to 45° co- (c) and cross-pol. (d), and the wide beam co- (e) and cross-pol. (f). All patterns are normalized to the maximum of broadside array at 30GHz.

be seen that approximately 1.3-2.3 dB of losses can be attributed to the feeding network in the band 28-32 GHz.

6.5. Conclusions

We presented a study of planar slot antennas with artificial dielectric superstrates to realize pattern shaping. Based on the analysis of leaky waves propagating along the artificial dielectric slab, the shape of the element pattern can be manipulated to enlarge the beamwidth. When used in array configuration, such an element can achieve reduced

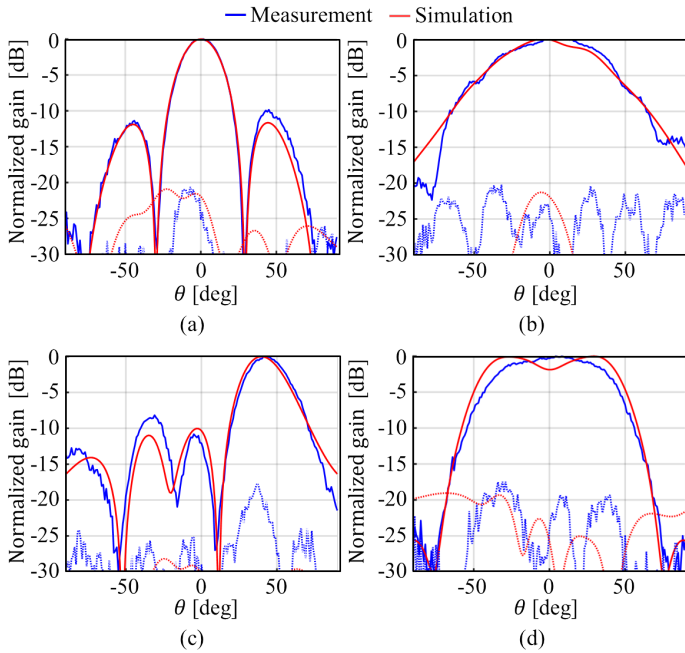


Figure 6.16: Comparison between normalized patterns from HFSS and measurements for the broadside case E- (a) and H-plane (b), E-plane while scanning to 45° (c) and the E-plane for the broad beam (d).

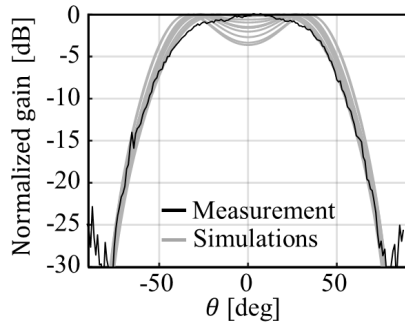


Figure 6.17: Tolerance study on pattern of the broad beam. The considered parameters are: h_1 , w , A , ϵ_r of the foam and the phase distribution along the array.

scan loss. The same array can be used also to radiate a pattern with large beamwidth by employing quadratic phase illumination.

A study was done on the relation between the gain difference between broadside and 45° due to the leaky waves and the mutual coupling between antenna elements within an array. This study led to a trade-off between matching and scan performance. An array design with a stable gain (gain difference ≈ 0 dB) in the scan range $\pm 45^\circ$ was concluded to be a good trade-off between impedance matching and radiation performance.

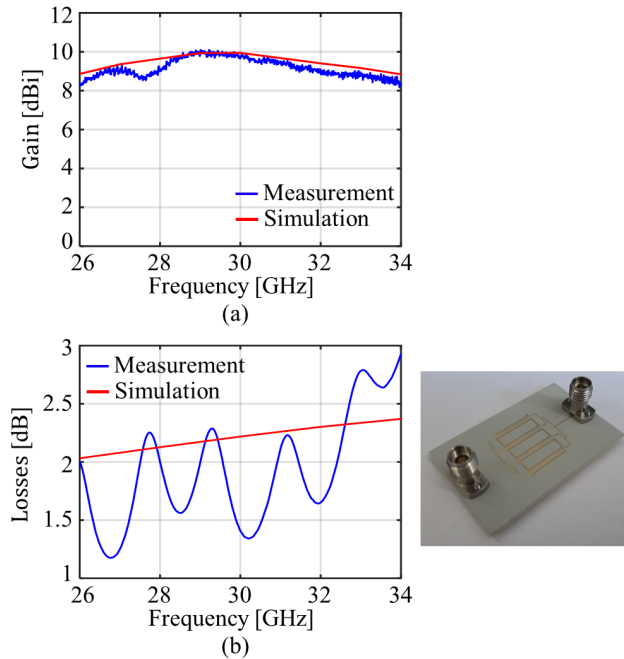


Figure 6.18: (a) Comparison between simulated and measured values of the gain and the realized gain for the broadside array. (b) Measured losses of the broadside feeding network.

A PCB prototype of the array for 30 GHz operation was manufactured and tested. Three arrays were fabricated, with different feeding networks to realize a beam in broadside direction, scanning to 45° and a broad beam. The measured results showed a good agreement with simulations, with a gain variation as a function of scan angle and frequency of less than 1 dB within a $\pm 45^\circ$ field of view and a 28-32 GHz bandwidth.

The proposed array concept has potential to be used in multi-mode mm-wave phased array with electronic control of phase and amplitudes of the elements.

Chapter 7

Conclusions

This dissertation describes the research work carried out over a period of four years (from October 2017 to October 2021) at Delft University of Technology, in Delft, the Netherlands, in the framework of the TTW-NXP partnership program: “Advanced 5G solutions”.

The project focused on an efficient power combiner for 5G communications, specifically in the frequency band around 28 GHz. Moreover, a multimode antenna array with reduced scan losses was designed. The radiating structures, used either as the combiner output or as the array elements, are slots with artificial dielectric layers (ADLs). ADLs can be design with the aim of controlling leaky waves and shaping the radiation pattern for angular filtering and gain enhancement in a given field of view.

Modeling aspects of the antenna elements were also addressed. An efficient method of moments procedure for finite slot antennas in arbitrary stratification is derived using basis functions only at the feeding point and the end points, and an equivalent transmission line model is derived. Also, a theoretical analysis is done on non-periodic and non-square ADLs, resulting in closed-form expressions and an equivalent circuit representation of these ADLs.

In this chapter, we summarize the conclusions and most important results of the research. In addition, an outlook on future research building on the work in this dissertation is discussed.

7.1. Equivalent Circuit Models of Finite Slot Antennas

An efficient method of moments procedure was presented, to accurately find the impedance of semi-infinite and finite slot antennas in arbitrary stratification. The procedure utilizes basis functions only at the feeding points and at the end points of the slot antenna. Therefore, only two basis functions are used for the semi-infinite slot and three for the finite slot. The basis functions were chosen such that they properly account for the reactive energy localized at these points, as well as the radiation emanating from these points. The procedure is validated with full wave simulations, as the input impedance of a finite slot antenna with arbitrary length was found accurately. Although not considered in this thesis, the method of moments derived here has found an important

application in the assessment of finite edge effects in large connected slot arrays [57]. The use of a limited number of basis functions, equal to the number of feeds and slot terminations, enables simulations of large connected array of slots with ADL superstrate. Such simulations would be too computationally demanding for a commercial software.

Based on the numerical spectral domain solution, an equivalent transmission line circuit was derived for the slot, by extracting the pole contribution from the mutual impedance integrals. The pole contribution is associated with a mode launched along the slot, and can be represented as a transmission line. To be able to separate the residue contribution from the space wave, a thin dielectric slab or losses in the metal can be introduced. The radiation is described in the model as resistances located at the feed and at the end points. The model allows representing the radiation from the finite slot as the generation of different space waves, one associated with the feeding gap and two emerging from the end points. The physical dimensions and the shape of the basis functions was accounted for in the circuit by means of transformers. The circuit model can also be used for multiple feeds, providing physical insight in the main mechanism determining the mutual coupling in connected slot arrays. The coupling between two feeds is dominated by waves that propagate along the slot and can be studied by means of equivalent transverse transmission lines connecting the two feeds.

7.2. Closed-Form Analysis of Artificial Dielectrics with Non-Identical or Non-Square Layers

Closed-form expressions for the reactance of ADLs were studied in previous works. More general closed-form expressions for the equivalent layer impedance for generic plane wave incidence were presented in this thesis, to account for non-periodic ADLs in the z -direction. The novel formulation allows the individual layers to be different from each other in terms of geometrical parameters. Also the mutual distance and shift between adjacent layers may vary along the stratification. The analytical formulas were validated by comparison with full wave simulation results. The expressions can be used to design ADLs that are not uniform along the vertical dimension.

Further generalizations are done on the analysis of ADLs, by dropping the requirement of square patches and periods. ADLs with different geometrical parameters in x - and y -directions were studied and closed-form expressions for the layer impedances in an equivalent transmission line model were derived. It is found that the TE and TM modes are no longer decoupled and that the coupling depends on the azimuthal angle of the incident plane wave. Such structures were not used in the designs shown in this thesis. However, non-square ADLs can find applications in the design of antenna superstrates with different properties in the the two main planes. Moreover, the application of these structures for the design of linear-to-linear or linear-to-circular polarization converter will be the object of future investigations.

7.3. Efficient PPW Power Combiner for mm-Waves

An efficient and wideband power combiner in a PPW structure was presented. The PPW is excited at periodically spaced locations in the transverse dimension by signals from

multiple PAs. Due to the periodic excitation, the active impedances of the different ports are nearly equal. Also, the non-resonant nature of the PPW allows for wideband operation, as the active impedances are constant with frequency. To accommodate efficiently the generation of a range of output power, for example for QAM-modulated signals, a Doherty combining scheme is implemented in the PPW combiner. Two sets of parallel feeding points, representing main and peaking sources, separated by a $\lambda/4$ section along the direction of propagation, excite the waveguide according to the Doherty scheme. Based on the required output power of the combiner, the number of inputs connected in parallel can be easily changed.

A design for a 6-to-1 combiner is made and fabricated in standard PCB technology. Measurement results were presented, showing good agreements with simulated results. It was found that in the band from 24 to 32GHz the efficiency of the structure, accounting for both the operating efficiency of the PAs and the impedance mismatch of the combiner, is around 60%.

Moreover, a 6-to-1 Doherty combiner integrated with an antenna was presented. To reduce the size of the structure, the waveguide folds over itself so that the combiner and antenna together fit within $0.5\lambda \times 0.5\lambda$, making it suitable for possible array implementations. The measured S-parameters show a good agreement with simulations, as well as the radiation characteristics of the antenna.

A variation of the PPW combiner concept was proposed for the integration with an active circuit containing the PAs. The slot is made to have a meandering shape, so that the output pads from the IC could be all on a line. The active impedance of the different feeding points is optimized for the optimal operating conditions of the PAs. A PCB was designed, where the combiner has either a connector as output, or a cavity backed slot antenna.

7.4. Phased Array with Pattern Shaping and Scan Loss Reduction for mm-Waves

A study of planar slot antennas with artificial dielectric superstrates to realize pattern shaping was presented. The shape of the element pattern can be manipulated to enlarge the beamwidth using leaky waves propagating in the cavity between the slot plane and the ADLs. When used in array configuration, this type of pattern shaping can achieve reduced scan loss. The same array can be used also to radiate a pattern with large beamwidth and to implement angular filtering, by employing quadratic phase illumination.

The relation between the gain difference between broadside and 45° and the mutual coupling between antenna elements was studied. It was concluded that a trade-off exists between matching and scan performance. An array design with a stable gain (gain difference ≈ 0 dB) in the scan range $\pm 45^\circ$ was found to be a good trade-off between impedance matching and radiation performance.

A PCB demonstrator of an array of cavity backed slots in the presence of an ADL superstrate was manufactured to operate in a band around 30 GHz. Three arrays were fabricated, with different feeding networks to realize a beam in broadside direction, scanning to 45° and a broad beam. The S-parameters and the radiation characteristics of the arrays were measured, and the measured results showed a good agreement with simu-

lations, with a gain variation as a function of scan angle and frequency of less than 1 dB within a $\pm 45^\circ$ field of view and a 28-32 GHz bandwidth.

7.5. Future Outlook

Two design topics and two theoretical topics were discussed in this dissertation. The concept of the Doherty PPW combiner and the array with pattern shaping and scan loss reduction were validated with measurements. Possible future research directions that could build upon this work are listed below:

- The demonstrator of the integration between the active components and the PPW combiner is still being fabricated. Once the demonstrator is manufactured, it should be tested, with the goal to achieve output power levels in the order of 1 watt.
- An antenna element including the PPW combiner is proposed to facilitate phased array application with $\lambda/2$ spacing. Additional engineering challenges exist still in the impact of the IC including its feeding structure and the heat dissipation in such a dense array configuration.
- The possibilities of independent E- and H-plane pattern optimization using non-square ADLs can be further investigated. The extra degree of freedom provided by this type of superstrate could improve antenna designs where strict requirements exist on the pattern in one of the two principle planes. Moreover, the design of polarizers could exploit the general formulas accounting for non-equal and non-square layers.
- The proposed ADL superstrate for pattern shaping and scan loss reduction can be implemented in-package. The smaller fabrication resolution in this technology compared to PCB allows for utilizing the concepts also for applications at higher operating frequencies. Also scaling to larger arrays is interesting for applications where a higher directivity is required.

7.6. Impact of the Research

The work described in this thesis has led to a number of journal and conference publications (listed on p. 127 of this dissertation).

The theoretical works from Ch. 2 and 3 are customarily used within the Terahertz Sensing group at TU Delft in the design of wideband connected arrays and the analysis of finite edge effects.

Moreover, the work described in Ch. 2 was nominated for the *best student paper award* at the 13th European Conference on Antennas and Propagation (EuCAP) in Krakow, Poland, and it was awarded with an *Honourable Mention* in the *best student paper award* competition at the 2019 IEEE Antennas and Propagation Society International Symposium (APS) in Atlanta, Georgia, USA.

Appendix A

Derivations of Equivalent Circuit for Non-square ADL

The closed-form expressions and the equivalent transmission circuit for ADLs with non-square patches are derived from the equivalent magnetic currents on the layers.

A.1. Single Layer

We consider the unit cell of a single ADL as shown in Fig. 3.10. As described in [24], an integral equation can be set up, where the unknown is the magnetic current distribution on the slot region of the unit cell as

$$\mathbf{m}_0(\boldsymbol{\rho}) * \mathbf{g}(\boldsymbol{\rho}) = \int_{-\infty}^{\infty} \int_{-\infty}^{\infty} \mathbf{g}(\boldsymbol{\rho} - \boldsymbol{\rho}') \cdot \mathbf{m}_0(\boldsymbol{\rho}') d\boldsymbol{\rho}' = \mathbf{h}_{inc}(\boldsymbol{\rho}). \quad (\text{A.1})$$

\mathbf{m}_0 is the magnetic current distribution on the slots, \mathbf{g} is the dyadic Green's function, which is related to the free space Green's function as $\mathbf{g} = 4\mathbf{g}_{fs}$, where \mathbf{g}_{fs} represents the magnetic field radiated by an elementary magnetic current source in free space. $d\boldsymbol{\rho}'$ refers to $dx'dy'$. The incident field \mathbf{h}_{inc} represents the incident magnetic field in absence of the magnetic current. It is related to the direct magnetic field of a plane wave incident on the ADL \mathbf{h}_{dir} as $\mathbf{h}_{inc} = 2\mathbf{h}_{dir}$.

A.1.1. Basis Functions

The total magnetic current of a layer can be written as a sum of four terms:

$$\mathbf{m}_0(\boldsymbol{\rho}) = \sum_{p=1}^4 a_p \mathbf{f}_p(\boldsymbol{\rho}) \quad (\text{A.2})$$

where $\mathbf{f}_p(\boldsymbol{\rho})$ are basis functions

$$\mathbf{f}_1(\boldsymbol{\rho}) = \sqrt{\frac{d_y}{d_x}} e^{-jk_{x0}x} \frac{1}{w_x} \text{rect}_{[-w_x/2, w_x/2]}(y) \hat{\mathbf{x}} \quad (\text{A.3})$$

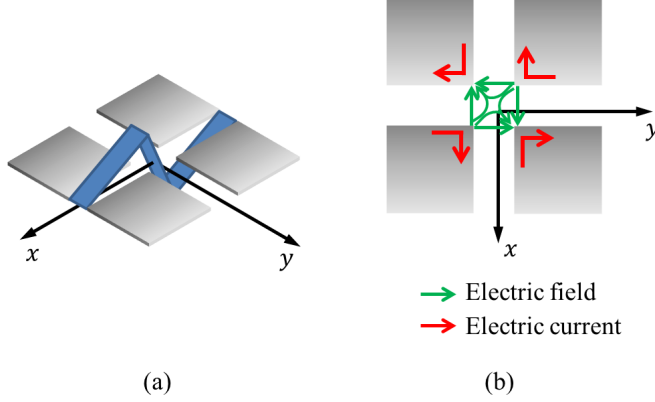


Figure A.1: (a) Illustration of the uniform transverse distribution with anti-symmetric shape in the longitudinal direction, \mathbf{f}_3 (\mathbf{f}_4 is along y). (b) Electric field and currents at the junction.

$$\mathbf{f}_2(\boldsymbol{\rho}) = \sqrt{\frac{d_x}{d_y}} e^{-jk_y y} \frac{1}{w_y} \text{rect}_{[-w_y/2, w_y/2]}(x) \hat{\mathbf{y}} \quad (\text{A.4})$$

$$\mathbf{f}_3(\boldsymbol{\rho}) = b_{d,x}(x) \frac{1}{w_x} \text{rect}_{w_x}(y) \hat{\mathbf{x}} \quad (\text{A.5})$$

and

$$\mathbf{f}_4(\boldsymbol{\rho}) = b_{d,y}(y) \frac{1}{w_y} \text{rect}_{w_y}(x) \hat{\mathbf{y}}. \quad (\text{A.6})$$

The first two functions, \mathbf{f}_1 and \mathbf{f}_2 , represent linearly progressive phase terms that account for the oblique angle of incidence along the slots between the patches. In the transverse direction a uniform amplitude is assumed, $\text{rect}_{[-w_i/2, w_i/2]}(\xi) = 1$ for $-w_i/2 \leq \xi \leq w_i/2$ and 0 elsewhere, where the subscript i denotes either x or y . The effect of the junctions (i.e. the crossing of the x - and y -oriented slots) are accounted for in \mathbf{f}_3 and \mathbf{f}_4 , that represent an anti-symmetric profile as illustrated in Fig. A.1(a). These currents are zero at the edges of the unit cell and in the center, and are consistent with the electric field and electric current distributions at the crossing, as shown in Fig. Fig. A.1(b). The longitudinal, anti-symmetric distribution along x is expressed as

$$b_{d,x}(x) = -\left(e^{jk_0 x} + \Gamma_x e^{-jk_0 x}\right) \text{rect}_{[-d_x/2, -w_x/2]}(x) + \left(e^{-jk_0 x} + \Gamma_x e^{jk_0 x}\right) \text{rect}_{[w_x/2, d_x/2]}(x) + C_x x \text{rect}_{[-w_x/2, w_x/2]}(x) \quad (\text{A.7})$$

where $C_x = (2/w_x)(e^{-jk_0 w_x/2} + \Gamma_x e^{jk_0 w_x/2})$ and $\Gamma_x = e^{-jk_0 d_x}$ is the reflection coefficient at the edges of the unit cell. Similarly, $b_{d,y}(y)$ can be found by replacing x with y .

By applying a Galerkin projection on the integral equation in (A.1) the ADL can be represented by means of a 4×4 admittance matrix, $\bar{\bar{\mathbf{Y}}}$. The entries of the admittance matrix are found in the spectral domain as

$$Y_{qp} = \frac{-1}{d_x d_y} \sum_{m_x} \sum_{m_y} \mathbf{F}_p(k_{xm}, k_{ym}) \cdot \mathbf{G}(k_{xm}, k_{ym}) \mathbf{F}_q^*(-k_{xm}, -k_{ym}) \quad (\text{A.8})$$

where the subscripts p and q refer to 1, 2, 3 or 4. \mathbf{F}_p and \mathbf{F}_q are the basis and test functions respectively, and are the Fourier transforms of (A.3) - (A.6):

$$\mathbf{F}_1(k_{xm}, k_{ym}) = \sqrt{d_x d_y} \delta(m_x) \text{sinc}(k_{ym} w_x / 2) \hat{\mathbf{x}} \quad (\text{A.9})$$

$$\mathbf{F}_2(k_{xm}, k_{ym}) = \sqrt{d_x d_y} \delta(m_y) \text{sinc}(k_{xm} w_y / 2) \hat{\mathbf{y}} \quad (\text{A.10})$$

$$\mathbf{F}_3(k_{xm}, k_{ym}) = B_{d,x}(k_{xm}) \text{sinc}(k_{ym} w_x / 2) \hat{\mathbf{x}} \quad (\text{A.11})$$

and

$$\mathbf{F}_4(k_{xm}, k_{ym}) = B_{d,y}(k_{xm}) \text{sinc}(k_{xm} w_y / 2) \hat{\mathbf{y}} \quad (\text{A.12})$$

$k_{xm} = k_{x0} - 2\pi m_x / d_x$ and $k_{ym} = k_{y0} - 2\pi m_y / d_y$ are the Floquet wavenumbers. \mathbf{G} is the Fourier transform of \mathbf{g} and $B_{d,x}$ and $B_{d,y}$ are the Fourier transforms of $b_{d,x}$ and $b_{d,y}$ and are given in Eq. (39) in [24]. $\delta(\cdot)$ is the Kronecker delta-function.

A.1.2. Reduced Admittance Matrix

We can write a system of equations

$$\begin{aligned} a_1 Y_{11} + a_2 Y_{12} + a_3 Y_{13} + a_4 Y_{14} &= i_1 \\ a_1 Y_{21} + a_2 Y_{22} + a_3 Y_{23} + a_4 Y_{24} &= i_2 \\ a_1 Y_{31} + a_2 Y_{32} + a_3 Y_{33} + a_4 Y_{34} &= i_3 \\ a_1 Y_{41} + a_2 Y_{42} + a_3 Y_{43} + a_4 Y_{44} &= i_4 \end{aligned} \quad (\text{A.13})$$

where $i_q = \langle 2\mathbf{h}_{inc}, \mathbf{f}_q \rangle$. The reaction operator has been introduced, defined as:

$$\langle f_1, f_2 \rangle = \int_{-\infty}^{\infty} \int_{-\infty}^{\infty} f_1(x, y) f_2^*(x, y) dx dy. \quad (\text{A.14})$$

A number of considerations can be made to allow the derivation of the solution in a closed form and provide physical insight. For sub-wavelength array periods, the projections of the plane wave onto the anti-symmetric profile functions can be neglected, since the positive and negative parts of these odd functions result in equal and opposite contributions and cancel out. This is equivalent to assuming that $i_3 \approx i_4 \approx 0$ and $Y_{13} \approx Y_{31} \approx Y_{24} \approx Y_{42} \approx 0$. Solving (A.13) for a_3 and a_4 gives:

$$\begin{aligned} a_3 &= -a_2 \frac{Y_{32} Y_{44}}{Y_{33} Y_{44} - Y_{34} Y_{43}} + a_1 \frac{Y_{41} Y_{34}}{Y_{33} Y_{44} - Y_{34} Y_{43}} \\ a_4 &= -a_1 \frac{Y_{41} Y_{33}}{Y_{33} Y_{44} - Y_{34} Y_{43}} + a_2 \frac{Y_{32} Y_{43}}{Y_{33} Y_{44} - Y_{34} Y_{43}} \end{aligned} \quad (\text{A.15})$$

which can be substituted back into (A.13), resulting two linear equations, rather than four:

$$\begin{aligned} a_1 \left(Y_{11} - \frac{Y_{41} Y_{33} Y_{14}}{Y_{33} Y_{44} - Y_{34} Y_{43}} \right) + a_2 \left(Y_{12} + \frac{Y_{32} Y_{43} Y_{14}}{Y_{33} Y_{44} - Y_{34} Y_{43}} \right) &= i_1 \\ a_1 \left(Y_{21} + \frac{Y_{41} Y_{34} Y_{23}}{Y_{33} Y_{44} - Y_{34} Y_{43}} \right) + a_2 \left(Y_{22} - \frac{Y_{32} Y_{44} Y_{23}}{Y_{33} Y_{44} - Y_{34} Y_{43}} \right) &= i_2. \end{aligned} \quad (\text{A.16})$$

This results in a reduced admittance matrix

$$\overline{\overline{\mathbf{Y}}}_r = \begin{bmatrix} Y_{11} - \frac{Y_{41} Y_{33} Y_{14}}{Y_{33} Y_{44} - Y_{34} Y_{43}} & Y_{12} + \frac{Y_{32} Y_{43} Y_{14}}{Y_{33} Y_{44} - Y_{34} Y_{43}} \\ Y_{21} + \frac{Y_{41} Y_{34} Y_{23}}{Y_{33} Y_{44} - Y_{34} Y_{43}} & Y_{22} - \frac{Y_{32} Y_{44} Y_{23}}{Y_{33} Y_{44} - Y_{34} Y_{43}} \end{bmatrix} \quad (\text{A.17})$$

which satisfies the relation

$$\overline{\overline{\mathbf{Y}}}_r \begin{pmatrix} a_1 \\ a_2 \end{pmatrix} = \begin{pmatrix} i_1 \\ i_2 \end{pmatrix}. \quad (\text{A.18})$$

A.1.3. Admittance Matrix Entries

The entries of the admittance matrix are found using (A.8).

Solution of Y_{11} and Y_{22}

We first consider Y_{11}

$$Y_{11} = \frac{-1}{d_x d_y} \sum_{m_x} \sum_{m_y} \mathbf{F}_1(k_{xm}, k_{ym}) \cdot \mathbf{G}(k_{xm}, k_{ym}) \mathbf{F}_1^*(-k_{xm}, -k_{ym}). \quad (\text{A.19})$$

We substitute (A.9) in this equation

$$Y_{11} = \frac{-1}{d_x d_y} \sum_{m_x} \sum_{m_y} \sqrt{d_x d_y} \delta(m_x) \text{sinc}(k_{ym} w_x / 2) \hat{\mathbf{x}} \cdot \mathbf{G}(k_{xm}, k_{ym}) \sqrt{d_x d_y} \delta(m_x) \text{sinc}(k_{ym} w_x / 2) \hat{\mathbf{x}} \quad (\text{A.20})$$

where we used the symmetric shape of the sinc-function. Using the property of the δ -function and simplifying the terms with d_x and d_y

$$Y_{11} = - \sum_{m_y} \text{sinc}^2(k_{ym} w_x / 2) G_{xx}(k_{x0}, k_{ym}). \quad (\text{A.21})$$

Substituting the xx -component of the Green's function

$$Y_{11} = - \sum_{m_y} \text{sinc}^2(k_{ym} w_x / 2) \left(- \frac{2}{k_0 \zeta_0} \frac{k_0^2 - k_{x0}^2}{\sqrt{k_0^2 - k_{x0}^2 - k_{ym}^2}} \right). \quad (\text{A.22})$$

We now separate the fundamental and the higher order Floquet modes

$$Y_{11} = \frac{2}{k_0 \zeta_0} \left(\text{sinc}^2(k_{y0} w_x / 2) \left(\frac{k_0^2 - k_{x0}^2}{\sqrt{k_0^2 - k_{x0}^2 - k_{y0}^2}} \right) + \sum_{m_y \neq 0} \text{sinc}^2(k_{ym} w_x / 2) \left(\frac{k_0^2 - k_{x0}^2}{\sqrt{k_0^2 - k_{x0}^2 - k_{ym}^2}} \right) \right). \quad (\text{A.23})$$

For narrow slots we can approximate $\text{sinc}^2(k_{y0} w_x / 2) \approx 1$. For the fundamental mode we can write $k_{x0} = k_0 \sin \theta \cos \phi$, $k_{y0} = k_0 \sin \theta \sin \phi$ and $\sqrt{k_0^2 - k_{x0}^2 - k_{y0}^2} = k_{z0} = k_0 \cos \theta$. Also, for higher order Floquet modes we can approximate

$$\sqrt{k_0^2 - k_{x0}^2 - k_{ym}^2} \approx -j |k_{ym}| \approx -j \left| - \frac{2\pi m_y}{d_y} \right| \quad (\text{A.24})$$

so that

$$Y_{11} = \frac{2}{k_0 \zeta_0} \left(\left(\frac{k_0^2 - k_0^2 \sin^2 \theta \cos^2 \phi}{k_0 \cos \theta} \right) + \sum_{m_y \neq 0} \operatorname{sinc}^2 \left(-\frac{\pi m_y w_x}{d_y} \right) \left(\frac{k_0^2 - k_0^2 \sin^2 \theta \cos^2 \phi}{-j \left| -\frac{2\pi m_y}{d_y} \right|} \right) \right). \quad (\text{A.25})$$

Rewriting with some simplifications results in

$$Y_{11} = (1 - \sin^2 \theta \cos^2 \phi) \left(\frac{2}{\zeta_0} \frac{1}{\cos \theta} + j \frac{d_y k_0}{\pi \zeta_0} \sum_{m_y \neq 0} \frac{\operatorname{sinc}^2(\pi m_y w_x / d_y)}{|m_y|} \right). \quad (\text{A.26})$$

By defining B_x as the imaginary part of the admittance, i.e.

$$B_x = \frac{d_y k_0}{\pi \zeta_0} \sum_{m_y \neq 0} \frac{\operatorname{sinc}^2(\pi m_y w_x / d_y)}{|m_y|} \quad (\text{A.27})$$

we find

$$Y_{11} = (1 - \sin^2 \theta \cos^2 \phi) \left(\frac{2}{\zeta_0} \frac{1}{\cos \theta} + j B_x \right). \quad (\text{A.28})$$

Similarly Y_{22} is found to be:

$$Y_{22} = (1 - \sin^2 \theta \sin^2 \phi) \left(\frac{2}{\zeta_0} \frac{1}{\cos \theta} + j B_y \right). \quad (\text{A.29})$$

where

$$B_y = \frac{d_x k_0}{\pi \zeta_0} \sum_{m_x \neq 0} \frac{\operatorname{sinc}^2(\pi m_x w_y / d_x)}{|m_x|} \quad (\text{A.30})$$

Solution of Y_{21} and Y_{12}

The mutual impedance between the phase progressive basis functions is found as

$$Y_{21} = \frac{-1}{d_x d_y} \sum_{m_x} \sum_{m_y} \mathbf{F}_1(k_{xm}, k_{ym}) \cdot \mathbf{G}(k_{xm}, k_{ym}) \mathbf{F}_2^*(-k_{xm}, -k_{ym}). \quad (\text{A.31})$$

We substitute (A.9) and (A.10) in this equation, so that

$$Y_{21} = \frac{-1}{d_x d_y} \sum_{m_x} \sum_{m_y} \sqrt{d_x d_y} \delta(m_x) \operatorname{sinc}(k_{ym} w_x / 2) \hat{\mathbf{x}} \cdot \mathbf{G}(k_{xm}, k_{ym}) \sqrt{d_x d_y} \delta(m_y) \operatorname{sinc}(k_{xm} w_y / 2) \hat{\mathbf{y}}. \quad (\text{A.32})$$

Using the property of the δ -function and simplifying we find

$$Y_{21} = -\operatorname{sinc}(k_{y0} w_x / 2) G_{yx}(k_{x0}, k_{y0}) \operatorname{sinc}(k_{x0} w_y / 2). \quad (\text{A.33})$$

For narrow slots we can approximate $\operatorname{sinc}^2(k_{y0} w_x / 2) \approx \operatorname{sinc}^2(k_{x0} w_y / 2) \approx 1$.

$$Y_{21} = -G_{yx}(k_{x0}, k_{y0}). \quad (\text{A.34})$$

Substituting the Green's function and writing $k_{x0} = k_0 \sin \theta \cos \phi$, $k_{y0} = k_0 \sin \theta \sin \phi$ and $\sqrt{k_0^2 - k_{x0}^2 - k_{y0}^2} = k_{z0} = k_0 \cos \theta$ we find

$$Y_{21} = -\frac{2}{\zeta_0} \frac{\sin^2 \theta \cos \phi \sin \phi}{\cos \theta}. \quad (\text{A.35})$$

Similarly

$$Y_{12} = -\frac{2}{\zeta_0} \frac{\sin^2 \theta \cos \phi \sin \phi}{\cos \theta}. \quad (\text{A.36})$$

Solution of Y_{41} , Y_{14} , Y_{32} and Y_{23}

Again, substituting (A.9) and (A.12) in (A.8) and using the property of the δ -function, we find

$$Y_{41} = \frac{-1}{\sqrt{d_x d_y}} \sum_{m_y} \text{sinc}(k_{ym} w_x / 2) G_{xy}(k_{x0}, k_{ym}) B_{d,y}^*(-k_{ym}) \text{sinc}(k_{x0} w_y / 2). \quad (\text{A.37})$$

For narrow slots we can approximate $\text{sinc}^2(k_{x0} w_y / 2) \approx 1$ and $B_{d,y}^*(-k_{y0}) \approx 0$, so that

$$Y_{41} = \frac{-1}{\sqrt{d_x d_y}} \sum_{m_y \neq 0} \text{sinc}(k_{ym} w_x / 2) G_{xy}(k_{x0}, k_{ym}) B_{d,y}^*(-k_{ym}) \quad (\text{A.38})$$

where we substitute the Green's function

$$Y_{41} = \frac{-1}{\sqrt{d_x d_y}} \sum_{m_y \neq 0} \text{sinc}(k_{ym} w_x / 2) \frac{2}{k_0 \zeta_0} \frac{k_{x0} k_{ym}}{\sqrt{k_0^2 - k_{x0}^2 - k_{ym}^2}} B_{d,y}^*(-k_{ym}). \quad (\text{A.39})$$

Using $\sqrt{k_0^2 - k_{x0}^2 - k_{ym}^2} \approx -j|k_{ym}|$, we find

$$Y_{41} = \frac{-1}{\sqrt{d_x d_y}} \frac{2}{k_0 \zeta_0} \sum_{m_y \neq 0} \text{sinc}(k_{ym} w_x / 2) \frac{k_{x0} k_{ym}}{-j|k_{ym}|} B_{d,y}^*(-k_{ym}). \quad (\text{A.40})$$

Writing again $k_{x0} = k_0 \sin \theta \cos \phi$

$$Y_{41} = \frac{-j}{\sqrt{d_x d_y}} \frac{2}{k_0 \zeta_0} \sum_{m_y \neq 0} \text{sinc}(k_{ym} w_x / 2) k_0 \sin \theta \cos \phi \text{sgn}(k_{ym}) B_{d,y}^*(-k_{ym}) \quad (\text{A.41})$$

which can be rewritten as

$$Y_{41} = \frac{-j}{\sqrt{d_x d_y}} \frac{2 \sin \theta \cos \phi}{\zeta_0} \sum_{m_y \neq 0} \text{sinc}(k_{ym} w_x / 2) \text{sgn}(k_{ym}) B_{d,y}^*(-k_{ym}) \quad (\text{A.42})$$

Following the same steps for Y_{14} , Y_{32} and Y_{23} we find

$$Y_{14} = \frac{-j}{\sqrt{d_x d_y}} \frac{2 \sin \theta \cos \phi}{\zeta_0} \sum_{m_y \neq 0} \text{sinc}(k_{ym} w_x / 2) \text{sgn}(k_{ym}) B_{d,y}(k_{ym}) \quad (\text{A.43})$$

$$Y_{32} = \frac{-j}{\sqrt{d_x d_y}} \frac{2 \sin \theta \sin \phi}{\zeta_0} \sum_{m_x \neq 0} \text{sinc}(k_{xm} w_y / 2) \text{sgn}(k_{xm}) B_{d,x}^*(-k_{xm}) \quad (\text{A.44})$$

and

$$Y_{23} = \frac{-j}{\sqrt{d_x d_y}} \frac{2 \sin \theta \sin \phi}{\zeta_0} \sum_{m_x \neq 0} \text{sinc}(k_{xm} w_y / 2) \text{sgn}(k_{xm}) B_{d,x}(k_{xm}). \quad (\text{A.45})$$

Looking at the expressions for Y_{41} , Y_{14} , Y_{32} and Y_{23} , we can define

$$\tilde{Y}_x = \frac{-j}{\sqrt{d_x d_y}} \frac{2}{\zeta_0} \sum_{m_x \neq 0} \text{sinc}(k_{xm} w_y / 2) \text{sgn}(k_{xm}) B_{d,x}(k_{xm}) \quad (\text{A.46})$$

and

$$\tilde{Y}_y = \frac{-j}{\sqrt{d_x d_y}} \frac{2}{\zeta_0} \sum_{m_y \neq 0} \text{sinc}(k_{ym} w_x / 2) \text{sgn}(k_{ym}) B_{d,y}(k_{ym}). \quad (\text{A.47})$$

Since the functions $B_{d,x}(k_{xm})$ and $B_{d,y}(k_{ym})$ are anti-symmetric, we know that $B_{d,x}(k_{xm}) = -B_{d,x}(-k_{xm})$ and $B_{d,y}(k_{ym}) = -B_{d,y}(-k_{ym})$, so that

$$\tilde{Y}_x^* = \frac{-j}{\sqrt{d_x d_y}} \frac{2}{\zeta_0} \sum_{m_x \neq 0} \text{sinc}(k_{xm} w_y / 2) \text{sgn}(k_{xm}) B_{d,x}^*(k_{xm}) \quad (\text{A.48})$$

and

$$\tilde{Y}_y^* = \frac{-j}{\sqrt{d_x d_y}} \frac{2}{\zeta_0} \sum_{m_y \neq 0} \text{sinc}(k_{ym} w_x / 2) \text{sgn}(k_{ym}) B_{d,y}^*(k_{ym}). \quad (\text{A.49})$$

Allowing us to write the more compact expressions

$$Y_{41} = \sin \theta \cos \phi \tilde{Y}_y^* \quad (\text{A.50})$$

Following the same steps for Y_{14} , Y_{32} and Y_{23} we find

$$Y_{14} = \sin \theta \cos \phi \tilde{Y}_y \quad (\text{A.51})$$

$$Y_{32} = \sin \theta \sin \phi \tilde{Y}_x^* \quad (\text{A.52})$$

and

$$Y_{23} = \sin \theta \sin \phi \tilde{Y}_x. \quad (\text{A.53})$$

Solution of Y_{33} and Y_{44}

Substituting (A.11) in (A.8), we find

$$Y_{33} = \frac{-1}{d_x d_y} \sum_{m_x} \sum_{m_y} B_{d,x}(k_{xm}) \text{sinc}^2(k_{ym} w_x / 2) G_{xx}(k_{xm}, k_{ym}) B_{d,x}^*(-k_{xm}). \quad (\text{A.54})$$

For narrow slots we can approximate $\text{sinc}^2(k_{y0} w_x / 2) \approx 1$ and $B_{d,x}(k_{x0}) \approx 0$. We also separate the fundamental mode in y from the higher order modes, so that

$$Y_{33} = \frac{-1}{d_x d_y} \sum_{m_x \neq 0} \left(B_{d,x}(k_{xm}) G_{xx}(k_{xm}, k_{y0}) B_{d,x}^*(-k_{xm}) \right. \\ \left. + \sum_{m_y \neq 0} B_{d,x}(k_{xm}) \text{sinc}^2(k_{ym} w_x / 2) G_{xx}(k_{xm}, k_{ym}) B_{d,x}^*(-k_{xm}) \right). \quad (\text{A.55})$$

Using the property $B_{d,x}(k_{xm})B_{d,x}^*(-k_{xm}) = -|B_{d,x}(k_{xm})|^2$ and substituting the Green's function, we find

$$Y_{33} = \frac{1}{d_x d_y} \sum_{m_x \neq 0} \left(|B_{d,x}(k_{xm})|^2 \left(\frac{-2}{k_0 \zeta_0} \frac{k_0^2 - k_{xm}^2}{\sqrt{k_0^2 - k_{xm}^2 - k_{y0}^2}} \right) + \sum_{m_y \neq 0} |B_{d,x}(k_{xm})|^2 \text{sinc}^2(k_{ym} w_x / 2) \left(\frac{-2}{k_0 \zeta_0} \frac{k_0^2 - k_{xm}^2}{\sqrt{k_0^2 - k_{xm}^2 - k_{ym}^2}} \right) \right). \quad (\text{A.56})$$

We make the approximations that are valid for higher order Floquet modes $\sqrt{k_0^2 - k_{xm}^2 - k_{y0}^2} \approx -j|k_{xm}|$ and $k_0^2 - k_{xm}^2 \approx -k_{xm}^2$, so that

$$Y_{33} = \frac{1}{d_x d_y} \frac{-2}{k_0 \zeta_0} \sum_{m_x \neq 0} \left(j |B_{d,x}(k_{xm})|^2 \frac{k_{xm}^2}{|k_{xm}|} + \sum_{m_y \neq 0} |B_{d,x}(k_{xm})|^2 \text{sinc}^2(k_{ym} w_x / 2) \frac{k_{xm}^2}{\sqrt{k_0^2 - k_{xm}^2 - k_{ym}^2}} \right). \quad (\text{A.57})$$

Similarly

$$Y_{44} = \frac{1}{d_x d_y} \frac{-2}{k_0 \zeta_0} \sum_{m_y \neq 0} \left(j |B_{d,y}(k_{ym})|^2 \frac{k_{ym}^2}{|k_{ym}|} + \sum_{m_x \neq 0} |B_{d,y}(k_{ym})|^2 \text{sinc}^2(k_{xm} w_y / 2) \frac{k_{ym}^2}{\sqrt{k_0^2 - k_{xm}^2 - k_{ym}^2}} \right). \quad (\text{A.58})$$

Solution of Y_{43} and Y_{34}

Finally, for the last terms we substitute (A.11) and (A.12) in (A.8), we find

$$Y_{43} = \frac{-1}{d_x d_y} \sum_{m_x} \sum_{m_y} B_{d,x}(k_{xm}) \text{sinc}(k_{ym} w_x / 2) G_{xy}(k_{xm}, k_{ym}) B_{d,y}^*(-k_{ym}) \text{sinc}(k_{xm} w_y / 2). \quad (\text{A.59})$$

Again, making the approximations $B_{d,x}(k_{x0}) \approx 0$ and $B_{d,y}(k_{y0}) \approx 0$, and substituting the Green's function

$$Y_{43} = \frac{-1}{d_x d_y} \sum_{m_x \neq 0} \sum_{m_y \neq 0} B_{d,x}(k_{xm}) \text{sinc}(k_{ym} w_x / 2) B_{d,y}^*(-k_{ym}) \text{sinc}(k_{xm} w_y / 2) \frac{2}{k_0 \zeta_0} \frac{k_{xm} k_{ym}}{\sqrt{k_0^2 - k_{xm}^2 - k_{ym}^2}}. \quad (\text{A.60})$$

Reorganizing the terms we find:

$$Y_{43} = \frac{-1}{d_x d_y} \frac{2}{k_0 \zeta_0} \sum_{m_x \neq 0} \sum_{m_y \neq 0} B_{d,x}(k_{xm}) B_{d,y}^*(-k_{ym}) \operatorname{sinc}(k_{ym} w_x / 2) \operatorname{sinc}(k_{xm} w_y / 2) \frac{k_{xm} k_{ym}}{\sqrt{k_0^2 - k_{xm}^2 - k_{ym}^2}}. \quad (\text{A.61})$$

Similarly

$$Y_{34} = \frac{-1}{d_x d_y} \frac{2}{k_0 \zeta_0} \sum_{m_x \neq 0} \sum_{m_y \neq 0} B_{d,y}(k_{ym}) B_{d,x}^*(-k_{xm}) \operatorname{sinc}(k_{ym} w_x / 2) \operatorname{sinc}(k_{xm} w_y / 2) \frac{k_{xm} k_{ym}}{\sqrt{k_0^2 - k_{xm}^2 - k_{ym}^2}}. \quad (\text{A.62})$$

A.1.4. Equivalent Circuit Representation

All entries of the reduced admittance matrix from (A.17) are now known, and we can take another look at this expression. First we split the matrix in two parts, one related only to the progressive phase basis functions, and the second containing all the terms with the anti-symmetric basis functions:

$$\overline{\overline{\mathbf{Y}}}_r = \begin{bmatrix} Y_{11} & Y_{12} \\ Y_{21} & Y_{22} \end{bmatrix} + \begin{bmatrix} -\frac{Y_{41} Y_{33} Y_{14}}{Y_{33} Y_{44} - Y_{34} Y_{43}} & \frac{Y_{32} Y_{43} Y_{14}}{Y_{33} Y_{44} - Y_{34} Y_{43}} \\ \frac{Y_{41} Y_{34} Y_{23}}{Y_{33} Y_{44} - Y_{34} Y_{43}} & -\frac{Y_{32} Y_{44} Y_{23}}{Y_{33} Y_{44} - Y_{34} Y_{43}} \end{bmatrix}. \quad (\text{A.63})$$

Substituting (A.28), (A.29), (A.35) and (A.36)

$$\overline{\overline{\mathbf{Y}}}_r = \frac{2}{\zeta_0 \cos \theta} \begin{bmatrix} 1 - \sin^2 \theta \cos^2 \theta & -(\sin^2 \theta \cos \phi \sin \phi) \\ -(\sin^2 \theta \cos \phi \sin \phi) & 1 - \sin^2 \theta \sin^2 \theta \end{bmatrix} + \begin{bmatrix} (1 - \sin^2 \theta \cos^2 \theta) j B_x & 0 \\ 0 & (1 - \sin^2 \theta \sin^2 \theta) j B_y \end{bmatrix} + \begin{bmatrix} -\frac{Y_{41} Y_{33} Y_{14}}{Y_{33} Y_{44} - Y_{34} Y_{43}} & \frac{Y_{32} Y_{43} Y_{14}}{Y_{33} Y_{44} - Y_{34} Y_{43}} \\ \frac{Y_{41} Y_{34} Y_{23}}{Y_{33} Y_{44} - Y_{34} Y_{43}} & -\frac{Y_{32} Y_{44} Y_{23}}{Y_{33} Y_{44} - Y_{34} Y_{43}} \end{bmatrix}. \quad (\text{A.64})$$

We can project the reduced admittance matrix on the TE and TM components of an incident plane wave, by multiplying both sides of (A.18) by a rotation matrix, as in [29]

$$\mathbf{R} = \begin{bmatrix} \cos \phi & \sin \phi \\ -\sin \phi & \cos \phi \end{bmatrix}, \quad (\text{A.65})$$

and realizing that $\mathbf{R}^T \mathbf{R}$ equals the unity matrix, we can write (A.18) as

$$\mathbf{R} \overline{\overline{\mathbf{Y}}}_r \mathbf{R}^T \begin{pmatrix} a_1 \\ a_2 \end{pmatrix} = \mathbf{R} \overline{\overline{\mathbf{Y}}}_r \mathbf{R}^T \begin{pmatrix} a_{TE} \\ a_{TM} \end{pmatrix} = \begin{pmatrix} i_{TE} \\ i_{TM} \end{pmatrix}. \quad (\text{A.66})$$

We rename the first term of the reduced admittance matrix multiplied by the rotation matrix and the transverse rotation matrix as:

$$\overline{\overline{\mathbf{Y}}}_{TL} = \mathbf{R} \frac{2}{\zeta_0 \cos \theta} \begin{bmatrix} 1 - \sin^2 \theta \cos^2 \theta & -(\sin^2 \theta \cos \phi \sin \phi) \\ -(\sin^2 \theta \cos \phi \sin \phi) & 1 - \sin^2 \theta \sin^2 \theta \end{bmatrix} \mathbf{R}^T = \begin{bmatrix} \frac{2}{Z_{0,TE}} & 0 \\ 0 & \frac{2}{Z_{0,TM}} \end{bmatrix} \quad (\text{A.67})$$

where $Z_{0,TE} = \zeta_0 / \cos\theta$ and $Z_{0,TM} = \zeta_0 \cos\theta$. The remaining two terms are also multiplied by \mathbf{R} and \mathbf{R}^T . Here we use

$$-\frac{\tilde{Y}_y^* \tilde{Y}_x Y_{34}}{Y_{33} Y_{44} - Y_{34} Y_{43}} - \frac{|\tilde{Y}_x|^2 Y_{44}}{Y_{33} Y_{44} - Y_{34} Y_{43}} = jB_y \quad (\text{A.68})$$

and

$$-\frac{\tilde{Y}_x^* \tilde{Y}_y Y_{43}}{Y_{33} Y_{44} - Y_{34} Y_{43}} - \frac{|\tilde{Y}_y|^2 Y_{33}}{Y_{33} Y_{44} - Y_{34} Y_{43}} = jB_x \quad (\text{A.69})$$

we find after many tedious algebraic steps that

$$\begin{aligned} \overline{\overline{\mathbf{Y}}}_{\text{layer}} &= \mathbf{R} \begin{bmatrix} (1 - \sin^2\theta \cos^2\theta) jB_x & 0 \\ 0 & (1 - \sin^2\theta \sin^2\theta) jB_y \end{bmatrix} \mathbf{R}^T \\ &+ \mathbf{R} \begin{bmatrix} -\frac{Y_{41} Y_{33} Y_{14}}{Y_{33} Y_{44} - Y_{34} Y_{43}} & \frac{Y_{32} Y_{43} Y_{14}}{Y_{33} Y_{44} - Y_{34} Y_{43}} \\ \frac{Y_{41} Y_{34} Y_{23}}{Y_{33} Y_{44} - Y_{34} Y_{43}} & -\frac{Y_{32} Y_{44} Y_{23}}{Y_{33} Y_{44} - Y_{34} Y_{43}} \end{bmatrix} \mathbf{R}^T \\ &= \begin{bmatrix} jB_y \sin^2\phi + jB_x \cos^2\phi + Y_{\text{loop}} & j \sin\phi \cos\phi (B_y - B_x) \\ j \sin\phi \cos\phi (B_y - B_x) & jB_x \sin^2\phi + jB_y \cos^2\phi \end{bmatrix} \end{aligned} \quad (\text{A.70})$$

where

$$Y_{\text{loop}} = \sin^2\theta \frac{\tilde{Y}_x^* \tilde{Y}_y Y_{43}}{Y_{33} Y_{44} - Y_{34} Y_{43}} \approx \frac{1}{\frac{1}{B_x} + \frac{1}{B_y}}. \quad (\text{A.71})$$

From this expression of $\overline{\overline{\mathbf{Y}}}_{TL}$ and $\overline{\overline{\mathbf{Y}}}_{\text{layer}}$, the transmission line model of 3.12 can be drawn, to represent the non-square ADL.

A.2. Multiple Layers

For multiple layers the analysis is very similar to the calculation of the single layer. A $\overline{\overline{\mathbf{Y}}}_{\text{layer}}$ can be found for all layers, separated by a transmission line with length equal to the distance between adjacent layers. The higher order Floquet modes account for the higher order coupling effects between the electrically close layers. We consider two cases: aligned layers and the more general misaligned layers, where the layers can be shifted by \mathbf{s} with respect to one-another.

A.2.1. Aligned Layers

Layers in between other layers

When considering a layer with other layers above and below, the derivation for the admittance matrix entries and the equivalent transmission line circuit remains the same, however we multiply the Green's function with [28]

$$\sum_{n_z=-\infty}^{\infty} (-1)^{n_z} e^{-jk_{zm}|n_z|d_z} = j \tan\left(\frac{k_{zm} d_z}{2}\right) \quad (\text{A.72})$$

where d_z is the distance between adjacent layers and $k_{zm} = \left(k_0^2 - k_{xm}^2 - k_{ym}^2\right)^{1/2}$. Since the steps are very similar to the single layer described above, only the expressions for the

equivalent susceptances $B_{\infty,x}$ and $B_{\infty,y}$ are given here

$$B_{\infty,x} = \frac{j d_y k_0}{\pi \zeta_0} \sum_{m_y \neq 0} \frac{\text{sinc}^2(\pi m_y w_x / d_y)}{|m_y|} \tan\left(\frac{k_z m d_z}{2}\right) \quad (\text{A.73})$$

and

$$B_{\infty,y} = \frac{j d_x k_0}{\pi \zeta_0} \sum_{m_x \neq 0} \frac{\text{sinc}^2(\pi m_x w_y / d_x)}{|m_x|} \tan\left(\frac{k_z m d_z}{2}\right) \quad (\text{A.74})$$

Layers at the top or bottom

When considering a layer with another layer only above or below, the derivation for the admittance matrix entries and the equivalent transmission line circuit remains the same, however we multiply the Green's function with [28]

$$\sum_{n_z=-\infty}^0 (-1)^{n_z} e^{-j k_{zm} |n_z| d_z} = \sum_{n_z=0}^{\infty} (-1)^{n_z} e^{-j k_{zm} |n_z| d_z} = 1 + j \tan\left(\frac{k_z m d_z}{2}\right) \quad (\text{A.75})$$

Since the steps are very similar to the single layer described above, only the expressions for the equivalent susceptances $B_{\text{semi-}\infty,x}$ and $B_{\text{semi-}\infty,y}$ are given here

$$B_{\text{semi-}\infty,x} = \frac{d_y k_0}{2\pi \zeta_0} \sum_{m_y \neq 0} \frac{\text{sinc}^2(\pi m_y w_x / d_y)}{|m_y|} \left(1 + j \tan\left(\frac{k_z m d_z}{2}\right)\right) \quad (\text{A.76})$$

and

$$B_{\text{semi-}\infty,y} = \frac{d_x k_0}{2\pi \zeta_0} \sum_{m_x \neq 0} \frac{\text{sinc}^2(\pi m_x w_y / d_x)}{|m_x|} \left(1 + j \tan\left(\frac{k_z m d_z}{2}\right)\right) \quad (\text{A.77})$$

A.2.2. Misaligned Layers

When a shift between two layers is included, the current distribution of adjacent layers is related by a phase shift not only due to the distance between the layers, but also due to the shift. After the steps in [29] the integral equation to be solved for these layers is

$$\begin{aligned} \sum_{n_z, \text{even}} \int_{-\infty}^{\infty} \int_{-\infty}^{\infty} 4 \mathbf{m}_0(\boldsymbol{\rho}') \mathbf{g}(\boldsymbol{\rho} - \boldsymbol{\rho}', n_z d_z, z=0) d\boldsymbol{\rho}' = \\ \sum_{n_z, \text{odd}} \int_{-\infty}^{\infty} \int_{-\infty}^{\infty} 4 \mathbf{m}_0(\boldsymbol{\rho}') e^{-j k_{\rho_s} s} \mathbf{g}(\boldsymbol{\rho} - \boldsymbol{\rho}', n_z d_z, z=0) d\boldsymbol{\rho}'. \end{aligned} \quad (\text{A.78})$$

Again, following similar steps as described for the single layer, the equivalent layer susceptances are

$$\begin{aligned} B_{\infty,x} = \frac{j d_y k_0}{\pi \zeta_0} \sum_{m_y \neq 0} \frac{\text{sinc}^2(\pi m_y w_x / d_y)}{|m_y|} \\ \left(-\cot\left(-j 2\pi |m_y| \frac{d_z}{d_y}\right) + e^{j 2\pi m_y \frac{s_y}{d_y}} \csc\left(-j 2\pi |m_y| \frac{d_z}{d_y}\right) \right) \end{aligned} \quad (\text{A.79})$$

and

$$B_{\infty,y} = \frac{j d_x k_0}{\pi \zeta_0} \sum_{m_x \neq 0} \frac{\text{sinc}^2(\pi m_x w_y / d_x)}{|m_x|} \left(-\cot\left(-j2\pi|m_x| \frac{d_z}{d_x}\right) + e^{j2\pi m_x \frac{s_x}{d_x}} \csc\left(-j2\pi|m_x| \frac{d_z}{d_x}\right) \right) \quad (\text{A.80})$$

for the layers with other layers both above and below, and

$$B_{\text{semi-}\infty,x} = \frac{j d_y k_0}{\pi \zeta_0} \sum_{m_y \neq 0} \frac{\text{sinc}^2(\pi m_y w_x / d_y)}{|m_y|} \frac{1}{2} \left(-j - \cot\left(-j2\pi|m_y| \frac{d_z}{d_y}\right) + e^{j2\pi m_y \frac{s_y}{d_y}} \csc\left(-j2\pi|m_y| \frac{d_z}{d_y}\right) \right) \quad (\text{A.81})$$

and

$$B_{\text{semi-}\infty,y} = \frac{j d_x k_0}{\pi \zeta_0} \sum_{m_x \neq 0} \frac{\text{sinc}^2(\pi m_x w_y / d_x)}{|m_x|} \frac{1}{2} \left(-j - \cot\left(-j2\pi|m_x| \frac{d_z}{d_x}\right) + e^{j2\pi m_x \frac{s_x}{d_x}} \csc\left(-j2\pi|m_x| \frac{d_z}{d_x}\right) \right) \quad (\text{A.82})$$

for the layers at the top or the bottom of a stack.

Appendix B

Cascading Layers of Non-Square ADL

ADL

This appendix describes the method to cascade the matrices describing the layers of the non-square ADL. The following steps are derived from the more general method to cascade S-parameter matrices of arbitrary size as described in [79]. This appendix focusses on the 4×4 -matrices of the non-square ADL, where the four ports are the top and bottom TE and TM transmission lines of the equivalent circuit representation of the ADL.

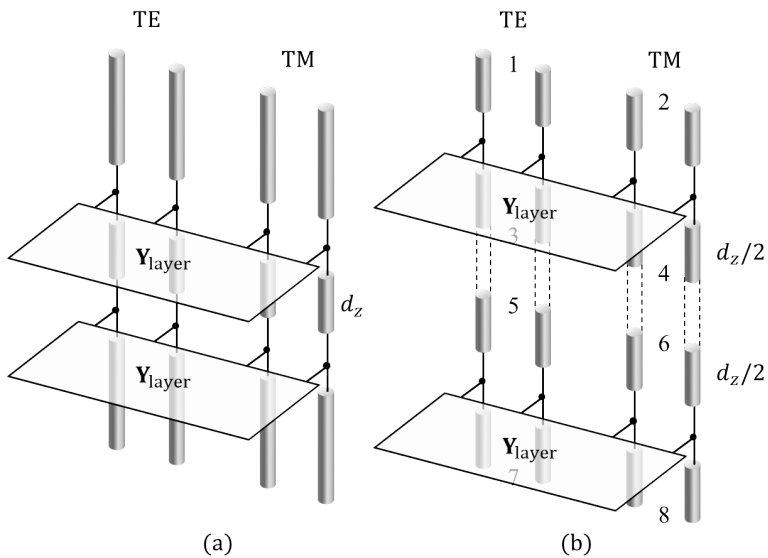


Figure B.1: (a) Transmission line model of multiple layers nonsquare ADL. (b) Total four port structure split in separate four ports for each layer.

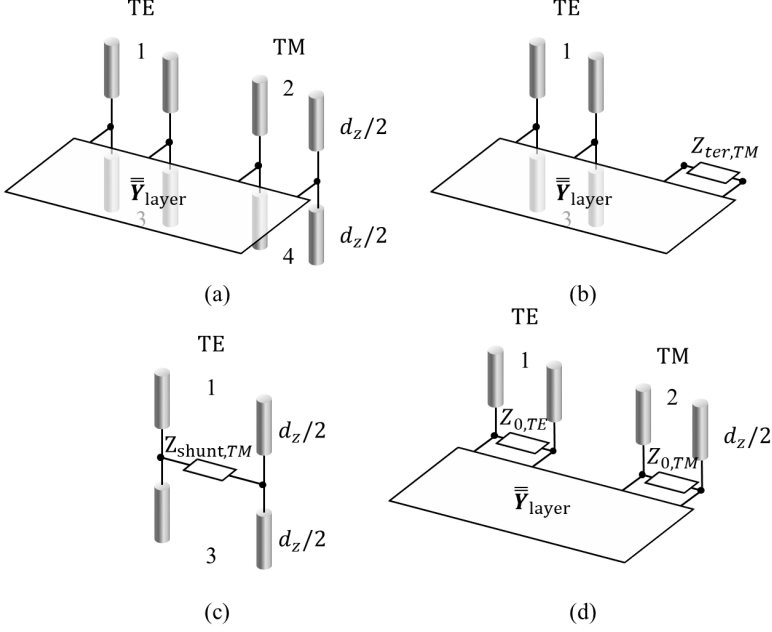


Figure B.2: (a) Transmission line model of one layer non-square ADL in a stack. (b) TM transmission lines terminated on matched loads. (c) Layer and TM termination impedance represented as a shunt impedance in the TE transmission line. (d) Terminating ports 3 and 4 on matched loads.

We consider the multi-layered structure as shown in B.1(a). The ADL is assumed to be in free space, however a different material can be considered by changing the characteristic impedances of the transmission lines. The total structure is split in two four-port networks, as in B.1(b), where we number the ports from 1 to 8. $\overline{\mathbf{Y}}_{\text{layer}}$ is found as in App. A. First the four-port matrices of the layers including the sections of transmission line need to be found. This is done in steps, as shown in Fig. B.2. Since the S-parameters are defined as the reflection and coupling when all other ports are terminated with a matched load, we start by terminating ports 2 and 4 with the characteristic impedance of the TM transmission line $Z_{0, \text{TM}}$. The two impedances in parallel result in the impedance $Z_{\text{ter}, \text{TM}} = Z_{0, \text{TM}}/2$ (Fig. B.2(b)). By rewriting the Y-matrix of the layer into a Z-matrix [75], we can represent the layer and $Z_{\text{ter}, \text{TM}}$ as a shunt impedance, $Z_{\text{shunt}, \text{TM}}$, in the TE transmission line (Fig. B.2(c)), as

$$Z_{\text{shunt}, \text{TM}} = Z_{\text{layer}}(1, 1) - \frac{Z_{\text{layer}}(1, 2)Z_{\text{layer}}(2, 1)}{Z_{\text{layer}}(2, 2) + Z_{\text{ter}, \text{TM}}} \quad (\text{B.1})$$

allowing to find the 2×2 $S_{\text{TE}, \text{TE}}$ -matrix describing the coupling between ports 1 and 3. The same steps are done to find the $S_{\text{TM}, \text{TM}}$ -matrix describing the coupling between ports 2 and 4. Finally, ports 3 and 4 are terminated with $Z_{0, \text{TE}}$ and $Z_{0, \text{TM}}$, as shown in Fig. B.2(d). The S-matrix for ports 1 and 2, $S_{\text{TE}, \text{TM}}$, can be found by cascading the ABCD-matrices of the transmission lines, the shunt impedances and the layer. The total 4×4

S-matrix of the layer including the transmission line sections can now be written as:

$$\mathbf{S}_{\text{layer},1} = \begin{bmatrix} S_{TE,TE}(1,1) & S_{TE,TM}(1,2) & S_{TE,TE}(1,2) & S_{TE,TM}(1,2) \\ S_{TE,TM}(1,2) & S_{TM,TM}(1,1) & S_{TE,TM}(1,2) & S_{TM,TM}(1,2) \\ S_{TE,TE}(1,2) & S_{TE,TM}(1,2) & S_{TE,TE}(2,2) & S_{TE,TM}(1,2) \\ S_{TE,TM}(1,2) & S_{TM,TM}(1,2) & S_{TE,TM}(1,2) & S_{TM,TM}(2,2) \end{bmatrix}. \quad (\text{B.2})$$

We can rename the terms in a more compact way as

$$\mathbf{S}_{\text{layer},1} = \begin{bmatrix} S_{11} & S_{12} & S_{13} & S_{14} \\ S_{21} & S_{22} & S_{23} & S_{24} \\ S_{31} & S_{32} & S_{33} & S_{34} \\ S_{41} & S_{42} & S_{43} & S_{44} \end{bmatrix}. \quad (\text{B.3})$$

The same is then done for the bottom layer, with ports 5 to 8, to find $\mathbf{S}_{\text{layer},2}$:

$$\mathbf{S}_{\text{layer},2} = \begin{bmatrix} S_{55} & S_{56} & S_{57} & S_{58} \\ S_{65} & S_{66} & S_{67} & S_{68} \\ S_{75} & S_{76} & S_{77} & S_{78} \\ S_{85} & S_{86} & S_{87} & S_{88} \end{bmatrix}. \quad (\text{B.4})$$

When we consider the two layers to be disconnected from each other, we can write a big, 8×8 S-matrix as

$$\begin{bmatrix} \mathbf{S}_{\text{layer},1} & \mathbf{0} \\ \mathbf{0} & \mathbf{S}_{\text{layer},2} \end{bmatrix}. \quad (\text{B.5})$$

We now reorganise the terms by swapping rows and columns, so that the outer ports of the total structure, i.e. ports 1, 2, 7 and 8, are grouped in the top left quadrant and the ports that will be connected to each other in the bottom right quadrant

$$\begin{bmatrix} S_{11} & S_{12} & 0 & 0 & 0 & 0 & S_{13} & S_{14} \\ S_{21} & S_{22} & 0 & 0 & 0 & 0 & S_{23} & S_{24} \\ 0 & 0 & S_{77} & S_{78} & S_{75} & S_{76} & 0 & 0 \\ 0 & 0 & S_{87} & S_{88} & S_{85} & S_{86} & 0 & 0 \\ 0 & 0 & S_{57} & S_{58} & S_{55} & S_{56} & 0 & 0 \\ 0 & 0 & S_{67} & S_{68} & S_{65} & S_{66} & 0 & 0 \\ S_{31} & S_{32} & 0 & 0 & 0 & 0 & S_{33} & S_{34} \\ S_{41} & S_{42} & 0 & 0 & 0 & 0 & S_{43} & S_{44} \end{bmatrix}. \quad (\text{B.6})$$

We define separate matrices for each 4×4 quadrant, so that B.6 becomes

$$\begin{bmatrix} \mathbf{S}_{11} & \mathbf{S}_{12} \\ \mathbf{S}_{21} & \mathbf{S}_{22} \end{bmatrix}. \quad (\text{B.7})$$

To connect the ports, we define a permutation matrix, where the entries are 0 for ports that are not directly connected and 1 for ports that are directly connected. To make this permutation matrix, we look at the quadrant in B.6 with the ports that are to be

connected, or \mathbf{S}_{22} , and we see the order of the rows and columns to be 5, 6, 3 and 4. Therefore, the permutation matrix becomes

$$\mathbf{C} = \begin{bmatrix} 0 & 0 & 1 & 0 \\ 0 & 0 & 0 & 1 \\ 1 & 0 & 0 & 0 \\ 0 & 1 & 0 & 0 \end{bmatrix} \quad (\text{B.8})$$

where the entry equals 1 when the ports related to the row and column are directly connected. The total 4×4 S -parameter matrix of the two layers, \mathbf{S}' can now be found as:

$$\mathbf{S}' = \mathbf{S}_{11} + \mathbf{S}_{12} (\mathbf{C} - \mathbf{S}_{22})^{-1} \mathbf{S}_{12}. \quad (\text{B.9})$$

Appendix C

Modeling of Power Amplifiers as Sources

It is convenient to represent the PA, schematically shown in Fig. C.1(a), as a Norton equivalent source. The resulting circuit is depicted in Fig. C.1(b), where the PA is represented as a voltage controlled current source. The control voltage signal v_{in} determines the value of the current and generator impedance. The PAs under consideration consist of multiple sub-PAs which are connected in parallel, that can be either on or off, according to the simplified circuit representation shown in Fig. C.1(c). The signal v_{in} controls the number of sub-PAs that are switched on (N_{on}). Each active sub-PA can also be represented as a Norton equivalent source with current generator I_{sub} and internal resistance R_{sub} , assumed to be $2k\Omega$. On the contrary, the inactive sub-PAs are ideally open circuits. We assume that the PA is designed such that the parasitics can be represented as a single resistor, $R_{par} = 480\Omega$, thus capacitive and inductive effects are neglected.

Therefore, the current $I_{PA}(v_{in})$ can be expressed as $I_{PA} = I_{sub}N_{on}$, while the impedance $Z_{PA}(v_{in}) = R_{par} || (R_{sub}/N_{on})$. The control voltage v_{in} is assumed to be linearly proportional to N_{on} and normalized so that $v_{in} = 0$ corresponds to all sub-PAs switched off and $v_{in} = 1$ refers to all sub-PAs being on. The resulting current and impedance of the Norton generator are shown in Fig. C.2.

If we assume PAs operating as class B, the total power supplied to the PA is given by [68]:

$$P_{supply} = V_{DD} \frac{2}{\pi} |I_{out}| \quad (C.1)$$

where V_{DD} is the drain voltage of the transistor (Fig. C.1(c)) and I_{out} is the output voltage of the PA. The output power is

$$P_{out} = \frac{1}{2} |V_{out}|^2 Re \left\{ \frac{1}{Z_{out}} \right\} \quad (C.2)$$

where V_{out} is the output voltage of the PA and $Z_{out} = V_{out}/I_{out}$. The efficiency of a class B PA can be found as the ratio between P_{out} and P_{supply} that, for real output impedance,

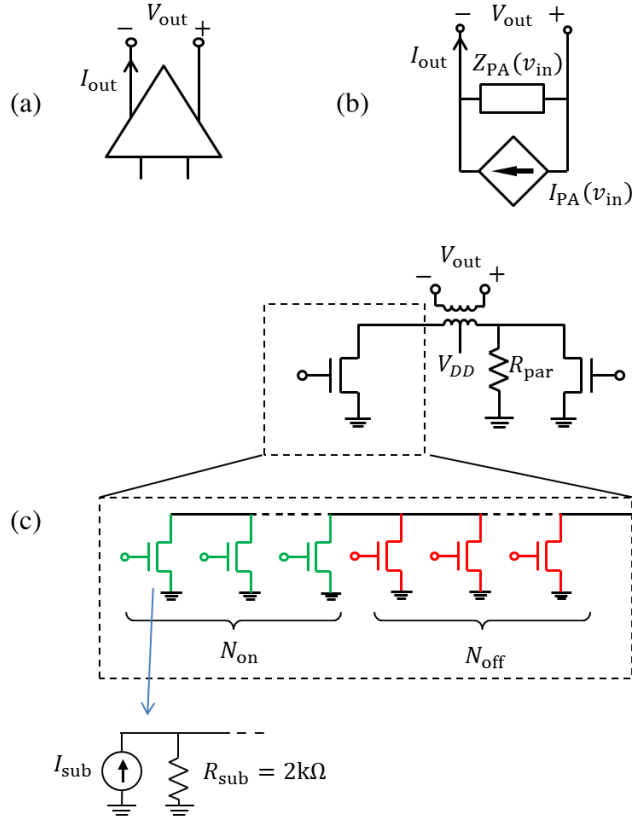


Figure C.1: (a) Circuit representation of a PA consisting of multiple sub-PAs. (b) Norton-equivalent circuit of the PA. (c) Schematic drawing of a PA consisting of multiple sub-PAs.

gives

$$\eta = \frac{\pi |V_{out}|}{4 V_{DD}}. \quad (C.3)$$

Since $|V_{out}|$ cannot exceed V_{DD} , the maximum efficiency of a class B PA is $\eta_{max} = \pi/4 \approx 79\%$ and is reached when $|V_{out}| = V_{DD}$. If a certain frequency range is considered, since the output voltages of the PAs cannot exceed the supply voltage, the condition

$$|V_{out}| \leq V_{DD} \quad (C.4)$$

can be imposed for every frequency and for the full range of output current. In practice, this can be realized by tuning the maximum value for control signal v_{in} at different frequencies. This results in a changing number of sub-PAs being switched on for different frequencies, and therefore in a frequency dependent port impedance Z_{PA} .

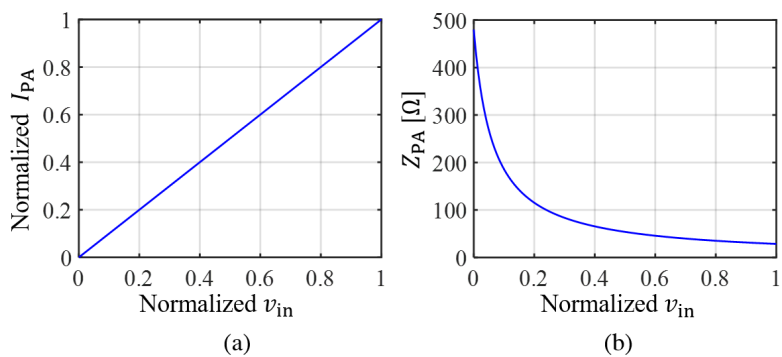


Figure C.2: (a) Normalized current and (b) internal impedance of the Norton generator, as a function of v_{in} .

Bibliography

- [1] H. Shan, N. Conrad, S. Hathorn, J. Peterson, and S. Mohammadi, "Implementation of a differential mm-wave CMOS SOI power amplifier," *IEEE MTT-S Int. Microw. Symp. Hardware Systems 5G and beyond*, Atlanta, GA, 2019, pp. 1-3.
- [2] M.H. Motaseri, J. Aikio, T. Rahkonen, and A. Pärssinen, "Design of stacked-MOS transistor mm-wave class C amplifiers for Doherty power amplifiers," *IEEE Nordic Circuits Systems Conf., NORCHIP and Int. Symp. SoC*, Tallinn, Estonia, 2018, pp. 1-5.
- [3] M.H. Motaseri, J. Aikio, T. Rahkonen, and A. Pärssinen, "Performance improvement of multi-stacked CMOS mm-wave power amplifiers based on negative capacitance phase compensation," *Int. Workshop Integr. Nonlinear Microw. mm-Wave Circuits*, Brive La Gaillarde, France, 2018, pp. 1-3.
- [4] K. Chang and C. Sun, "Millimeter-wave power combining techniques," *IEEE Trans. Microwave Theory Tech.*, vol. 31, no. 2, pp. 91-107, Feb. 1983.
- [5] R. J. Hwu, C. F. Jou, N. C. Luhmann, M. Kim, W. W. Lam, Z. B. Popovic, and D. B. Rutledge, "Array concepts for solid-state and vacuum microelectronics millimeter-wave generation," *IEEE Trans. Electron. Devices*, vol. 36, no. 11, pp. 2645-2650, Nov. 1989.
- [6] J.-G. Kim and G. M. Rebeiz, "Miniature four-way and two-way 24 GHz Wilkinson power dividers in 0.13 um CMOS," *IEEE Microw. Wireless Compon. Lett.*, vol. 17, no. 9, pp. 658-660, Sep. 2007.
- [7] Y. Zhao, J. R. Long, and M. Spirito, "Compact transformer power combiners for millimeter-wave wireless applications," *IEEE Radio Frequency Integrated Circuits Symposium*, Anaheim, CA, 2010, pp. 223-226.
- [8] J. R. Long, W. L. Chan, Y. Zhao, and M. Spirito, "Silicon VLSI catches the millimeter wave," *IEEE Communications Magazine*, vol. 49, no. 10, pp. 182-189, Oct. 2011.
- [9] J. R. Long, Y. Zhao, W. Wu, M. Spirito, L. Ver, a and E. Gordon, "Passive circuit technologies for mm-wave wireless systems on silicon," *IEEE Trans. Circuits Systems*, vol. 59, no. 8, pp. 1680-1693, Aug. 2012.
- [10] H. Sun, X. Zhu, R. Liu, and Z. H. Jiang, "Mm-wave waveguide traveling-wave power combiner design using an equivalent circuit model," *IEEE Access*, vol. 7, pp. 88327-88337, Jul. 2019.
- [11] N. S. Cheng, A. Alexanian, M. G. Case, and R.A. York, "20 watt spatial power combiner in waveguide," *IEEE MTT-S Int. Microw. Symp. Dig.*, vol. 3, pp. 1457-1460, Jun. 1998.

- [12] Z. Hu, M. Alonso-delPino, D. Cavallo, H. T. Shivamurthy, and M. Spirito, "Integrated waveguide power combiners with artificial dielectrics for mm-wave systems," *IEEE Int. Microw. Symp.*, Honolulu, HI, 2017, pp. 646-649.
- [13] A. Roev, R. Maaskant, A. Höök, and M. Ivashina, "Wideband mm-wave transition between a coupled microstrip line array and SIW for high-power generation MMICs," *IEEE Microw. Wireless Components Lett.*, vol. 28, no. 10, pp. 867-869, Oct. 2018.
- [14] A. Agah, H. T. Dabag, B. Hanafi, P. M. Asbeck, J. F. Buckwalter, and L. E. Larson, "Active millimeter-wave phase-shift Doherty power amplifier in 45-nm SOI CMOS," *IEEE J. Solid-State Circuits*, vol. 48, no. 10, pp. 2338-2350, Oct. 2013.
- [15] W. H. Doherty, "A new high efficiency power amplifier for modulated waves," *Proc. IRE*, vol. 24, no. 9, pp. 1163-1182, Sep. 1936.
- [16] H. Wang, S. Hu, T. Chi, F. Wang, S. Li, M.-Y. Huang, and J. S. Park, "Towards energy-efficient 5G mm-wave links: Exploiting broadband mm-wave Doherty power amplifier and multi-feed antenna with direct on-antenna power combining," *IEEE Bipolar/BiCMOS Circuits and Technology Meeting*, Miami, FL, USA, 2017, pp. 30-37.
- [17] M. Mortazavi, Y. Shen, D. P. N. Mul, L. C. N. de Vreede, M. Spirito and M. Babaie, "A 30GHz 4-way series Doherty digital polar transmitter achieving 18% drain efficiency and -27.6dB EVM while transmitting 300MHz 64-QAM OFDM signal," *2021 IEEE Custom Integrated Circuits Conference (CICC)*, Apr. 2021.
- [18] E. Kruglick, "Network coverage by cycling through beam shape coverage configurations," Patent, no. WO2013/028187A1, Feb. 2013.
- [19] D. R. Jackson and A. A. Oliner, "A leaky-wave analysis of the high-gain printed antenna configuration," *IEEE Trans. Antennas Propag.*, vol. 36, no. 7, pp. 905-910, Jul. 1988.
- [20] E. Magill and H. Wheeler, "Wide-angle impedance matching of a planar array antenna by a dielectric sheet," *IEEE Trans. Antennas Propag.*, vol. 14, no. 1, pp. 49-53, Jan. 1966.
- [21] C.-C. Chen, "Wideband wide-angle impedance matching and polarization characteristics of circular waveguide phased arrays," *IEEE Trans. Antennas Propag.*, vol. 22, no. 3, pp. 414-418, May 1974.
- [22] T. R. Cameron and G. V. Eleftheriades, "Analysis and characterization of a wide-angle impedance matching metasurface for dipole phased arrays," *IEEE Trans. Antennas Propag.*, vol. 63, no. 9, pp. 3928-3938, Sept. 2015.
- [23] D. Cavallo, W.H. Syed, and A. Neto, "Connected-slot array with artificial dielectrics: A 6 to 15 GHz dual-pol wide-scan prototype," *IEEE Trans. Antennas Propag.*, vol. 66, no. 6, pp. 3201-3206, Jun. 2018.

- [24] D. Cavallo, W. H. Syed, and A. Neto, "Closed-form analysis of artificial dielectric layers—Part I: Properties of a single layer under plane-wave incidence," *IEEE Trans. Antennas Propag.*, vol. 62, no. 12, pp. 6256-6264, Dec. 2014.
- [25] W. H. Syed, G. Fiorentino, D. Cavallo, M. Spirito, P. M. Sarro, and A. Neto, "Design, fabrication and measurement of 0.3 THz on-chip double-slot antenna enhanced by artificial dielectrics," *IEEE Trans. THz Sci. Tech.*, vol. 5, no. 2, pp. 288-298, Mar. 2015.
- [26] D. Cavallo, W. H. Syed and A. Neto, "Artificial dielectric enabled antennas for high frequency radiation from integrated circuits," *11th Eur. Conf. Antennas Propagation*, Paris, 2017, pp. 1626-1628.
- [27] W. H. Syed, D. Cavallo, H. Thippur Shivamurthy, and A. Neto, "Wideband, wide-scan planar array of connected slots loaded with artificial dielectric superstrates," *IEEE Trans. Antennas Propag.*, vol. 64, no. 2, pp. 543-553, Feb. 2016
- [28] D. Cavallo, W. H. Syed, and A. Neto, "Closed-form analysis of artificial dielectric layers—Part II: Extension to multiple layers and arbitrary illumination," *IEEE Trans. Antennas Propag.*, vol. 62, no. 12, pp. 6265-6273, Dec. 2014.
- [29] D. Cavallo and C. Felita, "Analytical formulas for artificial dielectrics with non-aligned layers," *IEEE Transactions on Antennas and Propagation*, vol. 65, no. 10, pp. 5303-5311, Oct. 2017.
- [30] D. Cavallo, "Analysis of artificial dielectric layers with finite conductivity," *Forum for Electromagnetic Research Methods and Application Technologies (FERMAT)*, vol. 31, no. 5, Jan. 2019
- [31] R. Gardelli, M. Albani, and F. Capolino, "Array thinning by using antennas in a Fabry-Perot cavity for gain enhancement," *IEEE Trans. Antennas Propag.*, vol. 54, no. 7, pp. 1979-1990, Jul. 2006.
- [32] A. Neto, N. Llombart, G. Gerini, M. Bonnedal, and P. de Maagt, "EBG enhanced feeds for the improvement of the aperture efficiency of reflector antennas," *IEEE Trans. Antennas Propag.*, vol. 55, no. 8, pp. 2185-2193, Aug. 2007.
- [33] A. Neto, M. Etorre, G. Gerini, and P. de Maagt, "Leaky wave enhanced feeds for multibeam reflectors to be used for telecom satellite based links," *IEEE Trans. Antennas Propag.*, vol. 60, no. 1, pp. 110-120, Jan. 2012.
- [34] D. Blanco, N. Llombart, and E. Rajo-Iglesias, "On the use of leaky wave phased arrays for the reduction of the grating lobe level," *IEEE Trans. Antennas Propag.*, vol. 62, no. 4, pp. 1789-1795, Apr. 2014.
- [35] G. Von Trentini, "Partially reflecting sheet arrays," *IRE Trans. Antennas Propag.*, vol. AP-4, pp. 666-671, 1956.
- [36] D. Cavallo, "Dissipation losses in artificial dielectric layers," *IEEE Trans. Antennas Propag.*, vol. 66, no. 12, 2018.

- [37] G. Valerio, Z. Sipus, A. Grbic, and O. Quevedo-Teruel, "Accurate equivalent-circuit descriptions of thin glide-symmetric corrugated metasurfaces," *IEEE Trans. Antennas Propag.*, vol. 65, no. 5, pp. 2695-2700, May 2017.
- [38] A. Neto and S. Maci, "Green's function for an infinite slot printed between two homogeneous dielectrics. Part I: Magnetic currents," *IEEE Trans. Antennas Propag.*, vol. 51, no. 7, pp. 1572-1581, Jul. 2003.
- [39] D. Cavallo, W. H. Syed, and A. Neto, "Equivalent transmission line models for the analysis of edge effects in finite connected and tightly coupled arrays," *IEEE Trans. Antennas Propag.*, vol. 65, no. 4, pp. 1788-1796, Apr. 2017.
- [40] S. van Berkel, A. Garufo, N. Llombart, and A. Neto, "A quasi-analytical tool for the characterization of transmission lines at high frequencies," *IEEE Antennas Propag. Mag.*, vol. 58, no. 3, pp. 82-90, Jun. 2016.
- [41] A. Roev, P. Taghikhani, R. Maaskant, C. Fager, and M. V. Ivashina, "A wideband and low-loss spatial power combining module for mm-wave high-power amplifiers," *IEEE Access*, vol. 8, pp. 194858-194867, Oct. 2020.
- [42] C. A. Balanis, *Antenna Theory: Analysis and Design, 4th Ed.* John Wiley & Sons, Inc., Hoboken, New Jersey, 2016.
- [43] N. Behdad and K. Sarabandi, "Dual-band reconfigurable antenna with a very wide tunability range," *IEEE Trans. Antennas Propag.*, vol. 54, no. 2, pp. 409-416, Feb. 2006.
- [44] C. Occhiuzzi, S. Cippitelli, and G. Marrocco, "Modeling, design and experimentation of wearable RFID sensor tag," *IEEE Trans. Antennas Propag.*, vol. 58, no. 8, pp. 2490-2498, Aug. 2010.
- [45] Y. Wang and S. Chung, "A short open-end slot antenna with equivalent circuit analysis," *IEEE Trans. Antennas Propag.*, vol. 58, no. 5, pp. 1771-1775, May 2010.
- [46] S. B. Cohn, "Slot line on a dielectric substrate," *IEEE Trans. Microw. Theory Tech.*, vol. 17, no. 10, pp. 768-778, Oct. 1969.
- [47] R. Garg and K. C. Gupta, "Expressions for wavelength and impedance of a slotline," *IEEE Trans. Microw. Theory Tech.*, vol. 24, no. 8, pp. 532-532, Aug. 1976.
- [48] J. J. Lee, "Slotline impedance," *IEEE Trans. Microw. Theory Tech.*, vol. 39, no. 4, pp. 666-672, Apr. 1991.
- [49] J. Svačina, "Dispersion characteristics of multilayered slotlines — A simple approach," *IEEE Trans. Microw. Theory Tech.*, vol. 47, no. 9, pp. 1826-1829, Sep. 1999.
- [50] M. Himdi and J. P. Daniel, "Analysis of printed linear slot antenna using lossy transmission line model," *Electronic letters*, vol. 28, no. 6, pp. 598-601, Mar. 1992.
- [51] R. Garg, P. Bhartia, I. Bahl, and A. Ittipiboon, *Microstrip Antenna Design Handbook*. Norwood, MA, USA: Artech House, Inc., 2001.

- [52] J. E. Ruyle and J. T. Bernhard, "A wideband transmission line model for a slot antenna," *IEEE Trans. Antennas Propag.*, vol. 61, no. 3, pp. 1407-1410, Mar. 2013.
- [53] D. Cavallo, A. Neto, and G. Gerini, "Analytical description and design of printed dipole arrays for wideband wide-scan applications," *IEEE Trans. Antennas Propag.*, vol. 60, no. 12, pp. 6027-6031, Dec. 2012.
- [54] D. S. Jones, *Methods in Electromagnetic Wave Propagation, 2nd Ed.* IEEE Press, New York, 1994.
- [55] M. Albani, A. Mazzinghi, and A. Freni, "Rigorous MoM analysis of finite conductivity effects in RLSA antennas," *IEEE Trans. Antennas Propag.*, vol. 59, no. 11, pp. 4023-4032, Nov. 2011.
- [56] A. Neto and J. J. Lee, "Ultrawide-band properties of long slot arrays," *IEEE Trans. Antennas Propag.*, vol. 54, no. 2, pp. 534-543, Feb. 2006.
- [57] R. Ozzola, "Spectral domain methods for wide-band phased arrays analysis," M.Sc. Thesis, Università degli Studi di Firenze, Florence, Italy, 2019.
- [58] W. E. Kock, "Metallic delay lenses," *Bell System Tech. J.*, vol. 27, no. 1, pp. 58-82, Jan. 1948.
- [59] S. S. D. Jones and J. Brown, "Metallic delay lenses," *Nature*, vol. 163, no. 4139, pp. 324-325, Feb. 1949.
- [60] R. E. Collin, *Field Theory of Guided Waves, 2nd Ed.* IEEE Press, New York, 1990.
- [61] E. Martini, G. M. Sardi and S. Maci, "Homogenization processes and retrieval of equivalent constitutive parameters for multisurface-metamaterials," *IEEE Trans. Antennas Propag.*, vol. 62, no. 4, pp. 2081-2092, April 2014.
- [62] S. Barzegar-Parizi and B. Rejaei, "Calculation of effective parameters of high permittivity integrated artificial dielectrics," *IET Microwaves, Antennas Propag.*, vol. 9, no. 12, pp. 1287-1296, Sep. 2015.
- [63] F. Mesa, R. Rodríguez-Berral, M. García-Vigueras, F. Medina and J. R. Mosig, "Simplified modal expansion to analyze frequency-selective surfaces: An equivalent circuit approach," *IEEE Trans. Antennas Propag.*, vol. 64, no. 3, pp. 1106-1111, March 2016.
- [64] J. R. Wait, "Theories of scattering from wire-grid and mesh structures," in *Electromagnetic Scattering*, P.L.E. Uslenghi, Ed. New York: Academic, 1978, pp. 253-287.
- [65] R. C. Compton and D. B. Rutledge, "Approximation techniques for planar periodic structures," *IEEE Trans. Microw. Theory Techniques*, vol. 33, no. 10, pp. 1083-1088, Oct. 1985.
- [66] O. Luukkonen, C. Simovski, G. Granet, G. Goussetis, D. Lioubtchenko, A. V. Raisanen, and S. A. Tretyakov, "Simple and accurate analytical model of planar grids and high-impedance surfaces comprising metal strips or patches," *IEEE Trans. Antennas Propag.*, vol. 56, no. 6, pp. 1624-1631, Jun. 2008.

- [67] S. A. Schelkunoff, "Some equivalence theorems of electromagnetics and their application to radiation problems," *Bell System Tech. J.*, vol. 15, pp. 92–112, 1936.
- [68] B. Razavi, *RF Microelectronics*. Castleton, NY: Prentice Hall, 2012.
- [69] W.H. Syed, G. Fiorentino, D. Cavallo, M. Spirito, P.M. Sarro, and A. Neto, "Design, fabrication, and measurements of a 0.3 THz on-chip double slot antenna enhanced by artificial dielectrics," *IEEE Trans. THz Science Techn.*, vol. 5, no. 2, pp. 288–298, March 2015.
- [70] W. C. E. Neo, J. Qureshi, M. J. Pelk, J. R. Gajadharsing, and L. C. N. de Vreede, "A mixed-signal approach towards linear and efficient N-way Doherty amplifiers," *IEEE Trans. Microw. Theory Techn.*, vol. 55, no. 5, pp. 866–879, May 2007.
- [71] Southwest Microwave, "End Launch 2.92mm (K) 40 GHz Jack (Female) Standard Block (.500)" [online] <https://mpd.southwestmicrowave.com/product/1092-03a-6-end-launch-2-92mm-k-40-ghz-jack-female-standard-block/> (accessed August 17, 2021)
- [72] F. Monticone and A. Alù, "Leaky-wave theory, techniques, and applications: From microwaves to visible frequencies," *Proceedings of the IEEE*, vol. 103, no. 5, pp. 793–821, May 2015.
- [73] R. Hansen, "Focal region characteristics of focused array antennas," *IEEE Trans. Antennas Propag.*, vol. 33, no. 12, pp. 1328–1337, Dec. 1985.
- [74] N. Llombart, A. Neto, G. Gerini, M. Bonnedal and P. de Maagt, "Impact of mutual coupling in leaky wave enhanced imaging arrays," *IEEE Trans. Antennas Propag.*, vol. 56, no. 4, pp. 1201–1206, Apr. 2008.
- [75] D. M. Pozar, *Microwave Engineering, 4th Ed.* John Wiley & Sons, Inc., Hoboken, New Jersey, 2012
- [76] Rosenberger, "02K722-40MS3" Technical data sheet [online] https://products.rosenberger.com/_ocassets/db/02K722-40MS3.pdf (accessed July 22, 2021)
- [77] S. Groiss, I. Bardi, O. Biro, K. Preis, and K. R. Richter, "Parameters of lossy cavity resonators calculated by the finite element method," *IEEE Trans. Magnetics*, vol. 32, no. 3, pp. 894–897, May 1996.
- [78] Rogers corporation, "Copper foils for high frequency materials" Data sheet [online] <http://payalnik.com.ua/upload/docum/Copper-Foils-for-High-Frequency-Circuit-Materials.pdf> (accessed July 22, 2021)
- [79] E. Salerno, "Appunti di microonde," (Italian), online: http://www1.isti.cnr.it/~salerno/Microonde/Microonde_08062010.pdf, accessed on 12-05-2021.

Summary

Power Combiner and Antenna Array Concepts for Millimeter Wave Applications

The fifth generation of mobile communication poses challenges in the form of increased data volume, network scalability and efficient network operation. An important part in meeting these requirements is the use of the mm-wave frequency range, enabling the use of a wide bandwidth and therefore the desired high-data rates. However, a challenging aspect of mm-wave communication lies in the efficient generation of RF power. In fact, currently reported power amplifiers are unable to reach the required output power for commercial applications. A typical way to increase the available power is to combine the signal from multiple sources using a power combiner. Power combiners in the mm-wave frequency range have been investigated for many years, but typical problems that occur are area occupation and insertion losses that grow directly with the number of inputs.

To overcome these problems, this dissertation investigates a waveguide power combiner. Specifically a parallel plate waveguide is used here, as it presents a frequency independent impedance behavior and, depending on the required output power, more sources can easily be added in parallel without the need for re-optimization of the structure. To allow amplitude modulation without a significant drop in the operating efficiency of the power amplifiers, a Doherty combiner is implemented in the parallel plate waveguide. A 6-to-1 demonstrator, operating in the frequency band around 28 GHz, is fabricated in standard PCB technology and the measured results show a good agreement with simulations. The operating efficiency of the ideal power amplifiers feeding the power combiner is higher than 50% over the entire bandwidth, both at power back-off and at full power.

Besides the efficient power combination, to reduce the area occupation and costs of antenna systems, multi-mode operation is a desired property. In base stations for wireless cellular networks, the ability to switch between narrow or wide beams allows to achieve an optimal capacity for different user distributions. Another advantage of multi-mode operation lies in the limited number of output channels of mm-wave integrated circuits. The multi-mode operation allows the reuse of these output channels for multiple purposes. For scenarios where beam efficiency is important, a wide angle impedance matching layer that supports leaky waves can be beneficial. The leaky waves focus the radiated power to certain directions, which allows for the shaping of the radiation pattern of an antenna.

In this dissertation an array of cavity backed slot antennas with an artificial dielectric superstrate is investigated to be used for dual-mode operation. Using the leaky waves the element pattern of the antennas are shaped to allow for a narrow beam that scans up to 45° without scan loss, and a wide beam with a -3dB -beamwidth of $\pm 45^\circ$. The leaky waves allow to truncate the dielectric and the ground plane without affecting sig-

nificantly the radiation patterns. The trade-off between mutual coupling between the elements and the gain enhancement due to the leaky waves is studied. The switching between the narrow and the wide beam can be achieved electronically by applying either a linear or a quadratic phase shift between the elements. Oscillations in the radiation pattern of the wide beam can be reduced by applying an amplitude taper on the excitations as well. A 30 GHz demonstrator is fabricated in standard PCB technology. The measured results show a good agreement with simulations and present a 7% operational bandwidth.

Regarding the modeling aspects, an efficient simulation tool is derived for the analysis of planar slot antennas. A method of moments is presented, with basis functions only at the feeding point of the slot and at the edges. Based on this spectral method of moments procedure, an equivalent transmission line model is derived, where the radiation and reactive power around the feeding point and the end points of the slot are accurately represented by impedances, and the length of the slot is accounted for with the transmission line. More feeding points can be added along the line, enabling the analysis of finite connected arrays of slots.

Also on the analysis of artificial dielectric layers, the previous formulations are generalized to allow for non-identical layers and for non-square patches and unit cells. These extensions provide more degrees of freedom in the design of matching layers and radiation pattern shaping. An equivalent circuit is derived based on the method, to describe rigorously the coupling between the TE and TM modes for the non-square ADLs.

Samenvatting

Vermogensopteller en Antennestelsel Concepten voor Millimetergolf Applicaties

De vijfde generatie mobiele communicatie stelt uitdagingen in de vorm van een groter datavolume, netwerkschaalbaarheid en efficiënte netwerkwerking. Een belangrijk onderdeel om aan deze eisen te voldoen is het gebruik van het mm-golf frequentiebereik, waardoor een brede bandbreedte en daarmee de gewenste hoge datasnelheden kunnen worden gebruikt. Een uitdagend aspect van mm-golfcommunicatie ligt echter in de efficiënte opwekking van RF-vermogen. De momenteel gerapporteerde vermogensversterkers zijn niet in staat om het vereiste uitgangsvermogen voor commerciële toepassingen te bereiken. Een typische manier om het beschikbare vermogen te vergroten, is door het signaal van meerdere bronnen te combineren met behulp van een vermogensopteller. Vermogensoptellers in het mm-golffrequentiebereik zijn al vele jaren onderzocht, maar typische problemen die optreden zijn oppervlaktebezetting en invoegverliezen die evenredig toenemen met het aantal ingangen.

Om deze problemen op te lossen, onderzoekt dit proefschrift een golfgeleider vermogensopteller. Specifiek wordt hier een parallelle plaatgolfgeleider gebruikt, omdat deze een frequentie-onafhankelijk impedantiegedrag vertoont en, afhankelijk van het vereiste uitgangsvermogen, gemakkelijk meer bronnen parallel kunnen worden toegevoegd zonder dat de structuur opnieuw moet worden geoptimaliseerd. Om amplitudemodulatie mogelijk te maken zonder een significante daling van de operationele efficiëntie van de vermogensversterkers, is een Doherty-opteller geïmplementeerd in de parallelle plaatgolfgeleider. Een 6-op-1 prototype, dat werkt in de frequentieband rond de 28 GHz, is gefabriceerd in standaard PCB-technologie en de meetresultaten laten een goede overeenkomst zien met simulaties. De operationele efficiëntie van de ideale vermogensversterkers die de vermogensopteller voeden, is hoger dan 50% over de gehele bandbreedte, zowel bij vermogens “back-off” als bij vol vermogen.

Naast de efficiënte vermogenscombinatie, is multimodus-werking een gewenste eigenschap om de oppervlaktebezetting en kosten van antennesystemen te verminderen. In basisstations voor draadloze mobiele netwerken maakt de mogelijkheid om te schakelen tussen smalle of brede bundels het mogelijk om een optimale capaciteit te bereiken voor verschillende gebruikersdistributies. Een ander voordeel van multimodus-werking ligt in het beperkte aantal uitgangskanalen van geïntegreerde schakelingen voor mm-golven. Dankzij de multimodus-werking kunnen deze uitgangskanalen voor meerdere doeleinden worden hergebruikt. Voor scenario's waar bundelefficiëntie belangrijk is, kan een groothoekimpedantie-aanpassingslaag die lekkende golven ondersteunt gunstig zijn. De lekkende golven richten het uitgestraalde vermogen in bepaalde richtingen, waardoor het stralingspatroon van een antenne kan worden gevormd.

In dit proefschrift wordt een reeks van holte-gesteunde gleufantennes met een kunstmatige diëlektrische superstraat onderzocht om te worden gebruikt voor dual-modus

werking. Met behulp van de lekkende golven wordt het elementpatroon van de antennes gevormd om een smalle bundel mogelijk te maken die tot 45° scant zonder scanverlies, en een brede bundel met een -3dB -bundelbreedte van $\pm 45^\circ$. De lekkende golven maken het mogelijk om het diëlektricum en het grondvlak af te kappen zonder de stralingspatronen significant te beïnvloeden. De afweging tussen onderlinge koppeling tussen de elementen en de versterkingsfactor door de lekkende golven wordt bestudeerd. Het schakelen tussen de smalle en de brede bundel kan elektronisch worden bereikt door een lineaire of een kwadratische faseverschuiving tussen de elementen toe te passen. Oscillaties in het stralingspatroon van de brede bundel kunnen worden verminderd door ook een amplitudetaper toe te passen op de excitaties. Een demonstrator van 30 GHz is vervaardigd in standaard PCB-technologie. De gemeten resultaten laten een goede overeenkomst zien met simulaties en presenteren een operationele bandbreedte van 7%.

Met betrekking tot de modelleringsaspecten wordt een efficiënte simulatietool afgeleid voor de analyse van vlakke gleufantennes. Er wordt een methode van momenten gepresenteerd, met basisfuncties alleen op het invoerpunt van de sleufantenne en aan de randen. Op basis van deze spectrale methode van momentenprocedure wordt een equivalent transmissielijnmodel afgeleid, waarbij de straling en het reactieve vermogen rond het voedingspunt en de eindpunten van de sleufantenne nauwkeurig worden weergegeven door impedanties, en de lengte van de sleuf wordt berekend met de transmissielijn. Langs de lijn kunnen meer voedingspunten worden toegevoegd, waardoor de analyse van eindig verbonden gleufantenne reeksen mogelijk is.

Ook voor de analyse van kunstmatige diëlektrische lagen, worden de eerdere formuleringen gegeneraliseerd om niet-identieke lagen en niet-vierkante vlakken en eenheidscellen mogelijk te maken. Deze uitbreidingen bieden meer vrijheidsgraden bij het ontwerpen van anti-reflectie lagen en het vormen van stralingspatronen. Op basis van de methode wordt een equivalent circuit afgeleid om de koppeling tussen de TE- en TM-modi voor de niet-vierkante kunstmatige diëlektrische lagen rigoureus te beschrijven.

List of Publications

Journal Papers

- J.1** R.M. van Schelven, D. Cavallo, and A. Neto, "Equivalent circuit models of finite slot antennas," *IEEE Trans. Antennas Propag.*, Vol. 67, No. 7, pp. 4367-4376, Jul. 2019.
- J.2** R.M. van Schelven, A. Fiorellini Bernardis, P. Sberna, and A. Neto, "Drude dispersion in the transmission line modelling of bulk absorbers at sub-mm wave frequencies: A tool for absorber optimization," *IEEE Antennas and Propagation Magazine*, 2021. (Early Access)
- J.3** R.M. van Schelven, and D. Cavallo, "Analysis of non-square artificial dielectric layers and application to the design of anisotropic slabs", *IEEE Antennas Wirel. Propag. Lett.*, 2021. (Early Access)
- J.4** R.M. van Schelven, M. Spirito, and D. Cavallo, "Efficient waveguide power combiners at mm-wave frequencies", (*IEEE trans. Antennas Propag.*, under review)
- J.5** R.M. van Schelven, W. Syed, G. Carluccio, K. Doris, A. de Graauw, A. Neto, and D. Cavallo, "Phased array with pattern shaping and scan loss reduction for millimeter waves", (*IEEE trans. Antennas Propag.*, in preparation)

Conference Papers

- C.1** R.M. van Schelven, D. Cavallo, and A. Neto, "Equivalent circuit models of finite slot antennas," *13th European Conference on Antennas and Propagation (EuCAP)*, Krakow, Poland, March 31 - April 5 2019.
- C.2** D. Cavallo, and R.M. van Schelven, "Closed-form analysis of artificial dielectric layers with non-periodic characteristics," *13th European Conference on Antennas and Propagation (EuCAP)*, Krakow, Poland, March 31 - April 5 2019. (Convened paper)
- C.3** R.M. van Schelven, D. Cavallo, and A. Neto, "Transmission line models of planar slot antennas," *IEEE Antennas and Propagation Society International Symposium (APS)*, Atlanta, Georgia, USA, July 7-12 2019.
- C.4** R.M. van Schelven, M. Spirito, and D. Cavallo, "Waveguide Doherty combiner for mm-waves," *IEEE Antennas and Propagation Society International Symposium (APS)*, Montréal, Canada, July 5-10 2020.
- C.5** R.M. van Schelven, M. Spirito, and D. Cavallo, "Efficient waveguide power combiners at mm-wave frequencies," *14th European Conference on Antennas and Propagation (EuCAP)*, Copenhagen, Denmark, March 15 - 20 2020. (Convened paper)

- C.6** A. Neto, R.M. van Schelven, and P. Sberna, "On the design of bulk absorbers at THz frequencies," *14th European Conference on Antennas and Propagation (EuCAP)*, Copenhagen, Denmark, March 15 - 20 2020.
- C.7** R.M. van Schelven, W. Syed, G. Carluccio, K. Doris, A. de Graauw, A. Neto, and D. Cavallo, "Pattern diversity and scan loss reduction for millimeter wave phased array applications," *15th European Conference on Antennas and Propagation (EuCAP)*, Düsseldorf, Germany, March 22 - 26 2021. (Convened paper)
- C.8** R.M. van Schelven, M. Spirito, and D. Cavallo, "Parallel plate waveguide Doherty power combiner at mm-wave frequencies," *15th European Conference on Antennas and Propagation (EuCAP)*, Düsseldorf, Germany, March 22 - 26 2021.

Master Thesis Co-supervised

- T.1** C. Tirband, "A nongalvanic chip-to-waveguide transition for mm-wave characterisation probes," M.Sc. Thesis, Delft University of Technology, Delft, The Netherlands, September 22, 2019

Propositions Accompanying the Doctoral Thesis

- I. The input impedance of a slot antenna in arbitrary stratification can be found accurately using the Method of Moments with basis functions only at the feeding point and the edges. (this dissertation, Ch. 2)
- II. A spectral domain analysis of artificial dielectric layers with a non-square, rectangular, geometry results in closed-form expressions of impedances in an equivalent transmission line model that shows a coupling between TE and TM modes. (this dissertation, Ch. 3)
- III. A parallel plate waveguide can be used as a power combining structure that allows for easy scalability by adding more inputs in parallel and shows an active impedance that is stable with frequency when the height of the PPW is small compared to the wavelength. (this dissertation, Ch. 4)
- IV. Realizing an electrically small cavity between an array of slots and artificial dielectric layers allows for effective pattern shaping using leaky waves propagating in the cavity by adjusting the geometrical parameters of the artificial dielectric layers. (this dissertation, Ch. 6)
- V. The greatest source of frustration while pursuing the Ph.D. degree is not unexpected measurement results or waiting for emails to be answered, it is when Powerpoint is determined to snap your figure somewhere you do not want.
- VI. While collaborating with others, effective communication is more important than all the knowledge in the world.
- VII. Life is a game, the people around you set the difficulty level.
- VIII. In electromagnetics, hours invested in understanding and efficient modeling save days in the implementation and design phase.
- IX. Endurance and perseverance are great virtues, but in many situations asking for help is simply more efficient.
- X. Although it is nice when others agree with you, the best conversations are with those that oppose your views.

These propositions are considered opposable and defensible, and as such have been approved by the promotor Prof.dr.ing. A. Neto

About the Author



Ralph van Schelven was born on March 9, 1993 in Dordrecht, the Netherlands. He received his B.Sc. and M.Sc. (cum laude) degrees in Electrical Engineering from Delft University of Technology (TU Delft), Delft, the Netherlands, in 2015 and 2017 respectively. During his master he specialized in telecommunications and sensing systems, with a focus on applied electromagnetics and antenna design. He performed an internship at TNO, The Hague. He worked on his M.Sc. thesis project at the THz-Sensing group at TU Delft and TNO, The Hague. During his M.Sc. thesis project he developed a method of moments procedure to analyze a linear array of skewed stacked dipole pairs in the presence of a backing reflector.

From October 2017 to October 2021 he pursued the Ph.D. degree at the THz-Sensing Group. During this period, his research interests included waveguide power combiners, element pattern shaping, artificial dielectric analysis and superstrate design and analytical/numerical techniques in electromagnetics and antenna design. This research has been carried out under the supervision of Prof. Andrea Neto as promotor, Dr. Daniele Cavallo as co-promotor and Dr. Marco Spirito as co-supervisor. The work resulted in 2 manufactured prototype demonstrators, 5 journal publications and 8 conference papers (1 nominated for *Best Student Paper Award* at the European Conference on Antennas and Propagation (EuCAP), Krakow, Poland, March 31 - April 5 2019 and 1 received an *Honourable Mention* in the *Best Student Paper Award* at the IEEE Antennas and Propagation Society International Symposium (APS), Atlanta, Georgia, USA, July 7-12 2019). During his Ph.D. he has co-supervised one M.Sc. student in the THz-Sensing group.

Acknowledgements

As I am thinking about this chapter and looking back at the past five years at the THz Sensing group I realize just how lucky I am having met so many amazing people. One of the most important people during my Ph.D. is of course my promotor Prof. Andrea Neto. I would therefore like to thank him first for giving me the opportunity of spending five years as a spartan and providing me with the tools to make it to the end of this journey. I will never forget the many discussions we had over coffee in the morning.

The next person I would like to give some special attention here is my co-promotor and daily supervisor Daniele Cavallo. I cannot even start to count the amount of times you helped me with the work, be it providing insight in a problem, finding an error in my procedure or rewriting an entire section of a paper using slightly different words. Another habit of yours I will never forget was walking in my room at the exact moment I was putting on my coat to leave. Usually this meant I would leave at least an hour later, but we made significant progress in that time. But it was not only work. We also spend hours running circles around campus or a bigger loop through the Delftse Hout, we talked about sports, food and music over coffee and during Covid there were many days that you were the only person I spoke to. Thanks for everything, I wouldn't be writing this chapter right now if it wasn't for you.

Another person I cannot forget is Marco Spirito. You helped me with measurements and often provided insight in the electronics side of the project as opposed to the electromagnetics that Daniele and I were considering. Besides this your energy always managed to lighten up a room, be it an actual room or a zoom meeting.

I was fortunate enough to work on a project that involved collaboration with another group within the building. This caused me to work together with Mohsen and Motahhareh. We spent a lot of time together working on the power combiner. You taught me so much about amplifiers and I hope I have helped you with some of your EM questions.

During the Ph.D. I also got the chance to work with people outside of TU Delft, and I was fortunate enough to work with Waqas and Giorgio from NXP. I really appreciate all your input during our meetings, and I am happy that I can now call you my colleagues at NXP. I am sure that we will share a lot of nice experiences both in the office and after work.

Next up are my bros, Sjoerd and Arturo. We shared our THz Sensing group experience all the way from the courses in the master up to this point. We had so much fun together and shared plenty of laughs (and still do). I guess that most others didn't understand half our humor, as over the years we acquired quite some inside jokes. I couldn't have wished for better roommates and I remember you everytime I'm going home or on a Friday. But the room wouldn't be complete without the master of boxes, David. You always had a story ready and you often provided some well needed distraction during a long day.

Of course, the THz Sensing group was bigger than our room. I am fortunate to have been part of many a night having drinks while playing cards against humanity or bother-

ing neighbours with awful karaoke. I am of course talking about the nights with Cristina, Sven, Shahab and Alejandro. It's truly a shame that we didn't get to visit more conferences together, but the few trips we shared are among the best memories of my Ph.D. Also I cannot forget Harshitha. Your famous expression used to make me laugh, but towards the end also I just wanted to be done with that sh*t. I'm looking forward to keep working together at NXP.

Besides these few people I just mentioned, the party wouldn't be complete without the rest of the THz Sensing group: Nuria, Jochem, Hansi, Akira, Maria, Pieter, Kenichi, Everdine, Alessandro, Marta, Juan, Paolo, Riccardo, Sander, Kevin, Huasheng, Sebastian, Bruno, Steven, Nina, Martijn, Matus, Ashwita, Nick and the new master students.

There is more to life than work and my life wouldn't be the same without my green friends of 142. I don't even know where to begin when thinking about the crazy things we shared together. Whether it is a diner, watching a movie, a trip abroad or just having a coffee, spending my time with you guys could turn a week of bad results into a night to vaguely remember based on the pictures. Thanks for everything, and there is no doubt in my mind that we'll keep having fun in the future.

Another group of amazing guys I want to mention here, is JC Schot. Right before I started the Ph.D. we had an amazing trip to Cuba and I still often look back at that vacation and cannot stop smiling. The times we managed to meet up during the last few years always turned into an incredible time. And even via whatsapp you guys often made me laugh. Thanks for everything guys.

Two people I have seen way too much these last years are Niels and Lotte. Since both of you were only two stairs away a vrijmibo was just around the corner, didn't even have to be a Friday. The game nights, BBQs and evenings hanging around watching TV always were super relaxed and our sailing weekend was awesome: 'IK KOM HIER VOOR MIJN RUST!'

And finally, I would like to thank my family for all their support during these years. Patrick, Nade and of course my parents. Jullie waren iedere avond beschikbaar voor een belletje en ik wist dat ik altijd langs kon komen voor een weekend of langer. Jullie steun heeft me op de been gehouden tijdens de moeilijke momenten. Ik kan jullie niet genoeg bedanken voor alles wat jullie voor mij hebben gedaan de laatste jaren en wat jullie nog steeds betekenen in mijn leven. Ik hou van jullie allemaal.

